이학박사 학위논문

Resistive switching behaviors of unipolar nonvolatile memory for flexible device applications

유연 소자 적용을 위한 단극성 비휘발 메모리의
저항변화 스위칭 동작 연구

2021 년 2 월

서울대학교 대학원
물리·천문학부
이 우 철

Resistive switching behaviors of unipolar nonvolatile memory for flexible device applications

유연 소자 적용을 위한 단극성 비휘발 메모리의
저항변화 스위칭 동작 연구

지도교수 이 탁 희

이 논문을 이학박사 학위논문으로 제출함
2021년 1월

서울대학교 대학원
물리•천문학부 물리학 전공
이 우 철

이우철의 이학박사 학위논문을 인준함
2021 년 1 월

위 원 장	최 석 봉	(인)
부 위 원 장	이 탁 희	(인)
위 원	노 태 원	(인)
위 원	민 홍 기	(인)
위 원	이 장 식	(인)

Abstract

Resistive switching behaviors of unipolar nonvolatile memory for flexible device applications

Woocheol Lee
Department of Physics and Astronomy
Seoul National University

Nowadays, electronic devices such as transistors and memory devices have become flexible, transparent, or stretchable. Si which has been the most commonly used substrate for electronic devices barely has these properties. To overcome the limitation of Si for flexible electronic devices, researchers have been looking for flexible substrates and flexible active materials. Many kinds of substrates such as plastic films, fiber papers, or tapes have been used for flexible application. Among these, the scotch tape can be a good flexible substrate with good flexibility, attach-ability, and low price

On the other hand, organic materials have also been used as active materials of flexible electronic devices because of their good flexibility. Organic resistive memory is one of the promising data storage technologies due to several advantages such as versatility of organic materials, low-cost device fabrication, and application on printable and flexible devices. However, the mechanism of the resistive switching phenomenon in organic resistive memory devices has not been clearly understood

In this regard, first, I have fabricated 8×8 arrays of non-volatile resistive memory devices on a commercially available tape as the flexible substrate. The memory device structure was Au/AlO_x/Au/AlO_x/Al/tape. The fabrication process to make memory devices

was dry and did not require a high-temperature process. Therefore, the tape substrate did not suffer from any damage during the fabrication. The fabricated memory devices showed typical unipolar non-volatile resistive memory property. The memory devices were turned to ON-state at ~3.5 V and turned to OFF state at ~10 V, showing a negative differential region after ~5 V. The memory devices exhibited a high ON/OFF ratio, good reproducibility, good stability, and high yield. Specifically, the ON/OFF ratio was high as ~10^4, and the devices endured over 200 cycles of reading/writing process. The retention time of the devices was longer than ~10^4 s. I observed that ~68 % of the total fabricated memory cells were well-operated. More importantly, the devices showed stable electrical properties under various bending conditions.

Although flexible memory devices were fabricated, the operating mechanism of the unipolar resistive memory device was still not clear. I investigated the time-dependent current behavior of unipolar-type memory devices under constant voltage stress. In this measurement, the current abruptly increased several times and reached ON state even when the applied stress voltage was below the turn-on voltage which was obtained from voltage sweeping. The distribution of the time required to reach ON state (denoted as turn-on time) could be described with Weibull distribution which has often been used for time-dependent gate dielectric breakdown in semiconductor transistors. Through statistical analysis of the turn-on times, I found that the abrupt increase of current followed a specific probability law. The probability of current increase over time was found to be constant in the OFF state and in all intermediate resistance states under the same voltage stress. The probability exponentially increased as the stress voltage bias increased. Through the statistical analysis, I estimated that the process of turning on the memory is probabilistically forming a conducting percolation network through which the current passes through the active layer.

During my thesis study, I fabricated flexible memory devices using unipolar resistive memory and investigated the switching mechanism of unipolar resistive memory devices. This research has led to understanding a large part of the switching mechanism of unipolar resistive memory devices and suggested operating methods for efficient use of the memory devices. Furthermore, this research may provide a foothold to manufacture more improved unipolar resistive memory devices in the future.

Keywords: Resistive memory device, Organic memory device, Switching behavior of resistive memory, Unipolar memory device.

Student Number: 2014-22373

List of Contents

List of Figures

Chapter 2.

Chapter 3.

Chapter 4.

Chapter 5.

spectra (red) of the $MAPbI_3$ film (h) I-V characteristics of flash-evaporated perovskite photodetectors under white light illumination (red) and dark (black) conditions, which were used to extract responsivity (*R*) and specific detectivity (*D**). Adapted from Lee et al.

Figure 5.2 (a) Multi-variable correlation matrix plot. (b) Representative correlation graphs for source mass and film thickness, grain size and PL peak position, relative purity and off current, and responsivity and surface roughness. The ellipses in the graphs show the regions with the confidence level of 90 %. Adapted from Lee et al.

Figure 5.3 (a) A 3D scattering plot of the film thickness according to the heating current, source mass, and excess MAI ratio ($MAI/MAPbI_3$) from the regression analysis. (b) A contour plot of the film thickness according to the heating current and the source mass. (c) Graphs of the film thickness as a function of the source mass at the different heating currents of 60 A (green line), 100 A (orange line), and 140 A (black line). (d), (e), and (f) are the same graphs as (a), (b) and (c) but represent the grain size instead of the film thickness. Adapted from Lee et al.

Figure 5.4 3D scattering plots of (a) the responsivity and (c) the relative purity according to the heating current, source mass, and $MAI/MAPbI_3$ from the regression analysis. Contour plots of (b) responsivity and (d) the relative purity is extracted from 3D scattering data (Figure 4a and c) at the source mass of 300, 500, 700 mg.

Figure 5.5 (a) I-V characteristics of white light illuminated photodetectors with three different $MAPbI_3$ films which are flash-evaporated under the optimized (red), central (black), and worst (blue) deposition condition. The inset shows log-scale I-V curves of the optimized photodetector under white light illumination (red) and dark (black) conditions. (b) The predicted responsivity values from the regression model (white) and experimental values (red) under various deposition conditions. Adapted from Lee et al.

This work is dedicated to my loving wife Dami.

Chapter 1. Introduction

1.1. Brief introduction of resistive memory devices

A resistive memory device refers to a device that distinguishes ON and OFF states by using resistive switching in response to the application of a strong external electric field. The resistive switching phenomenon was first reported by Hickmott in 1960s. In the 1960s and 1970s, a lot of research on the resistive switching was followed, but as the 1980s approached, research interest in this field rapidly declined. This is because of the stagnated research progress in the field of resistive memory devices and the remarkable development in the field of silicon-based electronics [1].

However, in the 2000s, as the issue of the fundamental physical limitations of silicon-based memory devices emerged and the understanding of oxide materials increased, resistive memory devices received considerable attention again. Resistive memory devices have several advantages including a fast process, low power consumption, and high-density integration ability. Additionally, a variety of materials can be used as the resistive switching layer such as oxide-based materials [2,3], nitride-based materials [4,5], and organic materials [6-8].

On the other hand, as research on resistive memory devices becomes active, research on fabricating flexible memory devices using resistive memory devices has also been actively conducted. The silicon-based memory devices are difficult to fabricate as flexible memory devices because they are manufactured using a hard silicon substrate. On the other hand, since the resistive memory devices can be fabricated using various materials, the substrate can be freely selected including flexible substrates.

1.2. Organic materials for flexible resistive memory devices

Organic materials for resistive memory devices provide many advantages, including material variety, solution-based process capability, and mechanical flexibility [8,9]. By utilizing these properties of organic materials, large-scale mass production is possible by applying a roll-to-roll process, and production costs are expected to be very low [10-12]. Therefore, many researchers have been studying organic resistive memory devices, and experimentally found that organic memories can satisfy the essential requirements for high-performance memory devices such as high ON/OFF ratio, long endurance and retention characteristics, and fast switching speed. However, the operation mechanism of organic resistive memory devices remains unclear, which may hinder the development of the organic resistive memory devices.

1.3. Unknown switching mechanism of unipolar resistive memory devices

Resistive memory devices can be categorized into two types according to the operation method. If the polarity of the voltage required to turn the memory device on and off is opposite, the memory device is called bipolar memory, and if the polarity is the same, the memory device is called unipolar memory. Unipolar memory can be classified into two major categories depending on the presence or absence of negative differential resistance (NDR). Most of the organic resistive memory devices exhibit the characteristic of unipolar memory including NDR. Although the first reported resistive memory device showed unipolar memory characteristics including NDR, and many organic memory devices

showed the same characteristics, the operating principle of these memory devices has not been revealed.

There are not many, but research has been carried out to better understand the principle of operation of unipolar resistive memory devices. Until the 2010s, many researchers thought that resistance changed as charge trapped in the active layer of memory devices [13-16]. In more detail, it is explained that the charge is trapped, forming an energy barrier, making charge injection difficult, and increasing the resistance. However, in the 2010s, arguments were raised that the resistance was lowered because a conducting path was formed in the active layer regardless of the charge trapping [17-19]. It has also been argued that the two concepts are combined that the conducting path is formed by the charge trap [7,20]. Discussion on the principle of operation is still ongoing [1].

References

[1] Lee J S, Lee S and Noh T W 2015 *Appl. Phys. Rev.* **2** 031303

[2] Song J, Inamdar A I, Jang B, Jeon K, Kim Y, Jung K, Kim Y, Im H, Jung W and Kim H 2010 *Appl. Phys Express* **3** 091101

[3] Wang L-G, Qian X, Cao Y-Q, Cao Z-Y, Fang G-Y, Li A-D and Wu D 2015 *Nanoscale Res. Lett.* **10** 1-8

[4] Kim H-D, An H-M, Kim K C, Seo Y, Nam K-H, Chung H-B, Lee E B and Kim T G 2010 *Semicond. Sci. Technol.* **25** 065002

[5] Chen C, Gao S, Tang G, Song C, Zeng F and Pan F 2012 *IEEE Electron Device Lett.* **33** 1711-3

[6] Kim T W, Zeigler D F, Acton O, Yip H L, Ma H and Jen A K Y 2012 *Adv. Mater.* **24** 828-33

[7] Song Y, Jeong H, Jang J, Kim T-Y, Yoo D, Kim Y, Jeong H and Lee T 2015 *ACS Nano* **9** 7697-703

[8] Cho B, Song S, Ji Y, Kim T W and Lee T 2011 *Adv. Funct. Mater.* **21** 2806-29

[9] Lee T and Chen Y 2012 *MRS Bull.* **37** 144-9

[10] Chung S, Kim S O, Kwon S-K, Lee C and Hong Y 2011 *IEEE Electron Device Lett.* **32** 1134-6

[11] Chung S, Lee J, Song H, Kim S, Jeong J and Hong Y 2011 *Appl. Phys. Lett.* **98** 153110

[12] Ji Y, Lee S, Cho B, Song S and Lee T 2011 *ACS Nano* **5** 5995-6000

[13] Bozano L, Kean B, Deline V, Salem J and Scott J 2004 *Appl. Phys. Lett.* **84** 607-9

[14] Bozano L D, Kean B W, Beinhoff M, Carter K R, Rice P M and Scott J C 2005 *Adv. Funct. Mater.* **15** 1933-9

[15] Vekderber R, Simmons J and Eales B 1967 *Philos. Mag.* **16** 1049-61

[16] Santoni F, Gagliardi A, der Maur M A and Di Carlo A 2014 *Org. Electron.* **15** 2792-801

[17] Nau S, Sax S and List-Kratochvil E J 2014 *Adv. Mater.* **26** 2508-13

[18] Busby Y, Nau S, Sax S, List-Kratochvil E, Novak J, Banerjee R, Schreiber F and Pireaux J-J 2015 *J. Appl. Phys.* **118** 075501

[19] Wolf C, Nau S, Sax S, Busby Y, Pireaux J-J and List-Kratochvil E J 2015 *Japanese Journal of Applied Physics* **54** 120301

[20] Song Y, Jeong H, Chung S, Ahn G H, Kim T-Y, Jang J, Yoo D, Jeong H, Javey A and Lee T 2016 *Sci. Rep.* **6** 33967

Chapter 2. Attachable and flexible aluminum oxide resistive non-volatile memory arrays fabricated on tape as the substrate

In this chapter, I will discuss about flexible resistive memory devices on the tape substrate. I fabricated 8 × 8 arrays of non-volatile resistive memory devices on commercially available Scotch® Magic™ tape as a flexible substrate. The memory devices consist of double active layers of AlO_x with a structure of Au/AlO_x/Au/AlO_x/Al (50 nm/20 nm/20 nm/20 nm/50 nm) on attachable tape substrates. Because the memory devices were fabricated using only dry and low temperature processes, the tape substrate did not suffer from any physical or chemical damage during the fabrication. The fabricated memory devices were turned to the low resistance state at ~3.5 V and turned to the high resistance state at ~10 V with a negative differential resistance region after ~5 V, showing typical unipolar non-volatile resistive memory behavior. The memory devices on the tape substrates exhibited reasonable electrical performances including a high ON/OFF ratio of 10^4, endurance over 200 cycles of reading/writing processes, and retention times of over 10^4 s in both the flat and bent configurations.

2.1. Introduction

Recently, resistive random access memory has attracted considerable attention as a promising memory device [1–3] due to its advantages including a fast process, low power consumption, and high density integration ability. In particular, it allows the use of simple architectures with electrocontrollable bistable resistance layers between top and bottom electrodes. A variety of materials such as oxide-based materials [4–6], nitride-based materials [7–9], and organic materials [10–12] have been used as the resistive switching

layer. Among these candidates, aluminum oxide (Al_2O_3) was employed as an active layer material because it could be deposited by using an e-beam evaporation system at relatively low temperature [13]. Al_2O_3 has gained interest as an active layer due to its good reliability and controllability [14, 15]. Although there are many previously reported results of resistive memory devices using Al_2O_3 layers, further improved electrical performances are highly desirable, particularly for endurance or electrical stability. In this regard, using doped oxide layers [16, 17], inserting metal layers into the active layer [15], or using different oxide layers that are sequentially deposited [18, 19] have been conducted to deliver better electrical characteristics. In these efforts, inserting a metal layer in the active layer can be regarded as an effective and facile approach to improving the electrical stability of the resistive memory devices.

In addition, because the demands for new electronic applications, such as wearable electronics, have increased, there have been considerable efforts to demonstrate flexible device applications [20–22]. In this manner, a use of organic materials has attracted much attention to realize soft electronics due to their great flexibility, low-cost, and low temperature processability. However further enhancements respecting to operation voltages and environmental reliability are still required for practical applications. Recently, inorganic layers, especially metal oxide layers with tens of nm thickness have been widely employed as a switching layer to realize flexible memory devices [23]. This strategy can address aforementioned issues of organic materials even though metal oxide materials have relatively less mechanical flexibility.

Additionally, low-cost processes are highly desirable for the realization of future disposable electronics such as electronic tags, labels, and newspapers [24, 25]. However, silicon-based electronic devices cannot be fabricated on low-cost flexible platforms due to

their high-temperature processes and chemical additive processes. Moreover, to develop disposable memory device applications, the use of cost-effective materials and fabrication methods is required on low-cost platforms, such as paper or polymer substrates. In this regard, research groups have demonstrated disposable field effect transistors on various paper substrates [26–28]. Our group also reported metal oxide-based resistive memory devices on wrapping paper [29]; however, there have been no attempts to realize individually operated memory arrays on these advanced platforms.

Here, I report aluminum oxide resistive non-volatile memory devices realized on commercially available Scotch® Magic™ tape substrates, which provides good attachability to a wide range of materials. The resistive memory devices in cross-bar arrays were fabricated using low-temperature

2.2. Experiments

A conventional tape (Scotch® Magic™ tape, 3M Inc.) was used as the substrate. Before fabrication, I confirmed from a thermal test that the tape could not endure temperatures over 120 °C (see figure 2.1). Therefore, low-temperature processes were used for the device fabrication. For convenient fabrication, the tape was attached to a smooth paper surface from which the tape could easily be detached. The tape substrates were cleaned by rubbing with cotton swabs. After the rubbing, the substrates were dried by blowing N_2 for ~30 s. Figure 2.1(a) shows a schematic of the device fabrication process.

The eight lines of the Al bottom electrodes were deposited through a shadow mask on the tape substrate by thermal evaporation with a deposition rate of 0.5 Å/s and at a pressure of

~10^{-6} Torr. The thickness and width of the Al bottom electrode line was 50 nm and 200 μm, respectively.

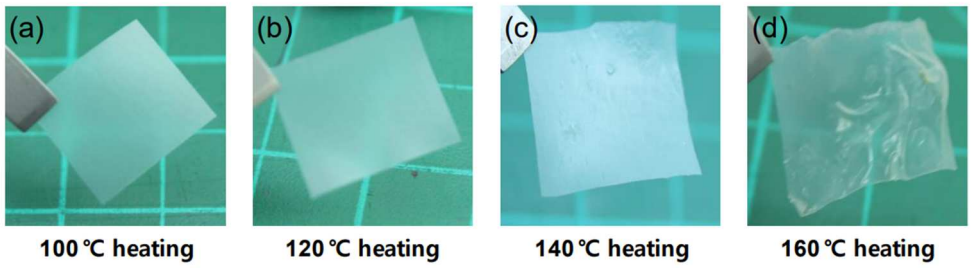

Figure 2.1 Optical images of the tape substrates after thermal treatments at (a) 100 ºC, (b) 120 ºC, (c) 140 ºC, and (d) 160 ºC for 10 min on a hot plate.

One Al_2O_3 layer can act as a resistive memory layer [30–32]; however, the endurance and yield of the memory devices could be improved by inserting a metal layer between the Al_2O_3 layers [15]. Al_2O_3 is usually deposited by atomic layer deposition (ALD). However, the ALD process requires a temperature of 200 °C; the tape substrate will be surely damaged at this temperature. Thus, I used an e-beam evaporator, which can deposit materials at room temperature. The layers of Al_2O_3, Au, Al_2O_3, and Au (20 nm/20 nm/20 nm/ 50 nm) were deposited sequentially by the electron-beam evaporator at the same pressure and with the same deposition rate as the deposition conditions of the Al bottom electrodes. The first Al_2O_3 layer was deposited covering all eight lines of the Al bottom electrodes. Then, the Au layer was deposited through a shadow mask forming 64 square cells (see figures 2.2(a) and (b)). Next, the second Al_2O_3 layer, which has the same thickness as the first Al_2O_3 layer, was deposited. Last, the Au top electrode was deposited by the electron-beam evaporator using the same conditions. The top electrodes had the same patterns as the bottom electrodes but crossed the bottom electrode lines orthogonally

in the cross-bar array architecture. After the deposition processes, the tape substrates were cut into 1.5 × 1.5 cm^2 pieces using scissors. Because tape was used as the substrate, the fabricated devices can easily stick to any surface. The right image of figure 2.2(b) shows that the fabricated memory devices stick vertically on the curved wall of a vial.

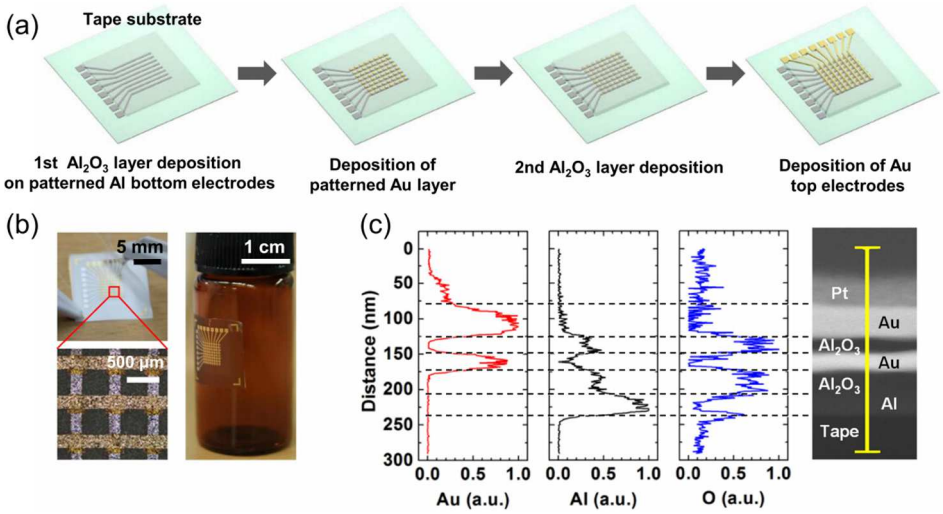

Figure 2.2 (a) Fabrication procedure of the memory devices on Scotch® Magic™ tape as a substrate. (b) Photographic and optical microscope images of the memory devices. (c) A cross-sectional TEM image with specified element percentage graphs along the yellow line.

Figure 2.2(c) shows the cross section transmission electron microscope (TEM) image of a memory device with the proportion of each element along the cross section. I could verify that Au was deposited as the top electrode and the active layer between the Al_2O_3 layers from the Au proportion graph. The O-rich parts indicate the Al_2O_3 active layers, which were well-deposited without aggregation or defects even though they were formed by the low-temperature thermally vaporized process using an e-beam evaporator. The bottom Al_2O_3 layer was thicker than the top Al_2O_3 layer, because the Al bottom electrode

was naturally oxidized forming an Al_2O_3 film. The Pt on the Au top electrode layer was deposited as a protection layer for the focused ion beam process, which was needed to make the specimen for TEM examination.

The electrical properties of the memory devices were measured with a semiconductor parameter analyzer (Model 4200 SCS, Keithley Inc.) inside a N_2 filled glove box at room temperature. To measure the electrical characteristics in the flat and bent conditions, the memory devices were attached on glass substrates and semi-cylinders, respectively.

2.3. Results and discussions

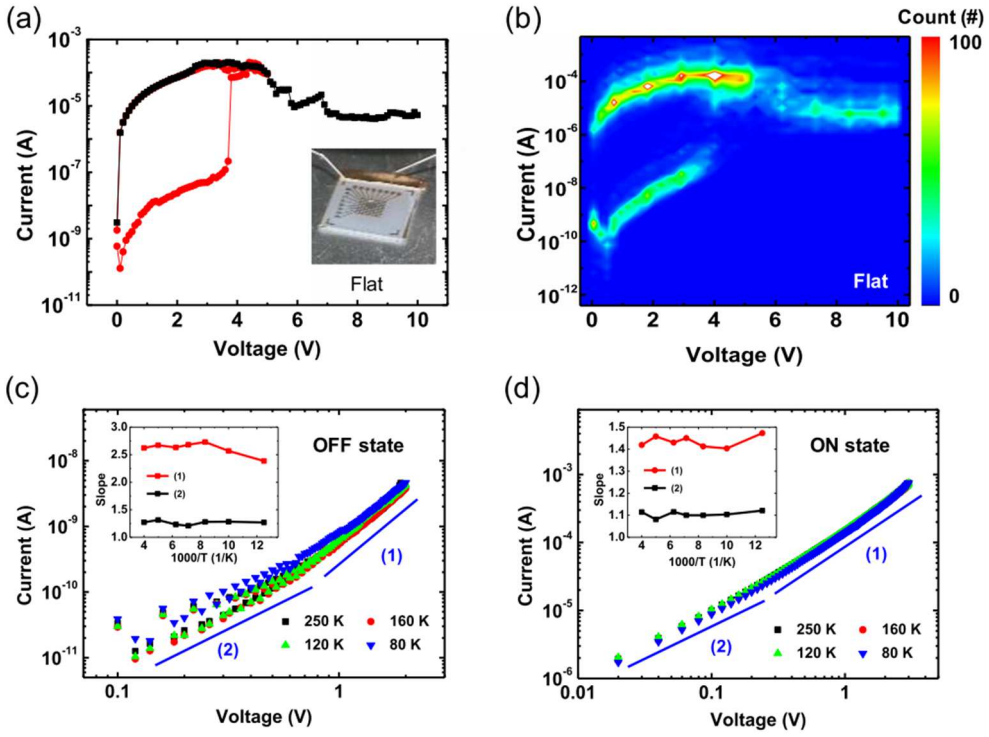

Figure 2.3 (a) Representative current–voltage graph of a memory device in the flat condition. (b) Color map of the current–voltage graphs of 65 memory devices. A double-log plot analysis of the current–voltage characteristics at various

temperatures in (c) ON state and (d) OFF state. Inset graphs are slops versus 1000/T (T: temperature).

Figure 2.3(a) shows the representative electrical properties of the memory devices. The inset is a photograph of the memory devices on the tape being measured in the flat condition. To make the ON state (low resistance state), forward and backward sweeping voltages were applied from 0 to 5 V and then from 5 to 0 V. The current jumped swiftly from the OFF state (high resistance state) to the ON state around ~4 V. The ON state was maintained as long as a low voltage was applied, which means the memory devices have a non-volatile memory characteristic. To make the devices in the OFF state, I swept the voltage from 0 to 10 V. The current was reduced after ~5 V, showing a negative differential resistance region [33, 34]. After this, the current was maintained in the OFF state at low voltage. As a result, the device had two controllable stable states so that it can be used as a rewritable non-volatile memory. The ON/OFF ratio was found to be high enough (~10^4) at a read voltage of 0.5 V. I examined a total of 94 memory device cells and confirmed 65 cells worked well (device yield of ~70%). Figure 2.3(b) shows a color map of the current–voltage graphs of all 65 working memory cells, which confirms that the memory window between the ON and OFF states was large enough statistically. Additionally, figure 2.3(b) shows that the OFF currents of most devices abruptly changed to ON currents. Note that the failure of ~30% devices showed either short currents or only OFF state currents.

Many research groups have explained charge transport mechanism in resistive switching memory devices with space charge limited current (SCLC), Poole–Frenkel conduction, and Fowler–Nordheim tunneling [35–37]. I previously explained that Poole–

Frenkel conduction and SCLC were dominant for the charge transport in a similar metal oxide memory system [29]. For the clear understanding, I performed variable temperature measurements, as the results are temperature, the charge transport mechanism in our memory device might not be explained solely by SCLC or Poole–Frenkel conduction. The temperature-independent transport properties may suggest tunneling conductions through trap sites in the switching layer [38]. Therefore, I propose a traps-associated tunneling (see figure 2.4).

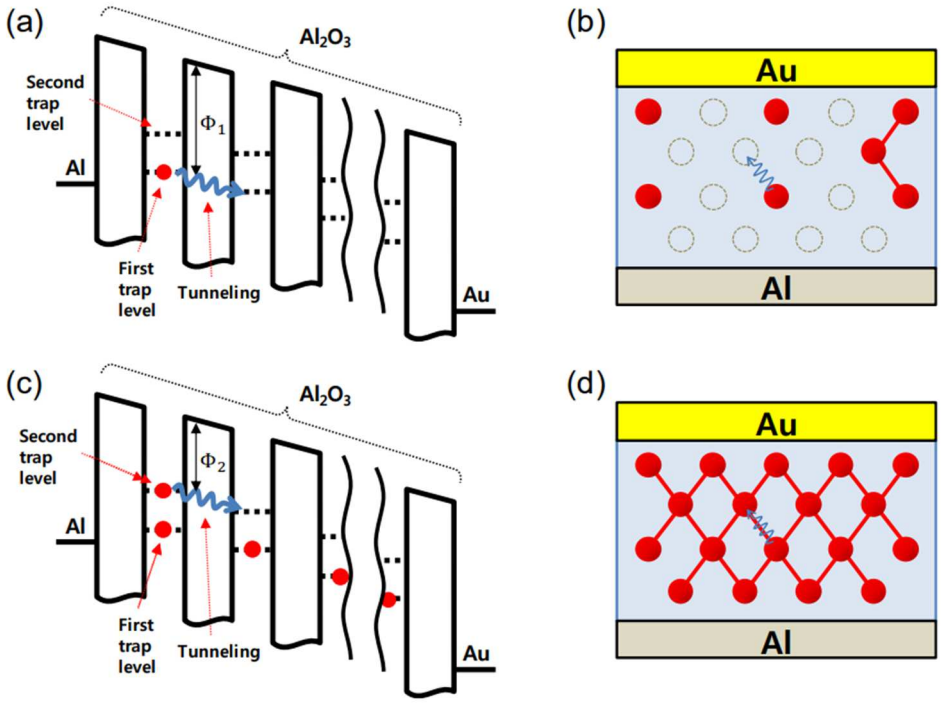

Figure 2.4 (a) Energy band diagram of traps-associated tunneling with a large potential barrier in the OFF state. (b) Schematic of current paths in the OFF state. (c) Energy band diagram of traps-associated tunneling with a small potential barrier in the ON state. (d) Schematic of a current path in the ON state.

From the unipolar switching behaviors with negligible temperature dependence (figure 2.3(c) and (d)), the main switching mechanism can be thought to be traps-associated

tunneling through the trap sites in the switching layers. Because the Al_2O_3 layers were deposited using an e-beam evaporator at low-temperature, a lot of defects might be created. Although it is not exactly the same system, I have previously explained trap-related resistive memory systems by trap-associated transport behaviors. Figure 2.4 shows schematics of the traps-associated tunneling model. In the initial state, all trap sites are empty. During the OFF state, the first trap-levels (deep traps) are started to be filled via trap-to-trap tunneling because the potential barrier height (Φ1) between the trap sites is too high to transport by thermionic emission over a potential barrier (see figure 2.4(a) and (b)). If the first trap-levels are fully filled, following charges should be trapped in an upper energy level in the same trap site. After the filling process, charges can transport by trap-totrap tunneling through the second trap-levels (shallow traps) forming current paths. Note that the charges in the second trap-levels can more easily move to neighboring trap sites because the potential barrier height (Φ2) is lower than Φ1 (see figure 2.4(c)). At this point, the state is changed into an ON state (low resistive state). At the voltage in the negative differential resistance (NDR) region, charges in the first trap-levels start to be ejected out by tunneling. At this point, the current path would be disconnected and the memory state is changed into an OFF state. I think that this is our best effort to understand the charge transport mechanism of our memory devices, but more clear understanding of the mechanisms will require further investigations in a future study.

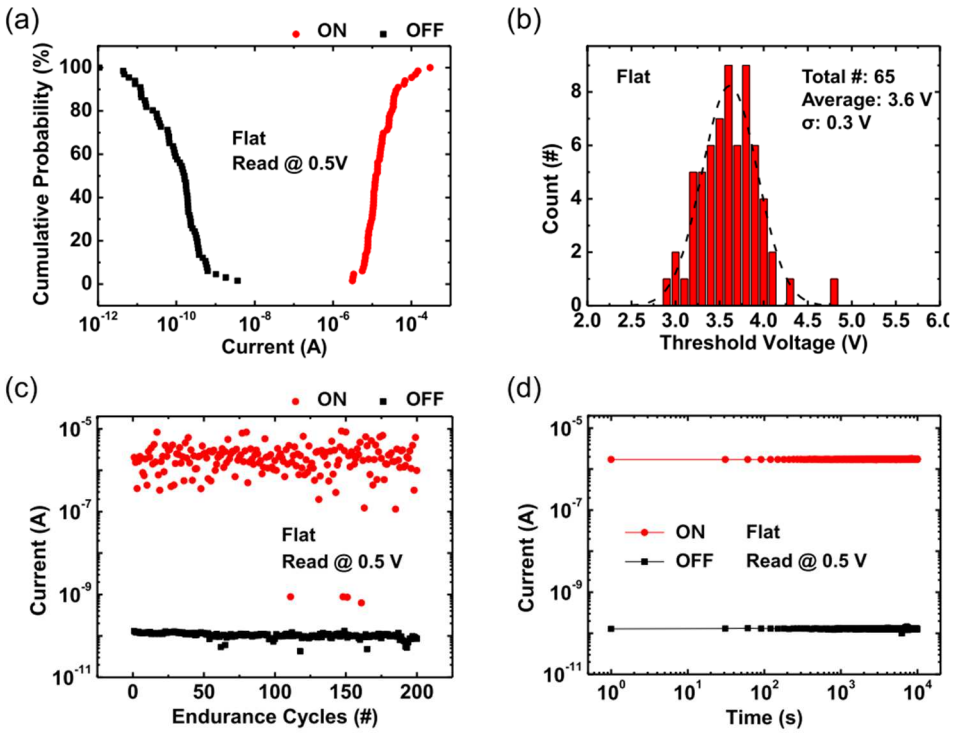

Figure 2.5 (a) The cumulative probability of the memory devices in the flat condition at a read voltage of 0.5 V. (b) The distribution of the threshold voltages. (c) Endurance test and (d) retention test results of the memory devices.

One of the important characteristics of memory devices is reliability. I tested the reliability using statistical methods. Figure 2.5(a) shows the ON and OFF currents of 65 memory device cells at 0.5 V. I could find that the lowest ON current was over two orders of magnitude higher than that of the highest OFF current. This indicates that the memory devices had two stable states at the read voltage. Figure 2.5(b) shows the distribution of the threshold voltage values, which are the voltages required to turn the devices to the ON state. The average threshold voltage was found to be ~3.6 V with a standard deviation of ~0.3 V. This small distribution of threshold voltages indicates that the memory devices had statistical uniformity. Figure 2.5(c) shows the endurance test results of the memory devices.

The ON states were achieved by applying 5 V, which is sufficiently higher than the threshold voltage of ~3.6 V. Then, the OFF states were achieved by applying 10 V for approximately 0.1 s. The read voltage was 0.5 V. The memory devices maintained the wide memory window of three to four orders of magnitude between ON and OFF states for over 200 cycles of ON and OFF states. Although there were several failures to turn on (see some scattered red data points in figure 2.5(c)), it did not mean the memory device had broken. Figure 2.5(d) shows the retention test results of a memory device. The read voltage was 0.5 V and the reading interval was 30 s for both the ON and OFF states. The currents of both the ON and OFF states were stably maintained for ~10^4 s with a high ON/OFF ratio of ~10^4. Note that the performances of these memory devices on the tape substrate were comparable to those of the memory devices fabricated on another plastic substrate, OHP film (see figure 2.6).

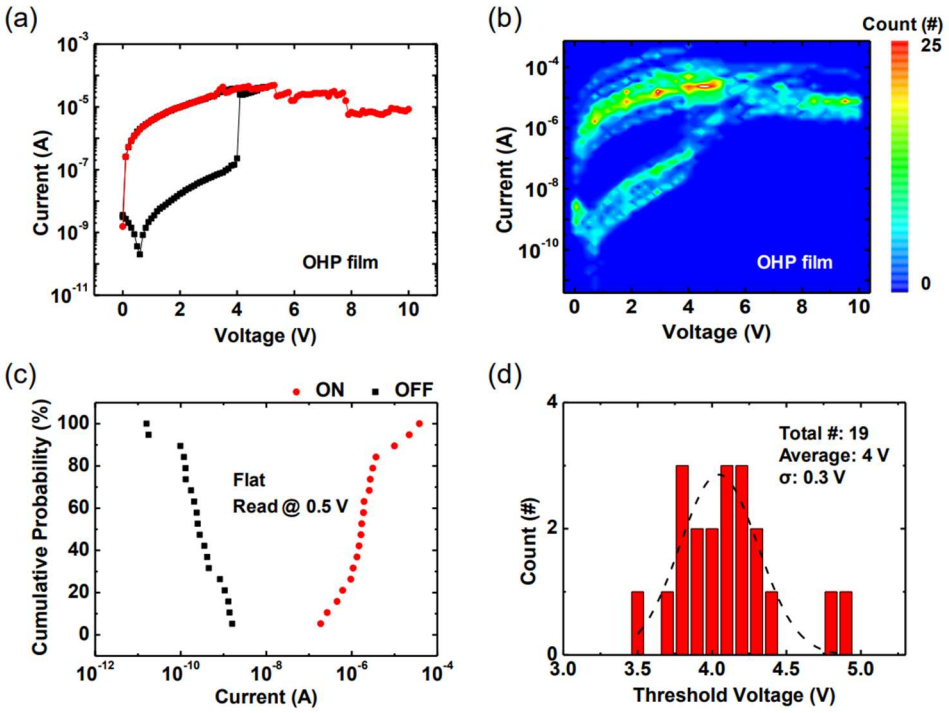

Figure 2.6 (a) Representative current-voltage graph of a memory device on OHP film. (b) Color map of current-voltage graphs of 19 memory devices. (c) The cumulative probability of the memory devices at read voltage 0.5 V. (d) The distribution of threshold voltages.

Figure 2.6 shows the electrical properties of the resistive memory devices of $Au/Al_2O_3/Au/Al_2O_3/Al$ fabricated on OHP films. 19 cells out of 30 cells (63 %) worked well as operative memory. Figure 2.6(a) is the representative electrical characteristics of the memory devices. The device turns to ON state at ~4 V and showed negative differential resistance (NDR) after ~5 V. Figure 2.6(b) is a color map of collection of 19 cells' electrical properties. I could confirm that the memory window was large enough for switching operation. The lowest current of ON states was ~100 times larger than the highest current of OFF states at read voltage (figure 2.6(c)). Figure 2.6(d) represents the distribution of threshold voltages of the memory devices. The average threshold voltage was found to be ~4.0 V with the standard deviation of ~0.3 V. These results indicate that the devices fabricated on OHP films can also be used as resistive non-volatile memory.

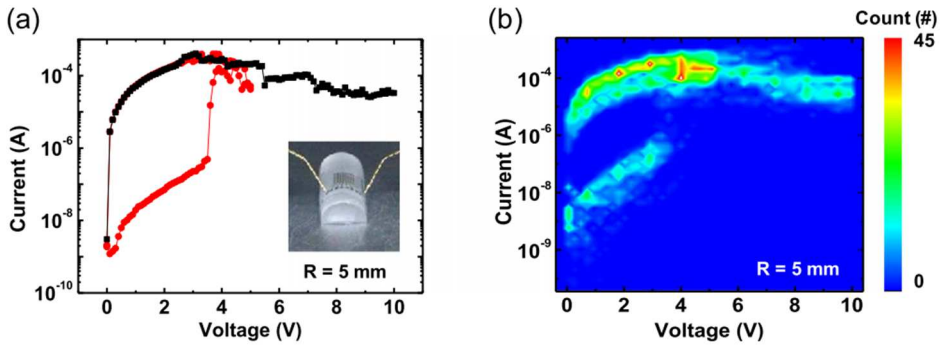

Figure 2.7 (a) Representative current–voltage graph of a memory device in the bent condition with a bending radius of 5 mm. (b) Color map of current–voltage graphs of 30 memory devices.

To investigate the electrical properties of the memory devices in bending conditions, I attached the devices on a semi-cylinder with a radius of 5 mm and performed the same measurements that were conducted on the memory devices in the flat conditions. Figure 2.7(a) is the representative electrical characteristics of a memory device in the bent condition. Similar I–V characteristics were observed in the flat and bent conditions (see figures 2.4 and 2.7). I investigated a total of 47 memory device cells in the bent condition. The device yield was found to be ~64% (30 of 47), which was slightly lower than that (~70%) in the flat condition. The color map in figure 2.7(b) shows that the large memory window was well maintained in the bent condition.

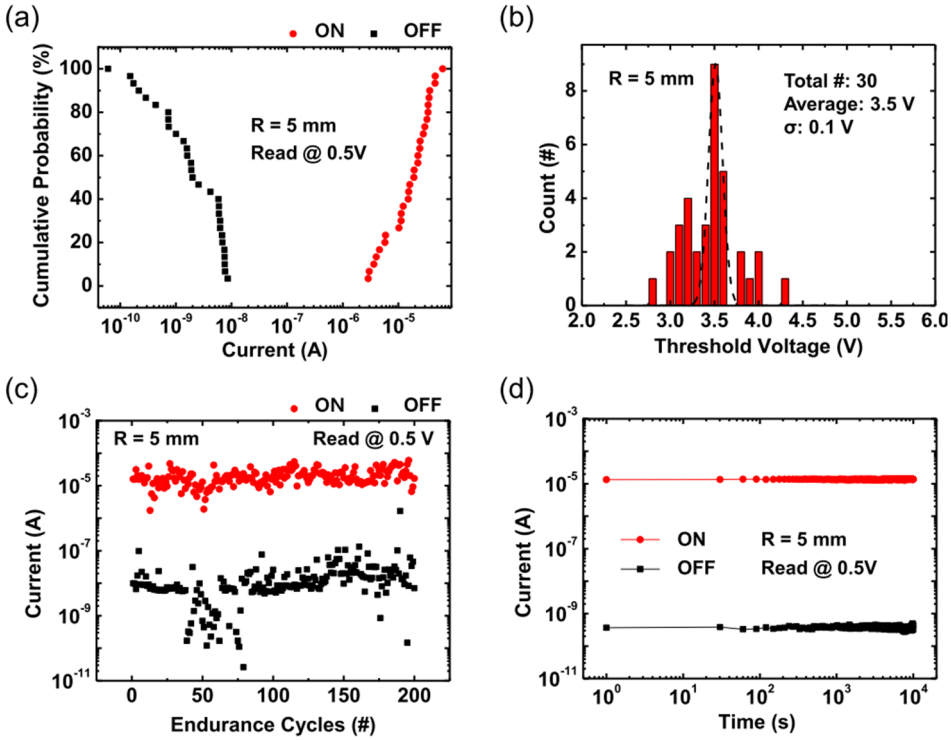

Figure 2.8 (a) The cumulative probability of the memory devices in the bent condition with a bending radius of 5 mm at read voltages of 0.5 V. (b) The distribution of threshold voltages. (c) Endurance test and (d) retention test results of the memory devices.

The cumulative probability graph (figure 2.8(a)) shows that the high ON/OFF ratio at read voltage was maintained in the bent condition. The distribution of the threshold voltages was also similar to that for the flat condition (figure 2.8(b)). The average and the standard deviation of the threshold voltage were found to be ~ 3.5 V and ~ 0.1 V, respectively. The memory devices on the curved surface still endured 200 cycles of ON/OFF. Although the ON/OFF ratio was slightly degraded and the deviation of the OFF currents became larger than in the memory devices on the flat surface (figure 2.8(c)), the devices maintained two well-separated stable states. Figure 2.8(d) also supports that the bending did not have any noticeable harmful influence on the retention characteristics of the memory devices. Also, during 1000 cycles of bending-relaxation at a bending radius of 5 mm, the devices maintained a high ON/OFF current ratio of $\sim 10^4$ with threshold voltage of ~ 3.5 V and no significant changes of the switching behaviors were observed during this measurement (see figure 2.9(a)). And, the memory devices well maintained their electrical properties including the ON/OFF state currents and threshold voltages under a harsh bending condition with a bending radius of 1 mm, as shown in figure 2.9(b). Moreover, the memory devices exhibited good retention time of $\sim 10^4$ s and stable switching-operation during the 200 cycles of bending-relaxation at the bending radius of 1 mm (see figures 2.9(c) and (d)). All these results suggest that our memory devices on the tape substrate can be attached on any curved surface within the bending radius of 1 mm without serious performance degradation.

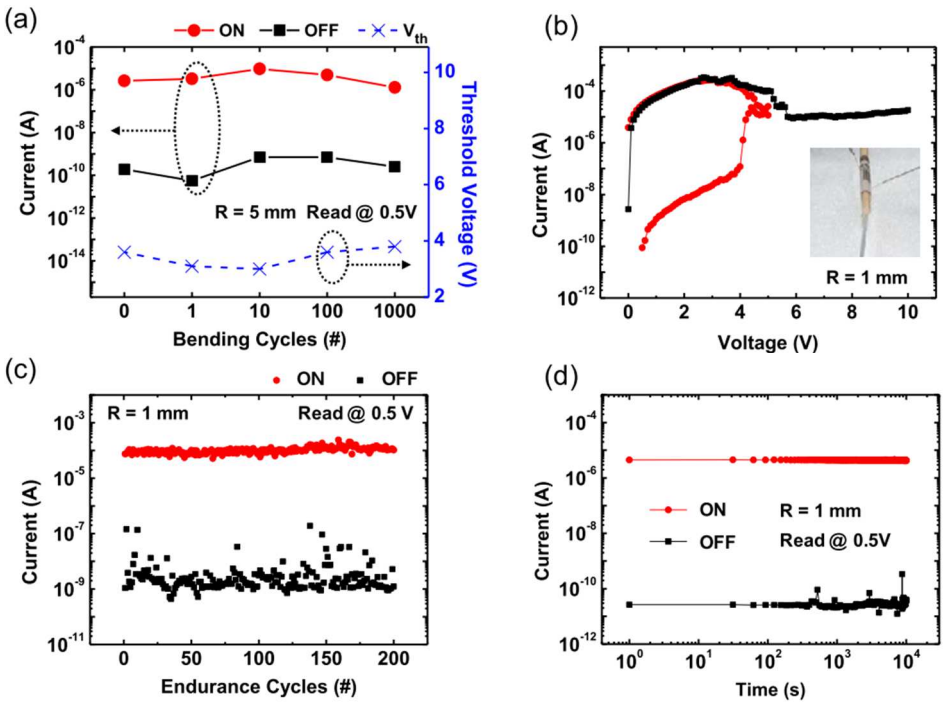

Figure 2.9 (a) Bending cycle test with a bending radius of 5 mm. (b) Representative current–voltage graph of a memory device with a bending radius of 1 mm. (c) Endurance test and (d) retention test results of the memory devices with a bending radius of 1 mm.

2.4. Conclusion

In summary, I fabricated resistive memory device arrays on conventional Scotch® Magic™ tape substrates using dry and low temperature processes. The attachable memory devices showed typical unipolar resistive switching properties with good electrical performance in both flat and bent configurations. The memory devices endured 200 cycles of switching and maintained their states for over 10^4 s with a high ON/OFF ratio (~10^4). The attachable memory device arrays fabricated on flexible and disposable tape substrates

may provide a pathway for the realization of practical and reliable resistive memory applications such as disposable electronic tags, labels, and sticker memory devices.

References

[1] Waser R and Aono M 2007 *Nat. Mater.* **6** 833

[2] Kwon D-H et al 2010 *Nat. Nanotechnol.* **5** 148

[3] Lee M-J et al 2011 *Nat. Mater.* **10** 625

[4] Akinaga H and Shima H 2010 *Proc. IEEE* **98** 2237

[5] Sawa A 2008 *Mater. Today* **11** 28

[6] Wong H-S P, Lee H-Y, Yu S, Chen Y-S, Wu Y, Chen P-S, Lee B, Chen F T and Tsai M-J 2012 *Proc. IEEE* **100** 1951

[7] Kim H-D, An H-M, Kim K C, Seo Y, Nam K-H, Chung H-B, Lee E B and Kim T G 2010 *Semicond. Sci. Technol.* **25** 065002

[8] Chen C, Gao S, Tang G, Song C, Zeng F and Pan F 2012 *IEEE Electron Device Lett.* **33** 1711

[9] Kim H-D, An H-M, Lee E B and Kim T G 2011 *IEEE Trans. Electron Devices* **58** 3566

[10] Cho B, Song S, Ji Y, Kim T W and Lee T 2011 *Adv. Funct. Mater.* **21** 2806

[11] Wang C, Gu P, Hu B and Zhang Q 2015 *J. Mater. Chem. C* **3** 10055

[12] Lee T and Chen Y 2012 *MRS Bull.* **37** 144

[13] Madaan N, Kanyal S S, Jensen D S, Vail M A, Dadson A E, Engelhard M H, Samha H and Linford M R 2013 *Surf. Sci. Spectra* **20** 43

[14] Pan F, Gao S, Chen C, Song C and Zeng F 2014 *Mater. Sci. Eng. R* **83** 1

[15] Song J et al 2010 *Appl. Phys. Express* **3** 091101

[16] Kim W, Park S I, Zhang Z, Yang-Liauw Y, Sekar D, Wong H-S P and Wong S S 2011 VLSI Symp. on Tech. Dig.p 22 http://ieeexplore.ieee.org/abstract/document/5984614/

[17] Wu Y-T, Jou S and Yang P-J 2013 *Thin Solid Films* **544** 24

[18] Kim K M, Choi B J, Koo B W, Choi S, Jeong D S and Hwang C S 2006 *Electrochem. Solid-State Lett.* **9** G343

[19] Wang L-G, Qian X, Cao Y-Q, Cao Z-Y, Fang G-Y, Li A-D and Wu D 2015 *Nanoscale Res. Lett.* **10** 1

[20] Cai Y, Tan J, YeFan L, Lin M and Huang R 2016 Nanotechnology **27** 275206

[21] Cramer T, Travaglini L, Lai S, Patruno L, de Miranda S, Bonfiglio A, Cosseddu P and Fraboni B 2016 *Sci. Rep.* **6** 38203

[22] Jang B C, Seong H, Kim S K, Kim J Y, Koo B J, Choi J, Yang S Y, Im S G and Choi S-Y 2016 *ACS Appl. Mater. Interfaces* **8** 12951

[23] Sun Y and Rogers J A 2007 *Adv. Mater.* **19** 1897

[24] Forrest S R 2004 *Nature* **428** 911

[25] Tobjörk D and Österbacka R 2011 *Adv. Mater.* **23** 1935

[26] Kim Y-H, Moon D-G and Han J-I 2004 *IEEE Electron Device Lett.* **25** 702

[27] Zocco A T, You H, Hagen J A and Steckl A J 2014 *Nanotechnology* **25** 094005

[28] Zschieschang U, Yamamoto T, Takimiya K, Kuwabara H, Ikeda M, Sekitani T, Someya T and Klauk H 2011 *Adv. Mater.* **23** 654

[29] Jang J, Song Y, Cho K, Kim Y, Lee W, Yoo D, Chung S and Lee T 2016 *Flex. Print. Electron.* **1** 034001

[30] Lin C-Y, Wu C-Y, Wu C-Y, Hu C and Tseng T-Y 2007 J. Electrochem. Soc. 154 G189

[31] Hubbard W, Kerelsky A, Jasmin G, White E R, Lodico J, Mecklenburg M and Regan B C 2015 *Nano Lett.* **15** 3983

[32] Zhu W, Chen T P, Liu Z, Yang M, Liu Y and Fung S 2009 *J. Appl. Phys.* **106** 093706

[33] Simmons J G and Verderber R R 1967 *Proc. R. Soc. A* **301** 77

[34] Kim T W, Zeigler D F, Acton O, Yip H L, Ma H and Jen A K Y 2012 *Adv. Mater.* **24** 828

[35] Spahr H, Montzka S, Reinker J, Hirschberg F, Kowalsky W and Johannes H-H 2013 *J. Appl. Phys.* **114** 183714

[36] Chang W-Y, Lai Y-C, Wu T-B, Wang S-F, Chen F and Tsai M-J 2008 *Appl. Phys. Lett.* **92** 022110

[37] Lee H Y et al 2009 *IEEE Electron Device Lett.* **30** 703

[38] Yu S, Guan X and Wong H-S P 2011 *Appl. Phys. Lett.* **99** 063507

Chapter 3. Investigation of Time-Dependent Resistive Switching Behaviors of Unipolar Non-Volatile Organic Memory Devices

In this chapter, I will discuss about the switching behavior of unipolar non-volatile memory devices. Organic resistive memory devices are one of the promising next-generation data storage technologies which can potentially enable low-cost printable and flexible memory devices. Despite a substantial development of the field, the mechanism of the resistive switching phenomenon in organic resistive memory devices has not been clearly understood. Here, I investigate the time-dependent current behavior of unipolar organic resistive memory devices under a constant voltage stress to investigate the turn-on process. The turn-on process is discovered to occur probabilistically through a series of abrupt increases in the current each of which can be associated with new conducing paths formation. The measured turn-on time values can be collectively described with Weibull distribution which reveals the properties of the percolated conducting paths. Both the shape of the network and the current path formation rate are significantly affected by the stress voltage. A general probabilistic nature of the percolated conducting path formation during the turn-on process was demonstrated among unipolar memory devices made of various materials. Our results are also highly relevant for practical operations of the resistive memory devices since I can potentially set guidelines for time-widths and magnitudes of voltage pulses required for writing and reading operation.

3.1. Introduction

Organic materials for electronic devices have attracted great attention due to their advantageous properties such as material variety, low production cost, mechanical flexibility, and large area processing capability.[1-2] Among various organic electronic devices, organic non-volatile resistive memory is one of actively researched areas.

The organic resistive random access memory (ORRAM) devices can be realized by

sandwiching various organic materials between top and bottom electrodes in a vertical two-terminal structure.[3,4] The ORRAM devices possess at least two stable resistance states which can be switched to each other by an external electric field. ORRAM can be categorized according to the polarity of the switching electric field: unipolar memory devices which can be switched ON and OFF by applying the electric field in the same polarity and bipolar memory devices which requires the electric field in the opposite polarities for the ON and OFF switching. Through extensive studies by many research groups, the electrical performances of ORRAM devices have been significantly improved along with advancement of architectural design and integration.[5-10] Nevertheless, the memory operation mechanism of ORRAM is still not completely understood. Especially, the operating principles of unipolar ORRAM devices which show S-shape current-voltage characteristics with a negative differential resistance (NDR) region are still controversial.[11-13]

Various experimental tools have been employed to investigate the fundamental properties of ORRAM devices; for example, impedance spectroscopy[12] to directly probe the charge trapping in the active layer and a direct spatial mapping of the current paths within the layer via elemental analysis.[14,15] I have recently employed 1/f noise measurements to show that the conduction paths in organic nanocomposite memory devices form a percolation network from the resistance scaling of the 1/f noise.[13,16] A further study of time-dependent current fluctuation behaviors during the turn-off process in the NDR region demonstrated that the percolating conduction paths dynamically changed before completely getting disconnected (i.e. OFF state).[13,16] However, there has been little research conducted on the formation process of this percolation network during the turn-on process in details.

In this study, I investigated the time dependent resistive switching behaviors, especially in the turn-on process. I observed how the current in the device increased with time while applying a constant voltage stress for ORRAM devices that were made of a nanocomposite layer of polystyrene (PS) and pheyl-C61-butyric acid methyl ester (PCBM). The fundamental properties of the PS:PCBM ORRAM devices were revealed through a statistical analysis of the turn-on time values from multiple measurements by employing Weibull distribution[17] which has been widely sed for describing the electrical breakdown of various materials.[18-22] Our study is the first attempt of applying the Weibull statistics in the context of ORRAM devices, to the best of our knowledge. I compared the results for the PS:PCBM ORRAM devices with other devices made from three different organic and inorganic materials, and I extracted some common fundamental properties among the unipolar resistive memory devices.

3.2. Results and discussion

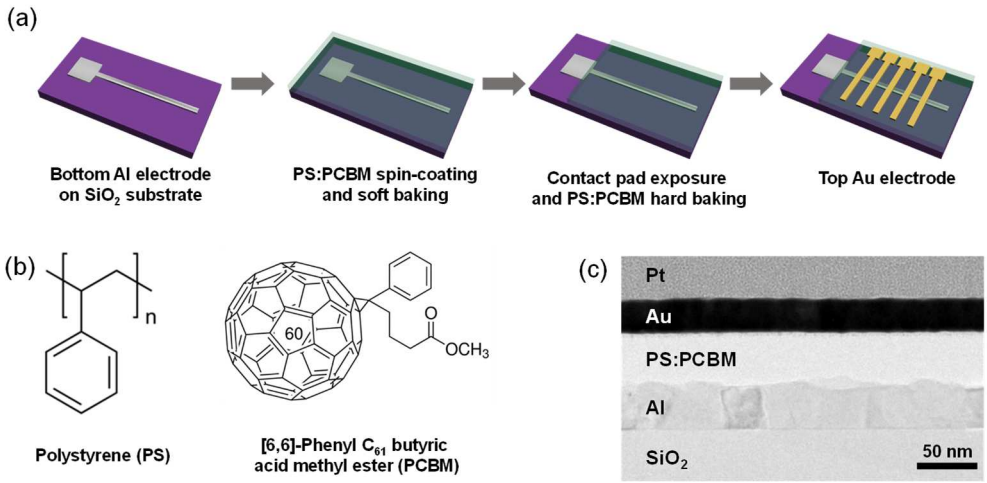

Figure 3.1 (a) A schematic showing the device fabrication processes for Al/PS:PCBM/Au organic resistive memory devices. (b) The molecular structure

of the PS:PCBM composite material. (c) A cross-sectional TEM image of the memory device.

Figure 3.1(a) shows the fabrication process of the ORRAM devices. First, Al (30 nm thick) was deposited as the bottom electrode on a SiO_2/Si substrate using a thermal evaporator. Then, a composite solution made with PS:PCBM dissolved in chlorobenzene was spin coated to form the memory layer (see Figure 3.1(b)). After a soft-baking of the samples, the contact pads of the Al bottom electrodes were exposed by sobbing with an acetone-soaked Q-tip cotton swab. After a hard baking of the samples on a hot plate at 120 ˚C for 60 min, Au (30 nm thick) was deposited for the top electrodes. As a result, memory cells with a size of 100 μm × 100 μm were fabricated (see Methods for more details). Figure 3.1(c) shows the cross-sectional transmission electron microscope (TEM) image of a memory cell, indicating a well-defined PS:PCBM memory layer with a thickness of ~40 nm without any noticeable penetration of metals (Au and Al) into the layer.

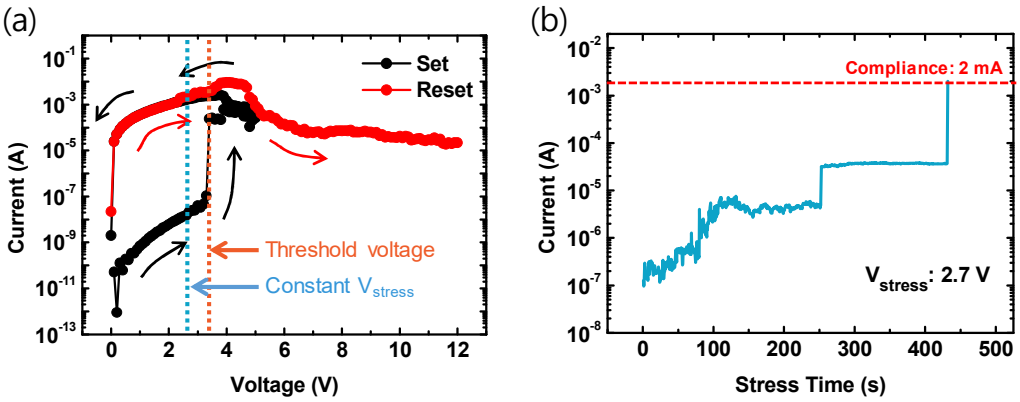

Figure 3.2 (a) A representative current-voltage graph of a PS:PCBM memory device. (b) A representative current-stress time curve under a constant voltage stress, V_{stress}, of 2.7 V.

The memory devices showed a typical unipolar behavior with the NDR. Figure 3.2(a) shows a representative current-voltage (I-V) curve of a PS:PCBM ORRAM device. The SET process consisted of sequential forward and reverse voltage scans between 0 and 5 V. Note that the bottom Al electrode was grounded and a bias voltage was applied at the top Au electrode. The resistive state changed from a high resistance state (HRS; OFF state) to a low resistance state (LRS; ON state) at the threshold voltage in a range of 3–4 V during the voltage sweep in the SET process. The LRS was maintained even when the applied voltage was removed, exhibiting non-volatile memory characteristics. The RESET process consisted of a single voltage sweep from 0 to 12 V, in which the current decreased after ~4 V and showed the NDR behavior. When the applied voltage was removed at around 12 V, the memory device turned back to HRS. The memory devices could endure over 500 cycles of ON/OFF switching cycles and maintain the memory states for longer than 10^4 s.

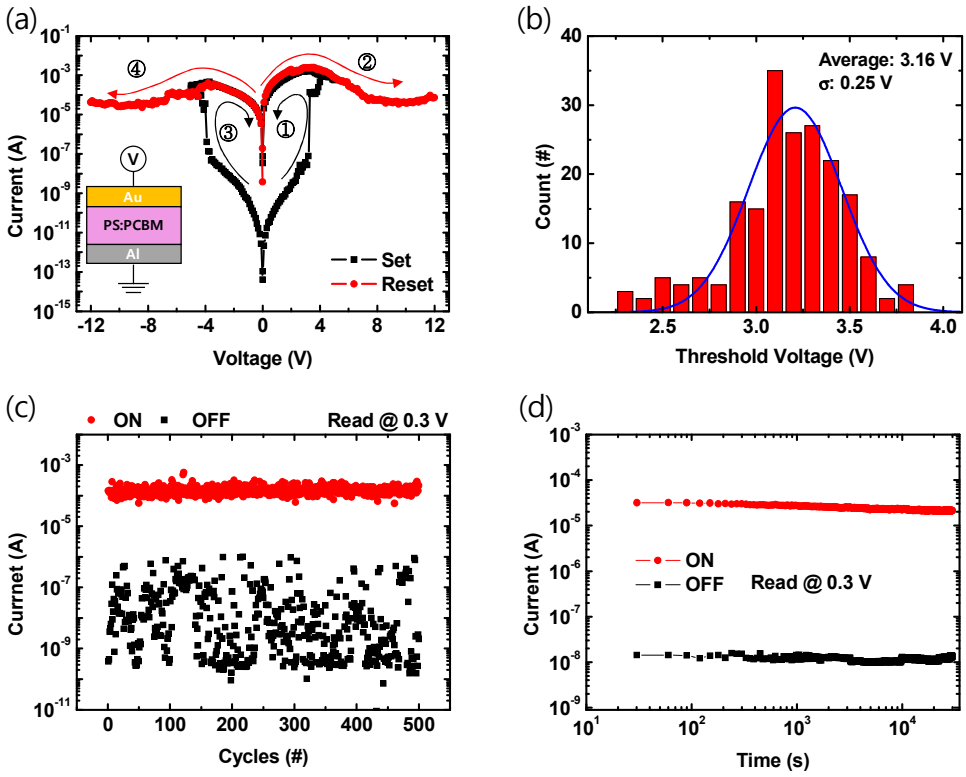

Figure 3.3 (a) Basic current-voltage characteristics, (b) Electrical endurance test, and (b) retention test results of the PS:PCBM memory device. (c) The distribution of the turn-on voltages of the same device.

In more detail, PS:PCBM memory devices shows typical unipolar I-V curves regardless of the polarity of the applied voltage (see figure 3.3(a)). Figure 3.3(b) represents the distribution of the threshold voltages at which abrupt current increases appeared during the voltage sweep from 0 to 5 V. The average value of the threshold voltages was extracted to be ~3.16 V from the Gaussian fitting of the threshold voltage distribution (see figure 3.3(b)). Figure 3.3(c) shows the electrical endurance of the PS:PCBM memory device discussed in the main manuscript. As shown in this figure, the device endured 500 cycles of switching. The distribution of the OFF current level had a finite distribution. However, it did not affect the τ which is obtained from the time dependent switching measurements under a constant voltage bias. This is because the current increase depends linearly on τ (see figure 3.10(a) in the main manuscript). τ will be decided by I_{set} (in the order of 10^{-3} A) regardless of the OFF current value (in the order 10^{-6} to 10^{-10} A). Figure 3.3(d) shows the retention test of the memory device. The device maintained its ON and OFF states over the duration of 10^4 s.

Generally, to turn the memory devices from the HRS to LRS, a voltage pulse with the magnitude above a certain voltage is applied. Threshold voltage is commonly determined as a voltage at which the current abruptly increases in the current-voltage sweep scans. When memory devices are operated in the voltage pulse mode, a certain duration of voltage pulse is required to turn on the memory devices. In our previous study, I observed that the smaller the applied voltage, the longer the minimum time required to turn on the memory devices.[23] Here, one may expect that the turn-on process could occur even when the

applied voltage is below the threshold voltage, provided that one applies the voltage for a long enough time. Thus, I measured the current over time while applying a constant voltage stress (V_{stress}) of an arbitrarily chosen value of 2.7 V (below the threshold voltage, see figure 3.2(a)). I observed that the current under V_{stress} irregularly increased with several steps over time (see figure 3.2(b)). After several step increases, the current ultimately reached 2.0 mA (set as the compliance) which is the expected current of ON state.

After the current reached the compliance, the RESET process described above was conducted to confirm the reversibility of the switching event. The memory device showed the same I-V curve of the RESET process shown in figure 3.2(a) and turned off. This means that the state of the memory device could change from the OFF to ON state under V_{stress} below the threshold voltage and that this process is effectively the same as the SET process. Here, I could infer that the threshold voltage is not a fixed value but is a variable that depends on the voltage stress-time.

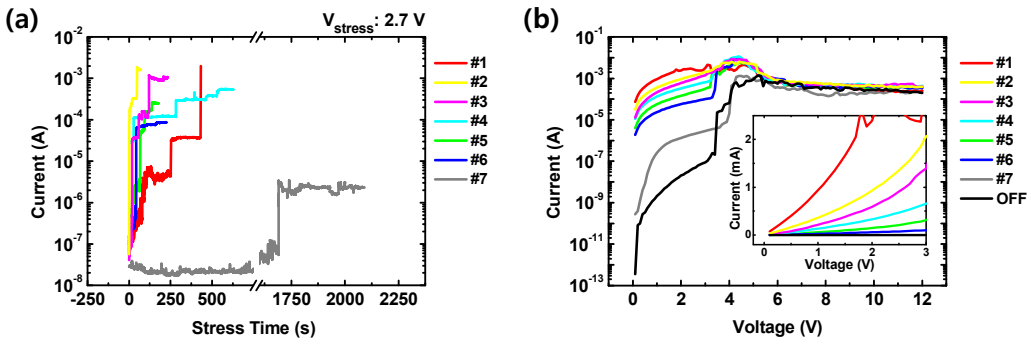

Figure 3.4 (a) Current-stress time curves of time-dependent current measurements in the same device under V_{stress} of 2.7 V. The measurements were manually stopped at different resistance states. (b) I-V curves of the same device for the different resistance states which were formed by the process shown in the (a). The color codes in (a) and (b) correspond to the same resistance states.

The current steps revealed the existence of multiple intermediate resistive states (IRSs) before reaching the ON state. In order to check the stability of the IRS, I manually removed the stress voltage while at the IRS. I found that the IRS was stable, and that the resistance value of the IRS corresponded to the value just before the stress voltage was removed. In more detail, intermediate resistance state (IRS) was shown when the memory devices switched from high resistance state (HRS) to low resistance state (LRS) under a constant voltage stress. In order to check whether the IRSs were stable, I manually removed the voltage stress when the device was in IRS (see figure 3.4(a)). After removing the voltage stress, I swept the voltage from 0 to 12 V to reset the device. Figure 3.4(b) shows that IRSs were well maintained even after the applied voltage disappeared. The inset of Figure 3.4(b) shows that the current-voltage curves were not linear, which means that the conduction mechanism is not ohmic conduction.

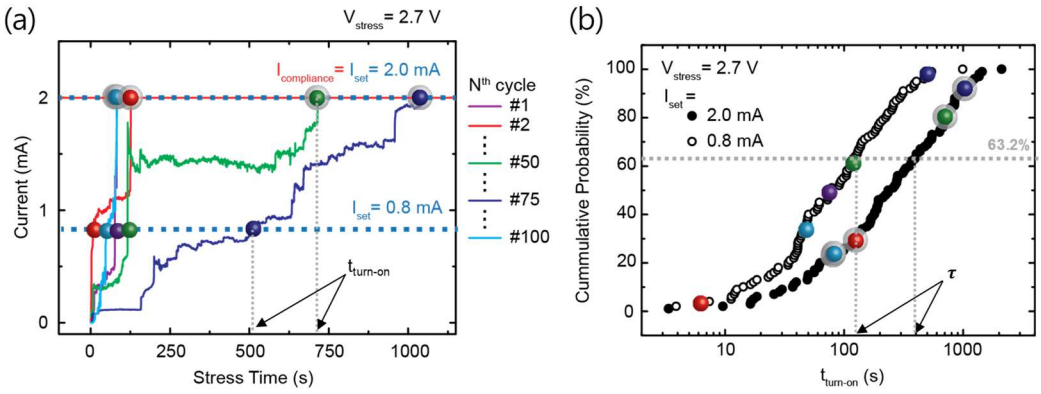

Figure 3.5 (a) Selected current-stress time curves from 100 cycles (shown as different colors) of time-dependent current measurements in the same device under V_{stress} of 2.7 V. I_{set} was chosen as a reference current value for the device in the ON state. The times taken for the device current to reach I_{set}, $t_{turn-on}$, were read from the points represented as the circular marks for each I_{set} of 0.8 mA (circles) and 2.0 mA (shadowed circles). (b) The cumulative probability of the time taken for the device current to reach I_{set}, $t_{turn-on}$, under V_{stress} of 2.7V with I_{set} of 0.8 and

2.0 mA (see the circular marks in (a) for the corresponding data). The horizontal dotted line of 63.2% can be used to read characteristic times, τ, which is discussed later in the manuscript.

I repeated the measurement shown in Figure 3.2b in multiple cycles while applying the same V_{stress} of 2.7 V in the same device to investigate the statistical relevance of the results, as shown in figure 3.5(a). All the current curves increased stepwise, however the time difference between the steps and the height of the steps were all different. In some cycles, the current reached the compliance in a few seconds whereas in other cycles the current reached the compliance after 1,000 seconds. Also, in some cycles, the current reached the compliance in one current step while other cycles showed several current steps before reaching the compliance. Therefore, the turn-on time values have a finite distribution which indicates a probabilistic nature of the turn-on process. This means that the device does not turn on deterministically after a specific voltage or energy requirement is met.[23] It is also obvious that the turn-on process occurs through discrete events in which the current abruptly changes. The percolation conducting path models[13,16] may explain the experimental results above. Every step increase in the current may represent a new current path formation. Each current path has a different resistance, which is reflected in the different heights of the current steps.

For a deeper understanding of the turn-on process, I collected the time, $t_{turn\text{-}on}$, taken to reach a specific current value, I_{set} (see figure 3.5(a)), by conducting the same measurements for different V_{stress}. I ran 100 measurement cycles for different V_{stress} varying from 2.7 V to 3.2 V with an interval of 0.1 V and I read $t_{turn\text{-}on}$ values for six different I_{set} values of 0.2, 0.4, 0.8, 1.2, 1.6, and 2.0 mA. Figure 3.5(b) shows two representative cumulative probability graphs of $t_{turn\text{-}on}$ values which were measured at V_{stress} of 2.7 V and

I_{set} of 0.8 and 2.0 mA. The two graphs look similar, but the graph for I_{set} of 0.8 mA shifted to the smaller $t_{turn\text{-}on}$ direction compared to the graph for 2.0 mA. This is because if one sets a smaller I_{set}, the memory device will reach ON state earlier at a given V_{stress}. A complete data set of cumulative probability distributions for different V_{stress} and I_{set} values can be found in figure 3.6 and 3.7. Figure 3.6(a)-(f) show the full data of the cumulative probability of $t_{turn\text{-}on}$ values. When I_{set} increased, the cumulative probability curves of $t_{turn\text{-}on}$ just shifted to the right without changing the slope under different V_{stress} in these plots. This means that I_{set} does not affect the shape of the distribution of $t_{turn\text{-}on}$. Figure 3.7(a)-(f) contain the same data with Figure 3.6(a)-(f) but these show the V_{stress} dependence of the distribution of $t_{turn\text{-}on}$ values with fixed I_{set}. As the V_{stress} increased, the cumulative distribution curves of $t_{turn\text{-}on}$ values shifted to the left and the slopes became steeper for the all I_{set}, representing a shorter τ and larger β.

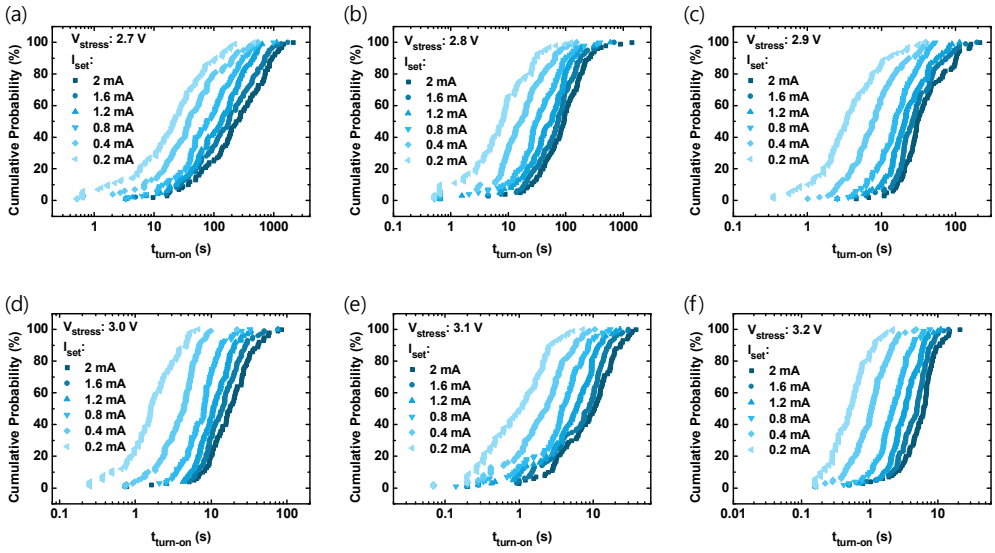

Figure 3.6 I_{set} (from 0.2 mA to 2 mA) dependence of cumulative probability of $t_{turn\text{-}on}$ values according to different V_{stress} of (a) 2.7 V, (b) 2.8 V, (c) 2.9 V, (d) 3.0 V, (e) 3.1 V, and (f) 3.2 V.

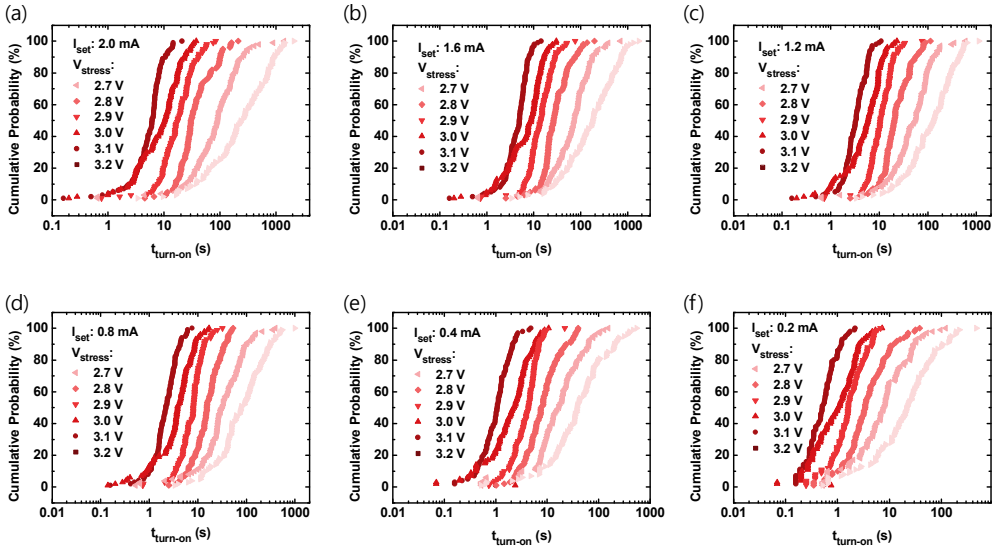

Figure 3.7 V_{stress} dependence of cumulative probability distribution curves of $t_{turn-on}$ values according to different I_{set} of (a) 2.0 mA, (b) 1.6 mA, (c) 1.2 mA, (d) 0.8 mA, (e) 0.4 mA, and (f) 0.2 mA.

Note that I observed no significant device degradation throughout the cycles because $t_{turn-on}$ showed no dependence on the number of cycles. For example, the $t_{turn-on}$ for the 2nd cycle was ~120 s whereas $t_{turn-on}$ for the 50th and the 100th cycle was ~700 s and ~100 s, respectively (see Figure 3.5a and b). The probabilistic nature of the time-dependent switching event can be analyzed by fitting the distribution of $t_{turn-on}$ values with the Weibull distribution. The Weibull distribution is one of the extreme value distributions[24] which has been widely used as an empirical law for describing the electrical breakdown phenomenon of a variety of insulators ranging from oxides to polymers via percolation leakage paths.[18-22] The following equation relates the cumulative probability of $t_{turn-on}$ according to Weibull distribution,

$$F(t) = 1 - \exp\left(-\left(\frac{t}{\tau}\right)^{\beta}\right), \qquad (3.1)$$

where β is the shape parameter and τ is the characteristic turn-on time. In order to assess

whether our experimental data follow the Weibull distribution, I plotted a linearized form of F, defined as $W = \ln(-\ln(1-F))$ as a function of $t_{turn\text{-}on}$. **Figure 4**a and b show that the plots of $t_{turn\text{-}on}$ values for various I_{set} (under a constant V_{stress}) and for various V_{stress} (under a constant I_{set}) can all be fitted linearly. The slopes of these linear lines represent β which is related to the width of the distribution of $t_{turn\text{-}on}$, i.e. a larger β represents a narrower distribution of $t_{turn\text{-}on}$ for a given τ.

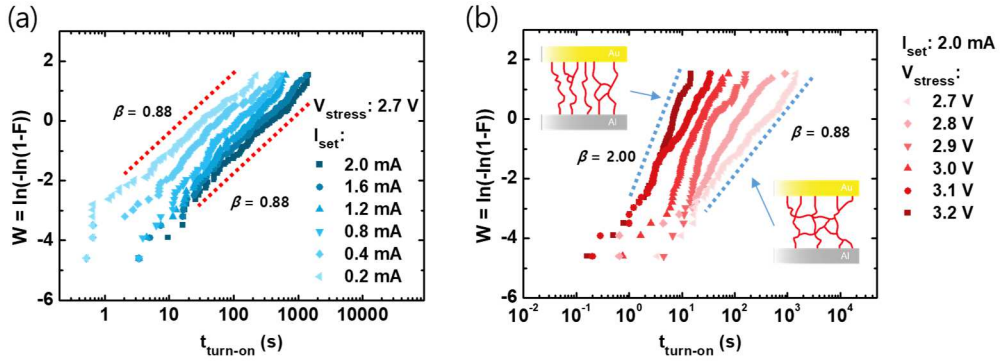

Figure 3.8 A linear fitting for Weibull plots of $t_{turn\text{-}on}$ (a) under V_{stress} of 2.7 V with six different I_{set} and (b) under six different V_{stress} with I_{set} of 2.0 mA. The slopes of the fitted lines indicate the shape parameter, β, of the Weibull distribution. The insets in (b) are schematic representation of different networks of the current paths formed under different V_{stress}.

I investigated the physical meaning of β and τ in the switching process by analyzing their dependence on V_{stress} and I_{set}. Figure 3.8(a) shows that β has a little dependence on I_{set} since the lines for different I_{set} were fitted linearly with similar slopes. On the other hand, β changed depending on V_{stress}; β increased as V_{stress} increased (Figure 3.8(b)). The fitted β varied from 0.88 at V_{stress} of 2.7 V to 2.00 at 3.2 V. Figure 3.9 shows the full data of β. I can see that β does not depend on I_{set} from Figure 3.9(a). However, it is obvious that β has some correlation with V_{stress} (see Figure 3.9(b)). For the range of V_{stress} from 2.7 V to 3.0 V,

β increased as V_{stress} increased. When V_{stress} is larger than 3.0 V, it appears as if the linear correlation between β and V_{stress} disappears, which might be an indication that the memory devices are approaching NDR where the devices begin to switch off.

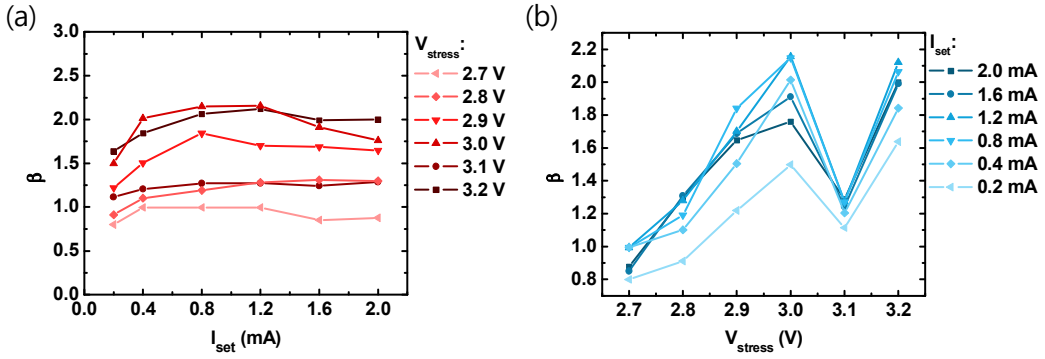

Figure 3.9 The variation of β for different (a) I_{set} and (b) V_{stress}.

The change of β with respect to V_{stress} may indicate the nature of the resistive switching process in the memory devices. The best analogy can be taken from the percolation model for an electrical breakdown in insulating polymers,[19,25,26] which has been explained as either a percolation-like breakdown or a filamentary-like breakdown.[27,28] The insets of Figure 3.8(b) show the schematics that represent two different resulting networks of the device in LRS. The percolation current path formation may have a preferred direction of formation according to the direction of the applied electric field. When V_{stress} becomes larger, the percolation current path formation is more directional along the field, which would tend to form more localized current paths. This is reflected in the higher value of β at larger V_{stress}.

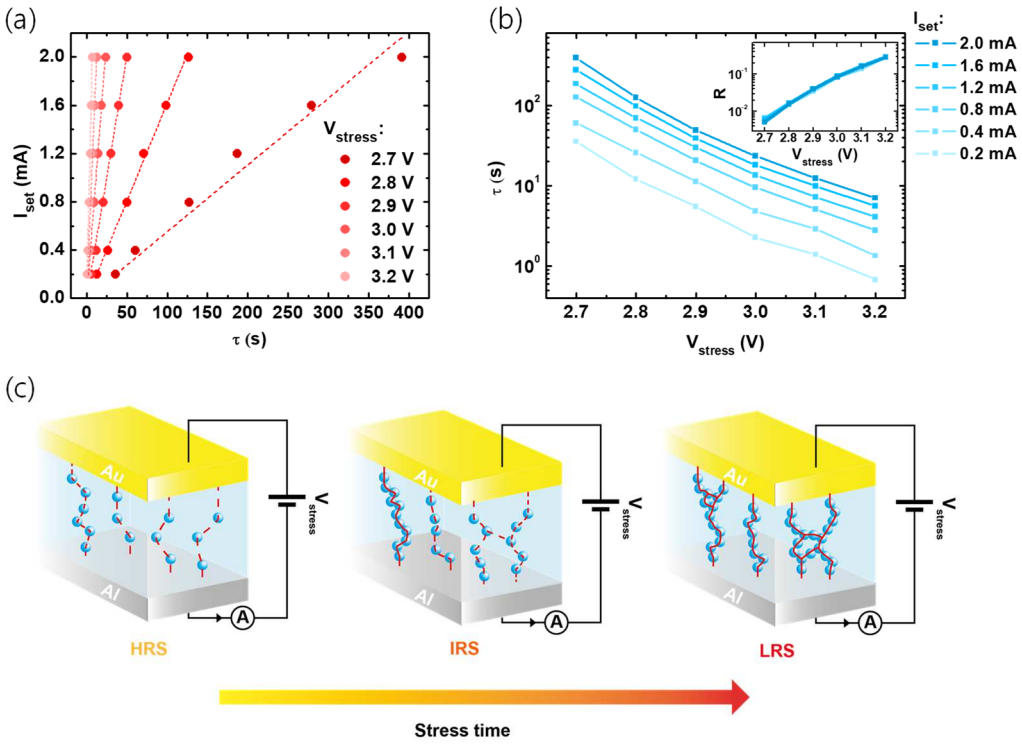

Figure 3.10 Dependence of the characteristic turn-on time, τ, on (a) I_{set} under different V_{stress} and (b) V_{stress} for different I_{set}. The calculated errors in τ are too small to be shown in the graph. The inset in (b) shows the dependence of the rate of current increase over time, R, on V_{stress}. (c) A schematic representation of the overall turn-on process under a constant V_{stress} evolving from HRS (left) to LRS (right).

I now investigate the physical meaning of τ by analyzing its dependence on V_{stress} and I_{set}. τ is calculated from the linear fitting of the linearized Weibull distribution plot in Figure 3.8(a) according to Equation (3.1). Figure 3.10(a) shows how τ changes with I_{set} under different V_{stress}. Obviously, the larger the I_{set}, the larger the τ. The relationship between τ and I_{set} seems linear. Note that τ is a representative value of $t_{turn\text{-}on}$, which is the value at 63.2% in the cumulative distribution of $t_{turn\text{-}on}$. The τ values are indicated by the arrows in Figure 3(b). τ could be considered similar to the mean value of all $t_{turn\text{-}on}$

values. The apparent relationship between τ and I_{set} indicates that the irregular current increases observed in Figure 3(a) are not completely random but follow a particular statistical behavior. I can connect this result to the rate of the current increase at a given time, R, which can be represented as $R = \frac{\Delta I_{set}}{\Delta \tau}$. Since τ increases linearly with I_{set}, R can be simply reduced to $R = \frac{\Delta I_{set}}{\Delta \tau} \cong \frac{I_{set}}{\tau}$. Thus, R is constant for the OFF state and all the IRSs when V_{stress} is constant. On the other hand, I observed that the current did not increase any more when it reached a specific current value of the ON state, even though V_{stress} was applied for a long time. According to Figure 3.10(a) in the main manuscript, the current seems to increase continuously even after reaching the ON state if V_{stress} does not disappear. However, I found that the currents did not increase any more when it reached certain values of ON states (Figure 3.11). This means that there are certain points beyond which the rate of the current increase over time, R, changes to zero. This means that R is constant during the turn-on process until the device reaches the maximum current state beyond which R changes to zero.

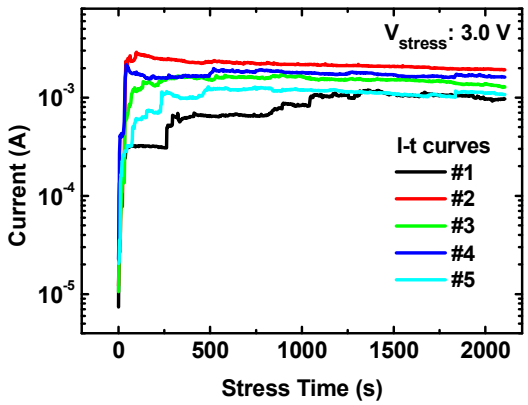

Figure 3.11 Current-stress time curves under V_{stress} of 3.0 V without compliance.

Figure 3.10(a) shows that the slopes of the I_{set} versus τ graphs increased as the V_{stress} increased, which means that the R increased with V_{stress}. The current increase over time can be interpreted as a formation of new current paths. This indicates that the current path formation rate was faster for larger V_{stress} since I_{set} increased rapidly with τ for large values of V_{stress}. Figure 3.10(b) shows the same data as Figure 3.10(a) but it displays a direct dependence of τ on V_{stress}. When V_{stress} linearly increased, τ exponentially decreased. This means that the current path formation rate exponentially depends on V_{stress} (see the inset of Figure 3.10(b)).

There are theoretical models which account for time-dependent dielectric breakdown that could be seen analogous to our observation.[29-32] Although I can not specify which model fully matches our data due to the limited range of V_{stress}, the common feature of the existing models (e.g. $\tau \propto \exp(-\sqrt{E})$,[27] $\tau \propto \exp(1/\mathrm{E})$,[29] and $\tau \propto \exp(-\mathrm{E})$,[33] where E is electric field) is that they are all based on the electric breakdown via percolation current paths.

On the other hand, the exponential dependence of τ on E is highly relevant for the memory device operation, especially in writing and reading processes via voltage pulse operation. Our results predict that τ is 5.49×10^{10} s for V_{stress} of 0.3 V which is a reading voltage used for the device. During the reading operation of the OFF state, the probability of turn-on is 1.02×10^{-9} % for a reading voltage pulse of 0.3 V with a pulse width of 1 ms. This is why the memory devices are highly unlikely to turn on during the reading operation at 0.3 V. On the other hand, τ is predicted to be 1.91×10^{-4} s for V_{stress} of 4.5 V. The probability of turn-on is 99.8 % for a voltage pulse of 4.5 V with a pulse width of 0.5 ms.

In more detail, the pulse-operation typically consists of three main stages; writing, reading and erasing, which all have different magnitudes of the voltage. The τ values at different V_{stress} can be extracted by using E-model ($\tau \propto \exp(-E)$) for a given V_{stress}. I obtained τ for different V_{stress} from the linear fitting of ln(τ) versus V_{stress} (see Figure 3.12 and Table 3.1). The turn-on probability can then be easily obtained by inputting the τ, β, and t (in this case a pulse width) values in Equation 3.1. However, β is hard to determine exactly because it is difficult to find a clear trend for β in a wide range of V_{stress} (see Figure 3.9(b)). Thus, I simply chose β as 0.8 for V_{stress} = 0.3 V which is the same value of β for V_{stress} = 2.7 V and β as 2.0 for V_{stress} = 4.5 V which is the same value of β for V_{stress} = 3.2 V. Table 3.2 and 3.3 show some representative values of turn-on probability for different pulse widths of reading and writing voltage pulses. The biggest source of error would be assuming the value of β. However, the calculated probability values show a clear trend that the turn-on probability dramatically changes depending on the magnitude of the voltage.

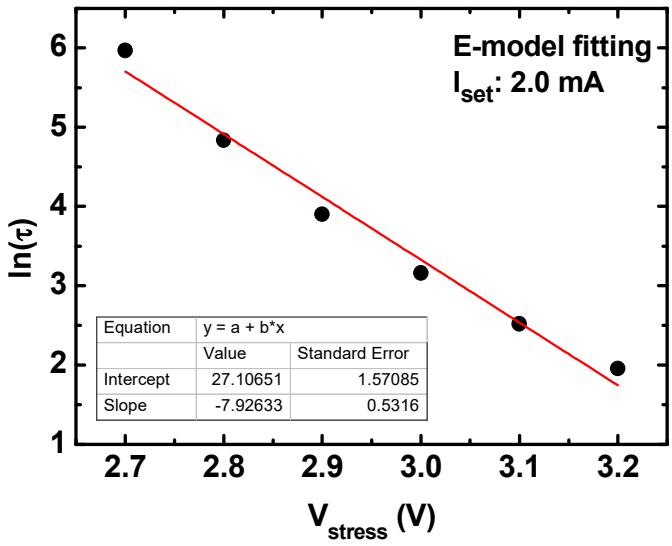

Figure 3.12 A linear fitting graph of ln(τ) versus V_{stress} in order to estimate τ for different V_{stress}. The inset table shows the result of the linear fitting.

Table 3.1 Expectation values of τ according to different V_{stress}

V_{stress} (V)	τ (s)
0.3	5.49×10^{10}
4.0	1.01×10^{-2}
4.5	1.91×10^{-4}
5.0	3.63×10^{-6}

Table 3.2 Expected turn-on probability for different pulse widths of the reading pulse of 0.3 V when τ and β are 5.49×10^{10} and 0.8, respectively.

Pulse width (ms)	Turn-on probability (%)
0.1	1.62×10^{-10}
0.5	5.86×10^{-9}
1.0	1.02×10^{-9}

Table 3.3. Expected turn-on probability for different pulse widths of the writing pulse of 4.5 V when τ and β are 1.91×10^{-4} and 2.0, respectively.

Pulse width (ms)	Turn-on probability (%)
0.1	0.27
0.5	99.8
1.0	100

Unfortunately, these values cannot represent all the PS:PCBM memory devices since the τ value is different for each device. In the worst case, the τ value is different by 2 orders of magnitude among the devices. I investigated the device variation in τ using different devices which had the same structure fabricated under the same condition. However, the extracted τ values were found to be different between the devices (Figure 3.12). The range of the extracted τ values for the measured devices spanned slightly more than one order of magnitude at the same V_{stress}. If the current in the memory flowed through the whole area of the active layer, local variations of memory cells would average out and therefore τ would be the same for all the devices considering that τ is a statistically determined value. Thus, the difference in τ could result from highly localized spatial extent of the current paths. There would be some weak spots (where the localized current paths readily form) in the active layer. The current paths would be formed in the vicinity of these weak spots which could vary from device to device. Note that although the values of τ were different according to the devices, the slopes for the τ versus V_{stress} graphs were almost the same.

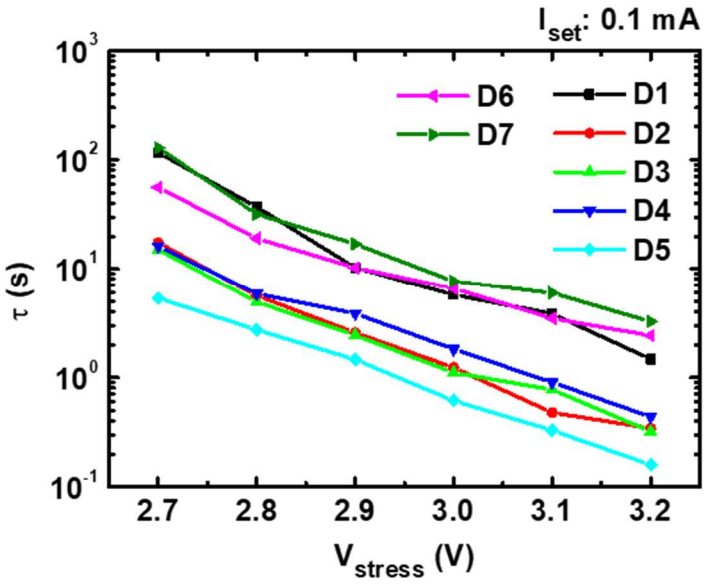

Figure 3.12 Dependence of the change τ on V_{stress} according to different devices

Even after considering the device variation, the results from this work confirm the conclusion from our previous study which demonstrated that voltage pulses of the magnitude 4.5 V and the widths from 5 to 30 ms were sufficient to turn on the memory devices.[23] Therefore, our discovery of the probabilistic nature of the turn-on process enables us to provide guidelines on developing suitable pulse-operation protocols. This allows us to gain a greater control of the device operation by predicting the turn-on probability of the memory devices for various applied voltages and pulse-time-widths, which, in turn, can even be used to justify the previously reported 'trial-and-error' method of operating the devices.

Throughout the discussion, I have not identified the microscopic nature of the percolated conducting paths in the PS:PCBM memory device. Although I cannot provide a complete information on the composition, I have conducted further experiments to investigate the temperature-dependent charge transport and the environmental effect on the

switching process in order to exclude some of the possible candidates. Our analysis suggests that the conducting paths are composed of carbon-rich regions formed by pyrolysis between which tunneling-based conduction occurs.

Although a complete information on the microscopic nature of the conducting paths can not be provided, I have attempted to deduce what constitutes the conducting path of the memory device from the characteristics of the PS:PCBM memory device shown in the experiments below.

A. Conduction mechanism of the PS:PCBM memory devices

I have discovered that the conducting paths are not likely to be metallic filaments (either Au or Al). Firstly, Au is an inert metal which requires a larger electrochemical potential to make filamentary paths for electrochemical metallization processes, compared to reactive metals such as Ag and Al. I also applied a positive voltage bias on the Au electrode (i.e. bottom Al electrode grounded) in order to avoid Al^{3+} ion migration in the film. Secondly, a non-ohmic conduction was seen from I-V curves of the ON state (see the inset of Figure 3.4). Metallic filaments typically show a linear I-V curve (i.e. ohmic conduction) at a lower voltage and a slightly non-linear (concave downward) curve due to an increased resistance by Joule heating at a higher voltage,[35-37] which has been observed in metal-oxide-based unipolar memories. The I-V curves of the LRS in our study showed an opposite trend.

I examined the temperature dependence of the I-V curves while maintaining the memory devices in the LRS and HRS. The I-V curves of the LRS remained almost the same over the measured temperature range, whereas the I-V curves of the HRS showed a thermally activated transport. This indicates that the transport mechanism of the LRS is

completely different from that of the HRS. Possible conduction mechanisms without a significant temperature dependence as shown for the LRS include metallic conduction and tunneling based conduction mechanisms. However, metallic filaments could be eliminated based on the discussion above, and therefore the tunneling based mechanism would be a possible candidate. As shown in Figure 3.13(a), I could describe the conduction in the LRS with a combination of a direct tunneling and Fowler-Nordheim tunneling equation[38] as,

$$I = C_1 V e^{-\frac{2d\sqrt{2m^*\Phi}}{\hbar}} + C_2 V^2 e^{-\frac{4d\sqrt{2m^*}\Phi^{\frac{3}{2}}}{3\hbar qV}}, \quad (3.2)$$

where C_1 and C_2 are constants, q is the electronic charge, m^* is the effective mass, d is the tunneling distance and Φ is the tunneling barrier. Although the good fit can not be a complete proof of tunneling, the fit yields a reasonable physical quantities such as $\Phi \sim 1\text{eV}$ and $\text{d} \sim 1\,\text{nm}$. However, the above equation is by no means a complete description of the tunneling process, since the equation strictly applies to a single tunneling barrier. I expect that the tunneling most probably occurs through multiple barriers, which would explain the temperature-insensitive conduction.

On the other hand, the conduction in the HRS was found to be significantly temperature dependent since the current decreased when the temperature decreased (see Figure 3.13(b)). The I-V curves for the HRS can be described with an ohmic conduction at a lower voltage (below 0.2 V) and a trap-limited space-charge-limited-current (SCLC) at a higher voltage over the entire range of temperatures (see Figure 3.13(b)). The ohmic conduction regime can be explained by a conduction due to a small concentration of thermally generated charge carriers and the SCLC regime can be explained with a SCLC model with an exponentially distributed charge traps,[39,40]

$$I \sim q^{-m}\mu N_{DOS}\left(2m-\frac{1}{m}\right)^m\left(m-\frac{1}{m}\right)^{m-1}\left(\frac{\epsilon_0\epsilon_r}{N_t}\right)^{m-1}V^m/d^{2m-1}, \quad (3.2)$$

where N_t is the density of the trap states, ϵ_0 is the vacuum permittivity, ϵ_r is the dielectric constant, μ is the mobility, and d is the length of the conduction path. Figure 3.13(c) shows that the slope of the I-V curve, m is thermally activated since the occupied trap density would depend on the temperature. As $T \to \infty$, $m = 2$ which is the limiting case for a trap-free SCLC conduction. Therefore, the conduction mechanism switches from a trap-limited thermally activated transport in the HRS (i.e. an intrinsic charge transport in the PS:PCBM film) to a tunneling based conduction in the LRS due to the formation of the percolated conducting paths.

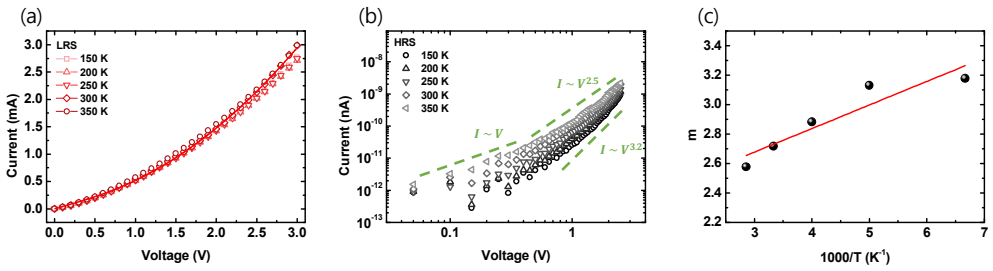

Figure 3.13 (a) The I-V curves over a temperature range from 150 K to 350 K for the LRS in a linear scale with a fit with the Equation 3.2 shown as the solid line and (b) The I-V curves over the same temperature range for the HRS in a log-log plot. (c) The temperature dependence of m in the Equation 3.3 which corresponds to the SCLC model with an exponential trap distribution.

B. Environmental effect on the switching process in PS:PCBM memory devices

I performed the environmental effect on the memory device operation to eliminate the existence of metallic filaments/particles. I discovered that normally operating PS:PCBM devices (shown in Figure 3.14(a)) could not be operated when measured in ambient conditions. When the memory device was exposed to air, the device could not be turned on after the RESEET process (see Figure 3.14(b) and 3.14(c)). However, when the device was put back in vacuum, it operated normally again (see figure 3.14(d)), showing the reversible

effect of oxygen and moisture on the resistive switching. A similar environmental effect has been reported in other organic resistive memory devices with similar unipolar I-V curves.[41] From these experimental results, it can be seen that conducting path formation is a process affected by moisture and oxygen in the ambient atmosphere. The memory devices based on metallic filamentary paths can be operated in ambient conditions.[42-44] The metallic filament/particles formation is mostly caused by electrochemical metallization which is an electrochemical process initiated by metal ion migration in the active channel which would be relatively insensitive to oxygen and moisture.

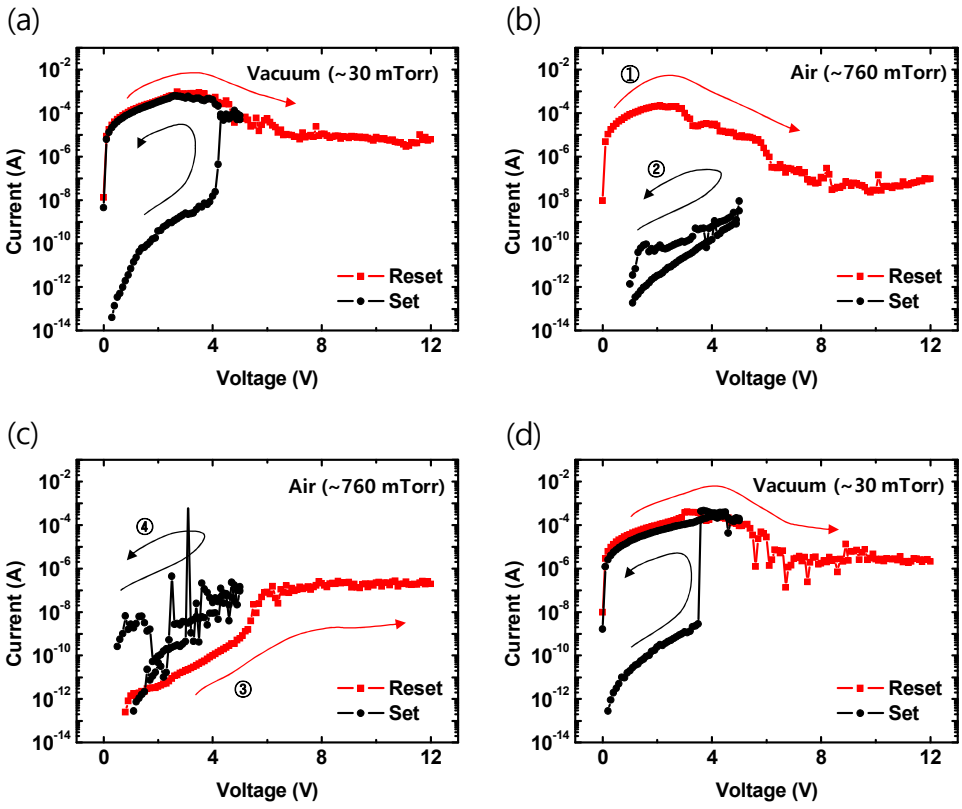

Figure 3.14 The I-V curves of the PS:PCBM memory devices in different environmental conditions: (a) the I-V curve in an initial vacuum condition, (b) the

first I-V curve in an ambient condition, (c) the second I-V curve in the ambient condition and (d) the I-V curve when the device was put back in vacuum condition.

C. Possible formation of carbon-rich regions

Our results shown above provide a strong indication that the conduction mechanism is tunneling-based. However, I have not specified the nature of these states between which the tunneling occurs. Although there are multiple candidates including charge-transfer complexes, metallic particles formed by electromigration and carbonaceous regions formed by pyrolysis due to Joule heating.[45] I can eliminate some of the candidates by our experimental data.

Firstly, the charge-transfer complexes are unlikely to form in PS:PCBM due to the energy-mismatch of around 1 eV between PS ($E_{\mathrm{LUMO}} \approx -3$ eV and $E_{\mathrm{HOMO}} \approx -7$ eV) and PCBM ($E_{\mathrm{LUMO}} \approx -4$ eV and $E_{\mathrm{HOMO}} \approx -6$ eV). This is also supported by a nearly-indifferent OFF current values between the PS:PCBM and PS-only memory devices (Figure 3.2 in the main manuscript and Figure 3.14).

Secondly, from these experimental results, it can be seen that conducting path formation is a process affected by moisture and oxygen in the ambient atmosphere. The memory devices based on metallic filamentary paths can be operated in ambient conditions.[S8-10] The metallic filament/particles formation is mostly caused by electrochemical metallization which is an electrochemical process initiated by metal ion migration in the active channel which would be relatively insensitive to oxygen and moisture. Thus, metallic filamentary/particles are also inappropriate candidates for conducting paths of PS:PCBM memory devices.

On the other hand, the formation of carbon-rich regions within the PS:PCBM film can be resolved with most of our experimental outcomes. Pender and Fleming[46] predicted that

highly-conductive carbon-rich filamentary paths form during the resistive switching in memory devices made of PS due to localized Joule heating that leads to pyrolysis during the soft electrical breakdown. They have reported similar I-V curves for the LRS and IRS to our data shown in inset of Figure 3.4, as well as a temperature-independent resistance of the LRS and an increasing HRS resistance with a decreasing temperature, which indicate that the conduction mechanism is similar in our PS:PCBM devices. I therefore expect that there are highly conductive carbon-rich areas formed[47] during the SET process between which the tunneling conduction occurs according to the model proposed in Equation 3.2.

There are several works which have shown a temperature-independent resistivity of amorphous carbon made from pyrolysis of organic materials.[48,49] In addition, the tunneling between carbon-rich areas can be treated analogously to the conduction in graphite-polymer composites[50] which is described as tunneling between graphite particles above a threshold graphite composition ratio. The resistivity of the tunneling conduction, ρ, can then be modelled as,[51,52] $\rho \propto \sin(\pi c k_B T)/\pi c k_B T$, where c is a function of the applied voltage, k_B is the Boltzman constant and T is the temperature. This predicts that the resistivity is shows a small dependence on T when c is small, which could explain our temperature-dependence data for the LRS. Furthermore, the reason for the oxygen and moisture effect could be due to the reaction between the carbon-rich areas formed during the pyrolysis and the oxygen which would undergo a series of reactions to oxidize the carbon-rich areas.

Finally, I observed a significant dependence of τ on temperature from the measurement of τ over a temperature range from 260 K to 340 K (Figure 3.15(a)). It is shown that τ exponentially increased when the temperature decreased for the same V_{stress} (Figure 3.15(b)). This indicates a strong temperature dependence of τ, considering that τ

changed by two orders of magnitude when temperature changed from 260 K to 340 K for V_{stress} of 3.2 V. When the temperature was as low as 260 K, τ did not reduce significantly even under a high V_{stress} unlike at high temperature (as seen from the slopes of the curves in Figure 3.15(a)). The strong temperature dependence of τ could be explained by a varying degree of thermal dissipation through the metal electrodes at different temperatures. The metal electrodes have much higher thermal conductivity than the PS film (~10^3 higher than PS) and can be treated as a heat reservoir. The lower the temperature, the higher the rate of the heat dissipation through the electrodes. Therefore, a longer time would be needed to acquire the same amount of heat energy to form the carbon-rich region near the electrode, which leads to a longer τ. In addition, there is a contribution from a smaller amount of Joule heating at a lower temperature since the HRS showed a thermally activated transport (E_a ~ 0.1 eV, see Figure 3.15(c)).

Although the formation of carbon-rich regions explains the various properties of PS: PCBM memory devices, there also exist some properties of the devices that are difficult to account for in the formation of carbon-rich regions. For example, it does not explain the constant R regardless of current states. The formation of carbon-rich regions is induced by Joule heating which is caused by a current flow. Therefore, I can infer that R should increase when the current increases, just as R increases with an increasing voltage. However, as I showed in Figure 3.10(a) and inset of Figure 3.10(b) in main manuscript, R does not change according to I_{set}.

I compared the characteristics of the PS: PCBM memory devices with those already presented to explain the microscopic nature. As a result, I found that the formation of carbon-rich regions was the most convincing explanation. However, further studies are needed to clarify the microscopic nature of the PS:PCBM memory devices in the future.

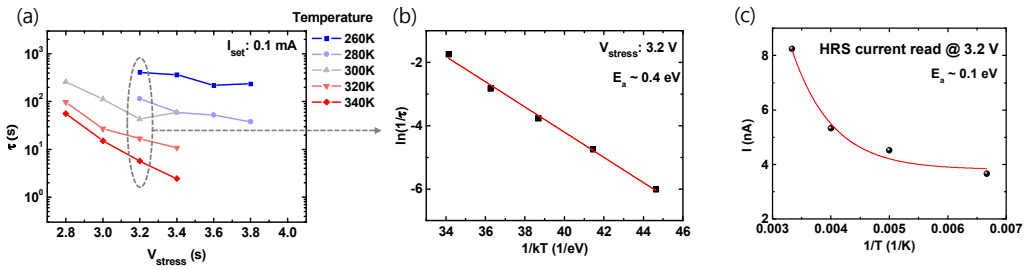

Figure 3.15 (a) The dependence of τ on V_{stress} at different temperatures from 260 K to 340 K for I_{set} of 0.1 mA. (b) The Arrhenius plot of τ under V_{stress} of 3.2V and I_{set} = 0.1 mA. (c) The current of the HRS at different T extracted at 3.2 V by fitting the data shown in Figure 3.13(b).

Now, I suggest an overall picture of the turn-on process. During the SET process, a trap-limited conduction occurs in the highly-resistive HRS (see 'HRS' in Figure 3.10(c)) which begins to initiate the formation of carbon-rich regions via Joule-heating-induced-pyrolysis. As a result, some of the carbon-rich regions become strongly connected which forms a current path in which the tunneling transport occurs, whereas other current paths remain weakly connected. This results in a slightly lower overall resistance and the current in the device is dominated by the well-connected current paths. The device becomes fully ON (i.e. LRS) when more carbon-rich areas are generated to form a larger number of strongly connected current paths ('LRS' in Figure 3.10(c)).

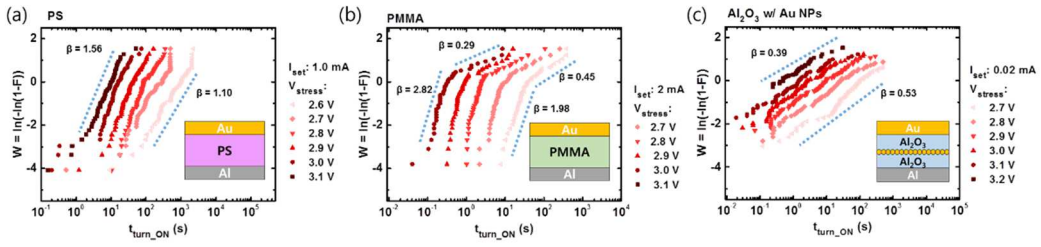

Figure 3.16 A linear fitting for the Weibull plots of $t_{turn\text{-}on}$ with the memory devices made of 3 other materials: (a) PS, (b) PMMA, and (c) Al_2O_3 with Au nanoparticles.

In order to check whether the probabilistic nature of the resistive switching process is universal for other active materials, I conducted the same tests on three different materials; PS, poly(methyl methacrylate) (PMMA), and Al_2O_3 with Au nanoparticles (NPs). The memory devices with the different active materials also turned on under a constant V_{stress} below the threshold voltage, showing similar behaviors of the stepwise current increase.

Figure 3.17(a) shows I-V characteristics of the memory devices made with PS as an active layer. Even without the nanocomposite materials, the devices showed a unipolar memory property. Under a constant voltage stress, the PS memory devices showed similar properties as the PS:PCBM memory devices; the current increased with several steps until it finally reached the compliance (Figure 3.17(b)).

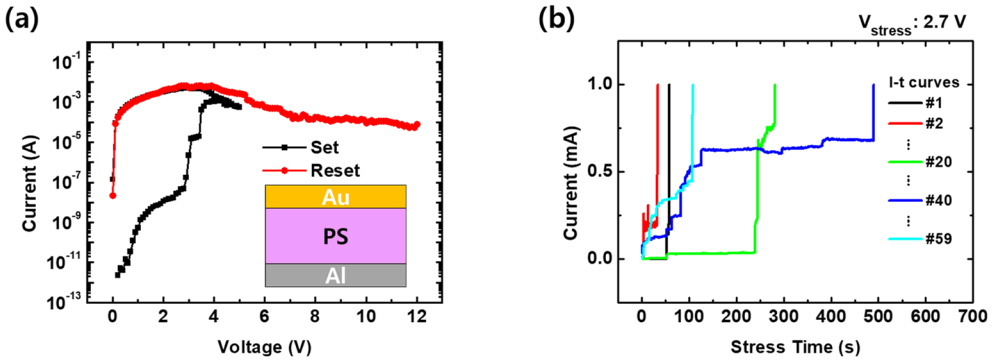

Figure 3.17 (a) A representative I-V graph of the memory devices made with PS as an active layer. (b) Current-stress time curves under V_{stress} of 2.7 V

In order to find whether the memory devices with other organic materials show the same stepwise increase of current under a constant voltage stress, I made resistive memory

devices using PMMA as an active layer. Figure 3.18(a) shows that the memory devices with PMMA had a typical unipolar resistive memory property. When a constant voltage stress was applied, the memory devices also showed similar properties; the current increased stepwise over time (Figure 3.18(b)).

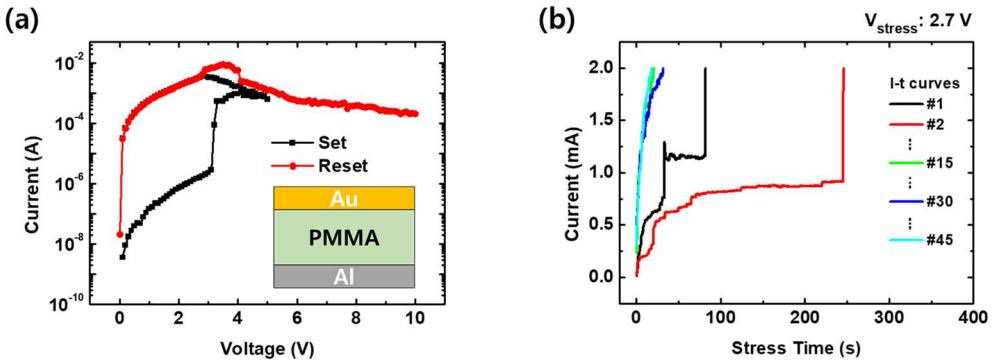

Figure 3.18 (a) A representative I-V graph of the memory devices made with PMMA as an active layer. (b) Current-stress time curves under V_{stress} of 2.7 V

The memory devices made of Al_2O_3 with Au nanoparticles (NPs) as an active layer were studied to investigate potential differences in the memory characteristics between organic (studied in the previous sections) and inorganic materials. The inorganic resistive memory devices showed similar I-V curves with the previous organic memory devices (Figure 3.19(a)). ON and OFF currents were both lower than the organic memory devices but the shape of the curves were similar to that of the organic devices. The inorganic memory devices also showed stepwise increase of current under a constant voltage stress (Figure 3.19(b)). Thus, I could guess that the property of the stepwise current increase is a universal property, regardless of the active material of unipolar memory devices that show NDR.

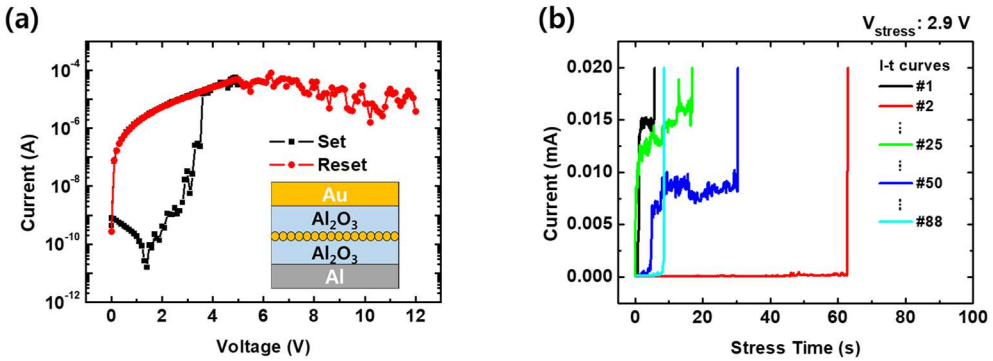

Figure 3.19 (a) A representative I-V graph of the memory devices made with Al_2O_3 with Au NPs as an active layer. (b) Current-stress time curves under V_{stress} of 2.9 V

The measured $t_{turn\text{-}on}$ values of the memory devices made of all the different active materials could also be described by the Weibull distribution, as shown in **Figure 3.16**. The exponential dependence of τ and R with V_{stress} was also consistently observed for the different materials of PS, PMMA, and Al_2O_3 with Au NPs which support the percolated network model, like in PS:PCBM.

In order to check whether the slope of of τ versus V_{stress} is an intrinsic parameter that depends on active materials, τ of the three devices with the three different materials were obtained. Note that the values of τ themselves are not important here because those vary on how I_{set} is selected. I have chosen I_{set} based on the different ON current for the different materials. However, the slopes of τ versus V_{stress} do not depend on I_{set} (Figure 3.10(b)). Interestingly, the slopes showed almost the same values independent of the materials (Figure 3.20(a)). This means that the voltage dependence of R is the almost same for all the four different materials (Figure 3.20(b)). This could reflect the nature of a common underlying resistive switching mechanism of the unipolar memory devices.

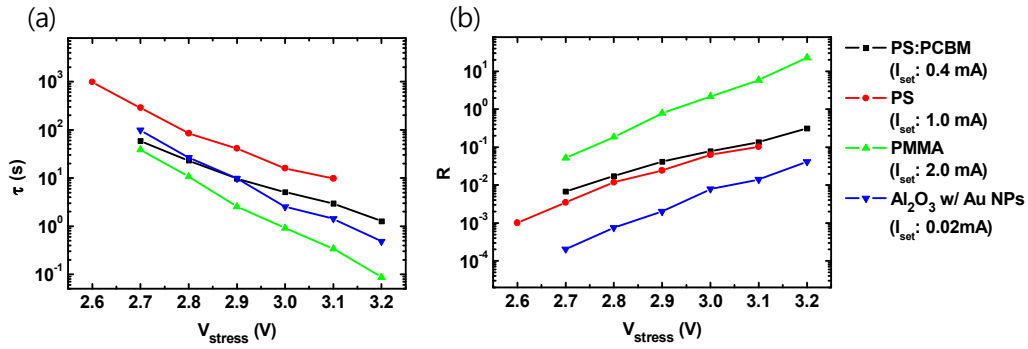

Figure 3.20 Dependence of (a) τ and (b) R on V_{stress} according to devices of different active materials and I_{set} chosen as shown in the legend.

Therefore, our results show that the different materials all show a probabilistic formation of percolated conducting paths. The observation implies an underlying common resistive switching properties in the different materials with different materialistic properties (i.e. varying from organic insulators, organic nanocomposites to inorganic insulators), as expected from the similar I-V curves of the memory devices (see Figure 3.17 to 3.19).

However, our results also reveal subtle differences between the resistive switching in the different material systems. The shape parameter, β, was found to be different for different materials which reflect different shapes of the percolation network of the conducting paths. For example, the correlation of β to the properties of the percolation network is seen clearly in the case for PMMA (Figure 3.16(b)), which shows degradation after the 11th cycle. After the degradation, the OFF current increases by an order of magnitude which may be due to the remaining strongly connected current paths. Concurrently, β increases sharply by an order of magnitude which indicates the formation of more localized conducting paths around these remaining strongly connected current paths, after the degradation. Although the change in β with respect to V_{stress} was similar for

the devices with PS and PMMA cases, in the case of Al_2O_3 with Au NPs, the dependence of β on V_{stress} was not clear. A similar independency of β on V_{stress} has been previously reported for time-dependent dielectric breakdown measurements of inorganic gate dielectric materials for field-effect transistors.[18,34]

Our results demonstrate that both the experimental and statistical analysis techniques used for investigating time-dependent resistive switching behaviors can be applied to various material systems. This, combined with further experiments to identify the microscopic origin of the conducting paths, will be a powerful tool for understanding the resistive switching mechanism in memory devices.

3.3. Experiments

Device Fabrication: Al bottom electrodes with line-widths of 100 μm and a thickness of 30 nm were deposited by thermal evaporation through a shadow mask on cleaned SiO_2/Si substrates. UV-ozone was illuminated to clean the substrate and enhance the film quality of spin-coated PS:PCBM. Four different materials were used as the active layer - PS:PCBM, PS, PMMA and Al_2O_3 with Au NPs. PS:PCBM and PS were made from solution mixtures of 32 mg of PS and 2.5 mg of PCBM dissolved in 4 mL of chlorobenzene and 8 mg of PS was dissolved in 1 mL of chlorobenzene, respectively. The solutions were spin coated onto the bottom electrodes in ambient condition and at a rate of 2000 rpm for 40 seconds. Then, the samples were soft baked at 60 ˚C for 10 minutes. The contact pads of the bottom electrodes were exposed by an acetone-soaked Q-tip cotton swab. The samples were hard baked at 120 ˚C for 60 minutes. The PMMA layers were made from a solution of 1% of PMMA with the molecular weight of 950,000 dissolved in anisole. The solution was spin coated onto the bottom electrodes at the rate of 4000 rpm for 40 seconds. After the exposure of the contact pads for contact with the swab, the samples were baked at 120 ˚C for 1 minute. In case of the active layers of Al_2O_3/Au NPs/Al_2O_3, they were sequentially deposited through the same shadow mask by an electron beam evaporator. The thicknesses of the active layers were ~40 nm for PS:PCBM, ~40 nm for PS, ~40 nm for PMMA, and 20 nm/2 nm/20 nm for Al_2O_3/Au NPs/Al_2O_3 layers. The top gold electrodes with line-widths of 100 μm and a thickness of 30 nm were deposited through a shadow mask by electron beam evaporation for all the devices. The memory cell size was defined as 100 μm × 100 μm.

Note that I treated the substrate and bottom Al electrode with UV-ozone to enhance the PS:PCBM film quaility and the device yield. One may concern that AlO_x formed on the Al electrode due to the UV-ozone treatment affects electrical characteristics of the memory

devices. However, Figure 3.21 shows the treatment did not significantly affect electrical characteristics of the memory devices, although the device yield was higher due to a higher film quality.

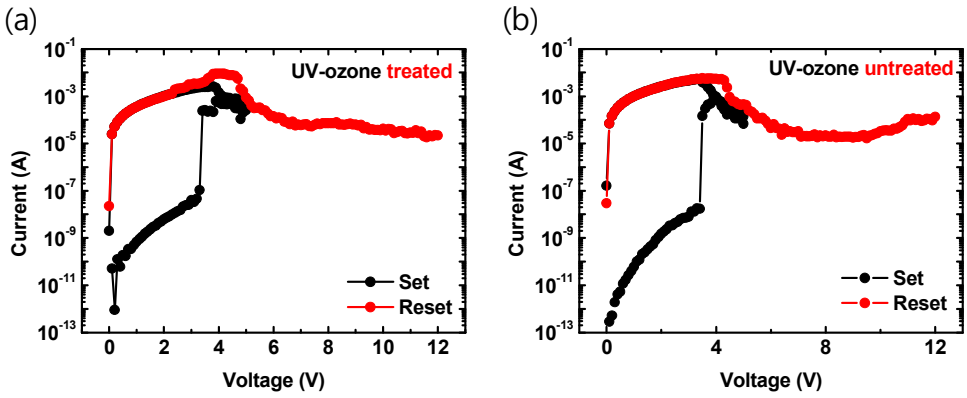

Figure 3.21 Current-voltage characteristics of the resistive memory devices (a) with UV-ozone treatment and (b) without UV-ozone treatment.

Device characterization: All the electrical measurements were performed in a vacuum environment (~10^{-3} Torr) with a semiconductor parameter analyzer (Keithley 4200 SCS). The scan rate of the voltage sweep in I-V measurements was typically 0.54 V/s. The bias voltage was applied to Au top electrode while the Al bottom electrode was grounded. One cycle of the measurement was defined as a set of the current-stress-time scans from 2.7 V to 3.2 V (i. e., 2.7 V stress, RESET, 2.8 V stress, RESET, …, 3.2 V stress, and then RESET). In overall, 100 cycles of the voltage-stress measurement were conducted for the PS:PCBM devices. The purpose of the measurement sequence was to reduce the systematic errors related to the voltage-stress effect (e.g. device degradation).

3.4. Conclusion

I investigated the time dependent turn-on phenomena of unipolar resistive memory devices by performing voltage-stress measurements. The turn-on time was observed to have a finite distribution which reflects an intrinsic probabilistic nature of the turn-on process. By statistically analyzing the turn-on time distribution, I found that the current paths formed a percolation network with shape properties and formation rate both of which vary significantly with the stress voltage. Our results could be applied to estimate the turn-on probability of the memory devices during writing and reading processes during the pulse operation, which strengthen the practical relevance of this study for developing suitable operation protocols for unipolar resistive memory devices. I discovered that the probabilistic nature of the percolated conducting paths formation was shared between unipolar resistive memory devices with different active materials (PS, PMMA, and Al_2O_3 with Au NPs). Our results indicate that controlling these percolation current paths could enhance the electrical stability of the memory devices, which would be a key element for making practical memory devices. The analysis based on Weibull statistics presented in the study may also be applicable for investigating the resistive switching properties of various other types of resistive memories.

References

[1] H. E. Katz, J. Huang, 2009, *Annu. Rev. Mater. Res.* **39** 71.

[2] T. W. Kelley, P. F. Baude, C. Gerlach, D. E. Ender, D. Muyres, M. A. Haase, D. E. Vogel, S. D. Theiss, 2004 *Chem. Mater.* **16** 4413.

[3] T. Lee, Y. Chen, 2012 *MRS Bull.* **37** 144.

[4] C. Wang, P. Gu, B. Hu, Q. Zhang, 2015 *J. Mater. Chem. C* **3** 10055.

[5] B. Cho, S. Song, Y. Ji, T. W. Kim, T. Lee, 2011 *Adv. Funct. Mater.* **21** 2806.

[6] S. Goswami, A. J. Matula, S. P. Rath, S. Hedström, S. Saha, M. Annamalai, D. Sengupta, A. Patra, S. Ghosh, H. Jani, S. Sarkar, M. R. Motapothula, C. A. Nijhuis, J. Martin, S. Goswami, V. S. Batista, T. Venkatesan, 2017 *Nat. Mater.* **16** 1216.

[7] S. Song, B. Cho, T. W. Kim, Y. Ji, M. Jo, G. Wang, M. Choe, Y. H. Kahng, H. Hwang, T. Lee, 2010 *Adv. Mater.* **22** 5048.

[8] Y. Song, J. Jang, D. Yoo, S.-H. Jung, H. Jeong, S. Hong, J.-K. Lee, T. Lee, *J. Nanosci.* 2016 *Nanotechnol.* **16** 6350.

[9] T. W. Kim, D. F. Zeigler, O. Acton, H. L. Yip, H. Ma, A. K. Y. Jen, 2012 *Adv. Mater.* **24** 828.

[10] T.-W. Kim, H. Choi, S.-H. Oh, G. Wang, D.-Y. Kim, H. Hwang, T. Lee, 2009 *Adv. Mater.* **21** 2497.

[11] L. D. Bozano, B. W. Kean, M. Beinhoff, K. R. Carter, P. M. Rice, J. C. Scott, 2005 *Adv. Funct. Mater.* **15** 1933.

[12] S. Nau, S. Sax, E. J. List-Kratochvil, 2014 *Adv. Mater.* **26** 2508.

[13] Y. Song, H. Jeong, J. Jang, T.-Y. Kim, D. Yoo, Y. Kim, H. Jeong, T. Lee, 2015 *ACS Nano* **9** 7697.

[14] Y. Busby, S. Nau, S. Sax, E. List-Kratochvil, J. Novak, R. Banerjee, F. Schreiber, J.-J. Pireaux, 2015 *J. Appl. Phys.* **118** 075501.

[15] C. Wolf, S. Nau, S. Sax, Y. Busby, J.-J. Pireaux, E. J. List-Kratochvil, 2015 *Japanese Journal of Applied Physics* **54** 120301.

[16] Y. Song, H. Jeong, S. Chung, G. H. Ahn, T.-Y. Kim, J. Jang, D. Yoo, H. Jeong, A. Javey, T. Lee, 2016 *Sci. Rep.* **6** 33967.

[17] W. Weibull, 1951 *J. Appl. Mech.* **103** 293.

[18] C. Monsérié, P. Mortini, G. Pananakakis, G. Ghibaudo, 1993 *Microelectron. J.* **24** 353.

[19] J. Stathis, 1999 *J. Appl. Phys.* **86** 5757.

[20] G.-H. Buh, I. Hwang, B. H. Park, 2009 *Appl. Phys. Lett.* **95** 142101.

[21] T. K. Wong, 2012 *Materials* **5** 1602.

[22] Q. Wu, B. Yin, K. Zhou, J. Wang, J. Gao, presented at Semiconductor Technology International Conference (CSTIC), 2017 China.

[23] J. Jang, Y. Song, D. Yoo, K. Cho, Y. Kim, J. Pak, M. Min, T. Lee, 2015 *Adv. Electron. Mater.* **1** 1500186.

[24] L. A. Dissado, 2002 *IEEE Trans. Dielectr. Electr. Insul.* **9** 860.

[25] K. Wu, L. A. Dissado, T. Okamoto, 2004 *Appl. Phys. Lett.* **85** 4454.

[26] P. M. Duxbury, P. L. Leath, 1987 *J. Phys. A: Math. Gen.*, **20** L411.

[27] K. Wu, Y. Wang, Y. Cheng, L. A. Dissado, X. Liu, 2010 *J. Appl. Phys.* **107** 064107.

[28] K. Wu, Y. Cheng, 2007 *J. Appl. Phys.* **101** 064113.

[29] L. Zhao, Z. Tőkei, K. Croes, C. J. Wilson, M. Baklanov, G. P. Beyer, C. Claeys, 2011 *Appl. Phys. Lett.* **98** 032107.

[30] J. Lloyd, E. Liniger, T. Shaw, 2005 *J. Appl. Phys.* **98** 084109.

[31] R. S. Achanta, J. L. Plawsky, W. N. Gill, 2007 *Appl. Phys. Lett.* **91** 234106.

[32] P. D. Beale, P. M. Duxbury, 1988 *Physical Review B* **37** 2785.

[33] P. E. Nicollian, *Physics of trap generation and electrical breakdown in ultra-thin SiO2 and SiON gate dielectric materials*, University of Twente, 2007.

[34] A. Martin, P. O'Sullivan, A. Mathewson, 1998 *Microelectron. Reliab.* **38** 37.

[35] J. S. Lee, S. Lee, T. W. Noh, 2015 *Appl. Phys. Rev.* **2** 031303.

[36] D. B. Strukov, F. Alibart, R. S. Williams, 2012 *Appl. Phys. A* **107** 509.

[37] D. Ielmini, R. Bruchhaus, R. Waser, 2011 *Phase Transitions* **84** 570.

[38] J. Ouyang, C.-W. Chu, C. R. Szmanda, L. Ma, Y. Yang, 2004 *Nat. Mater.* **3** 918.

[39] A. Rose, 1955 *Physical Review* **97** 1538.

[40] D. Joung, A. Chunder, L. Zhai, S. I. Khondaker, 2010*Appl. Phys. Lett.* **97** 093105.

[41] C. Wolf, S. Nau, S. Sax, Y. Busby, J.-J. Pireaux, E. J. List-Kratochvil, 2015 *Japanese Journal of Applied Physics* **54** 120301.

[42] F. Zhuge, S. Peng, C. He, X. Zhu, X. Chen, Y. Liu, R.-W. Li, 2011 *Nanotechnology* **22** 275204.

[43] C.-N. Peng, C.-W. Wang, T.-C. Chan, W.-Y. Chang, Y.-C. Wang, H.-W. Tsai, W.-W. Wu, L.-J. Chen, Y.-L. Chueh, 2012 *Nanoscale Res. Lett.* **7** 559.

[44] G. Casula, P. Cosseddu, Y. Busby, J.-J. Pireaux, M. Rosowski, B. T. Szczesna, K. Soliwoda, G. Celichowski, J. Grobelny, J. Novák, 2015 *Org. Electron.* **18** 17.

[45] J. C. Scott, L. D. Bozano, 2007 *Adv. Mater.* **19** 1452.

[46] L. Pender, R. Fleming, 1975 *J. Appl. Phys.* **46** 3426.

[47] F. H. Winslow, W. Matreyek, 1956 *"J. Polym. Sci., Part A: Polym. Chem."* **22** 315.

[48] S. Mrozowski, 1952 *Physical Review* **85** 609.

[49] W. Bücker, 1973 *J. Non-Cryst. Solids* **12** 115.

[50] A. Celzard, E. McRae, J.-F. Marêché, G. Furdin, B. Sundqvist, 1998 *J. Appl. Phys.* **83** 1410.

[51] R. Stratton, G. Lewicki, C. Mead, 1966 *J. Phys. Chem. Solids* **27** 1599.

[52] T. E. Hartman, J. S. Chivian, 1964 *Physical Review* **134** A1094.

Chapter 4. Controllable deposition of organic metal halide perovskite films with wafer-scale uniformity by single source flash evaporation

In this thesis, I described evaporation method of perovskite films which can be used for flexible resistive memory devices. Conventional solution-processing techniques such as the spin-coating method have been used successfully to reveal excellent properties of organic-inorganic halide perovskites (OHPs) for optoelectronic devices such as solar cell and light-emitting diode, but it is essential to explore other deposition techniques compatible with large-scale production. Single-source flash evaporation technique, in which a single source of materials of interest is rapidly heated to be deposited in a few seconds, is one of the candidate techniques for large-scale thin film deposition of OHPs. In this work, I investigated the reliability and controllability of the single-source flash evaporation technique for methylammonium lead iodide ($MAPbI_3$) perovskite. In-depth statistical analysis was employed to demonstrate that the $MAPbI_3$ films prepared via the flash evaporation have an ultrasmooth surface and uniform thickness throughout the 4-inch wafer scale. I also show that the thickness and grain size of the $MAPbI_3$ film can be controlled by adjusting the amount of the source and number of deposition steps. Finally, the excellent large-area uniformity of the physical properties of the deposited thin films can be transferred to the uniformity in the device performance of $MAPbI_3$ photodetectors prepared by flash evaporation which exhibited the responsivity of 0.2 A/W and detectivity of $3.82 \cdot 10^{11}$ Jones.

4.1. Introduction

Organo-metal halide perovskites (OHPs) have come into the spotlight as the power conversion efficiency of solar cell using OHPs has increased dramatically in the past few years[1-7]. Since then, OHPs have demonstrated compliant performance in other

optoeletronic devices such as light emitting diodes (LEDs)[8-12], photodetectors[13, 14], lasers[15] and phototransistors[16]. Out of various methods studied in the field, solution-processing[2, 17, 18], thermal evaporation[19, 20] and chemical vapor deposition[21, 22] have gained the most attention as methods for depositing OHP thin films. Especially, spin-coating is the most commonly used lab-scale deposition method because it is a low-cost and easily accessible process. Although some works have reported remarkable device performances in large-area perovskite optoelectronic devices made with spin-coated perovskite films[9, 23], the solution-process fundamentally imposes limitations in reliably producing uniform films over a large area. In addition, the spin-coating methods have evolved to achieve high-quality OHP films for state-of-the-art devices by adopting additional techniques[17] such as hot-casting[2, 5], solvent engineering[24, 25] and two-step sequential deposition[3, 26, 27], which inevitably adds complexities, and therefore reduces the overall controllability of the process.

The evaporation method, on the other hand, has a potential for uniform large-area film deposition[28, 29], conformal film deposition on uneven surfaces[30], as well as a simple patterning with shadow masks[31]. Additionally, since it is a solvent-free process, there is no need to consider surface tension or solubility of the underlying layer. Organo-halide precursor (e.g. methylammonium iodide, MAI) and lead-source precursor (e.g. lead iodide, PbI_2) can be thermally evaporated by co-evaporation method[19, 32], sequential deposition[33-35] or vapour-assisted deposition[36, 37] to form OHP (e.g. methylammonium lead iodide, $MAPbI_3$) films. Although these deposition methods are well-established, it is still challenging to produce OHP films with the desired stoichiometric ratio between the three different ionic components by evaporation because the precursors have very different vaporization temperatures[28].

Flash evaporation method has gained attention as a candidate for evaporating two or more precursors from a single thermal source by rapidly raising the temperature in a very short time[20, 30, 31, 38-41]. In principle, the rapid vaporization of the precursors induces complete and uniform evaporation of the precursors, while maintaining the same ratio between the different components in OHP. Solar cells with flash evaporated OHP films have exhibited over 10% of power conversion efficiency[39, 41], which is comparable to the early stage spin-coated OHP films[17, 42]. Furthermore, the flash evaporation method has been expanded to deposit OHP films with mixed cation and halide species[30], which is challenging for the aforementioned other evaporation methods[28]. Although this aspect of flash evaporation presents a prospect of exploring a diverse compositional range of OHPs, there has been relatively a few reports which have systematically studied the controllability of the flash evaporation method and the uniformity of OHP films produced by this method. Especially, flash evaporated OHP films have only been reported to be uniform in small areas, but wafer-scale uniformity has rarely been investigated to assess its applicability for mass-producing devices with uniform performance. In this paper, I demonstrate that OHP films with wafer-scale uniformity can be formed by flash evaporation. In addition, it is difficult to monitor the deposition rate and control the resulting film thickness with flash evaporation due to the rapid nature of the evaporation process, unlike other methods. For optoelectronic devices, the thickness of the active layer is critical in determining the device performance[43, 44]. Therefore, a reliable deposition of OHP films with controllability over a wide range of target thicknesses is desired for meeting different requirements in terms of film characteristics for various device applications. Our study directly shows that the thickness of flash evaporated OHP films can be controlled by simply adjusting the mass of the source material. Similarly, I discovered

that the grain size of the flash evaporated OHP films varied with the mass of the source materials loaded, and that the grain size could even be controlled by introducing multi-step depositions.

4.2. Results and Discussion

In this study, I focused on the deposition of $MAPbI_3$ films (see Figure 1(a) for the crystal structure) by flash evaporation. Figure 1(b) shows a schematic image of the

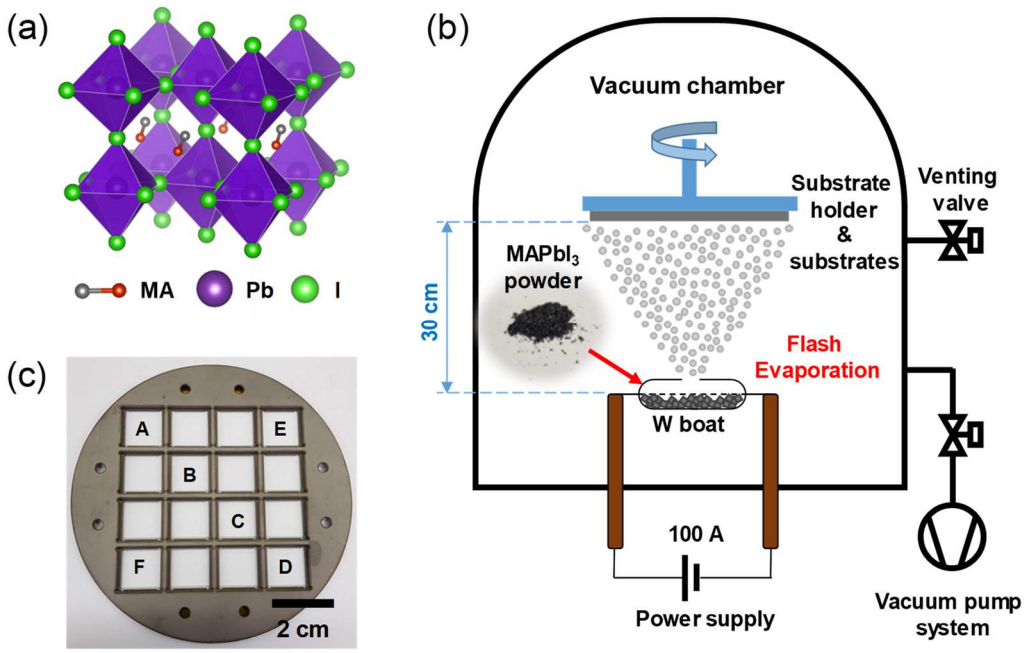

Figure 4.1 (a) Schematic illustration of $MAPbI_3$ crystal structure. (b) Schematic illustration of deposition of organo-halide perovskite film via flash evaporation. The inset shows photographs of $MAPbI_3$ single crystal powder. (c) A photograph of the substrate holder for film uniformity test with the labels that indicate the location of the substrates (from A to F).

flash evaporation process adopted in this work. The pre-synthesized $MAPbI_3$ single crystal powder was used as the source instead of PbI_2 and MAI precursors (see the inset of Figure

4.1(b)) in order to obtain better quality films owing to an exact stoichiometric ratio between the different ionic components of $MAPbI_3$ within the single crystal[30, 45]. The exact amount of single crystal powder was loaded on the tungsten boat which is located inside of vacuum chamber. The source-to-substrate distance was designed to be 30 cm which is the longest distance among source-to-substrate distances of flash evaporation reported so far[20, 31, 38, 40, 41]. This is so that I could achieve a uniform deposition of $MAPbI_3$ over a large area at the substrate end. The $MAPbI_3$ single crystal powder was heated by rapidly ramping up the heater current to 100 A in 3 seconds at a constant voltage of 0.31 V. The powder was then evaporated within 60 seconds and deposited on substrates which were located on specific locations of the holder. Throughout this paper, I will refer to different sample locations in the 4-inch wafer size substrate holder as labeled in Figure 4.1(c) (substrate location A to F) to assess the uniformity of the deposited $MAPbI_3$ film.

I checked the film quality of flash evaporated $MAPbI_3$ films by probing their structural and optical properties as shown in Figures 4.2 and 4.3. An optical micrograph of the flash evaporated $MAPbI_3$ film patterned by a shadow mask showed a smooth and clean film with a clearly distinguishable boundary at the edge (see Figure 4.2(a)). The top-surface images of the films measured by field emission scanning electron microscope (FE-SEM) and atomic force microscope (AFM) are presented in Figures 4.2(b) and 4.2(c), respectively. A typical grain size determined from the FE-SEM image is 40 nm which I will discuss further later in the paper. A smooth and pinhole-free surface was observed with the roughness of approximately 5 nm (2.86 nm locally, Figure 4.2(c)).

Figure 4.3(a) shows the X-ray diffraction (XRD) results. The green line shows the XRD result of the single crystal powders of $MAPbI_3$ used as the source, which closely resembles the calculated XRD results. It signifies that a high purity $MAPbI_3$ single crystal

powders were successfully synthesized. The blue and red lines show the XRD results of the flash evaporated and spin-coated $MAPbI_3$ films, respectively. The positions of the (110) and (220) peaks were the same for all the XRD results (14.1º and 28.5º, respectively), confirming the identical crystal structure of the flash evaporated $MAPbI_3$ film with those prepared by other methods. As no peaks other than (110) and (220) peaks appeared, the deposited $MAPbI_3$ films exhibit a strong preferred orientation along the (110) surface[30, 32, 46, 47]. In addition, the high purity of the flash evaporated film is indicated by the absence of diffraction peaks that correspond to PbI_2 (asterisk marks (12.6º)). Note that this is an interesting observation because many previous studies [31, 38, 40, 41] have demonstrated that the addition of excess MAI was necessary to deposit pure $MAPbI_3$ films without PbI_2 impurities.

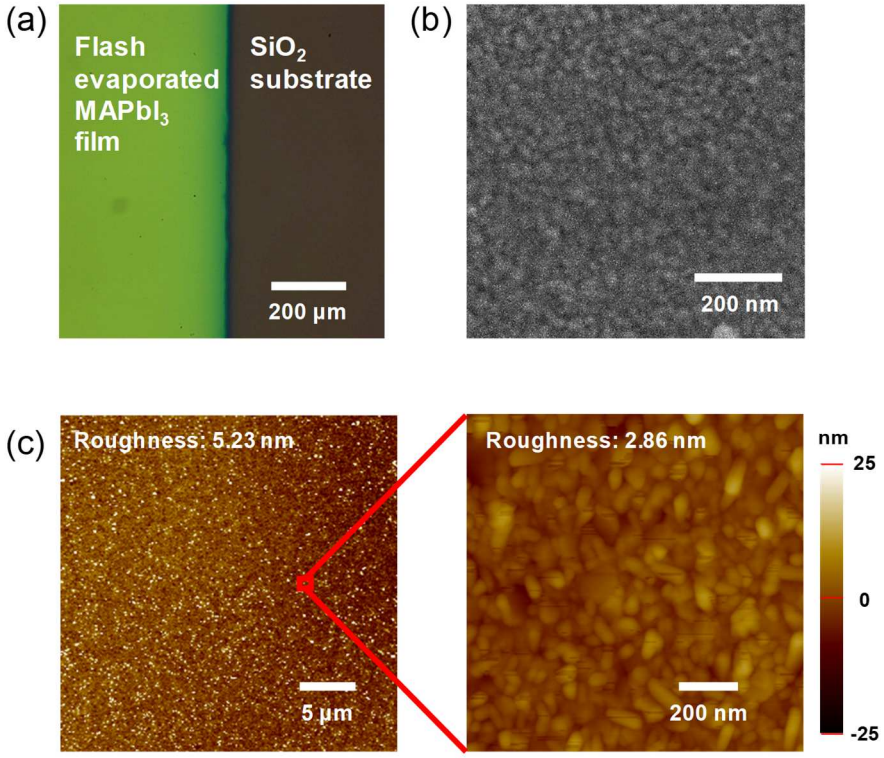

Figure 4.2 (a) An optical microscope image of the flash evaporated $MAPbI_3$ film. (b) SEM image and (c) AFM images of flash evaporated $MAPbI_3$ film surface.

UV-visible absorbance and photoluminescence (PL) spectra were taken to investigate the optical properties of the flash evaporated $MAPbI_3$ film (see Figure 4.3(b)). The estimated optical bandgap from the absorbance spectrum by using the Tauc plot[48] is 1.61 eV (see the inset of Figure 4.3(b)) and PL peak is shown at 756 nm with a full-width-half-maximum (FWHM) of 45 nm, both of which agree well with the reported values for $MAPbI_3$ in literature[15, 49]. When compared with the spin-coated $MAPbI_3$ film produced as a reference sample, it showed similar absorbance and PL spectra. From the structural and optical characterizations, I could safely confirm that our flash evaporated $MAPbI_3$ films had a high film quality without a significant amount of impurities formed.

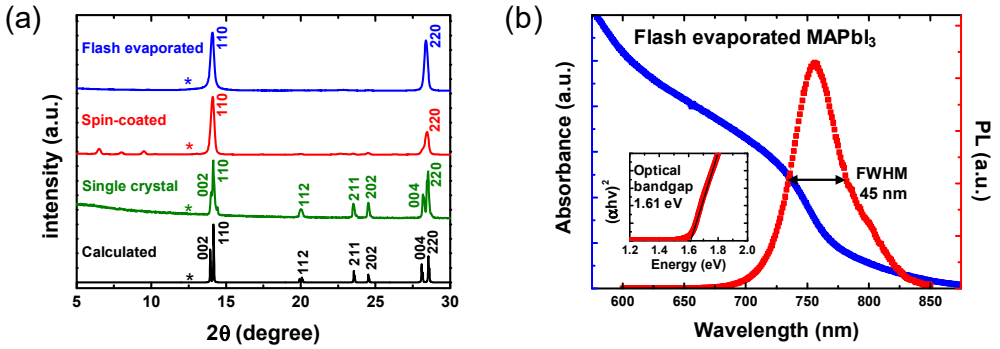

Figure 4.3 (a) XRD data of the flash evaporated film, spin-coated film and single crystal powder. Calculated results from the unit cell of $MAPbI_3$ are also shown. (b) UV-visible absorbance and PL spectra of $MAPbI_3$ film deposited via flash evaporation. The inset shows Tauc plot to estimate the optical bandgap of the perovskite film.

I checked that the evaporated perovskite films had a uniform thickness and the same optical properties over the whole wafer. Before testing wafer-scale film uniformity, I compared the film uniformity between the flash evaporated perovskite film to spin-coated perovskite film (reference) on the 1.5 × 1.5 cm^2 substrate. The thickness values of both films were measured by randomly selecting 20 points on cross-sectional FE-SEM images.

The average thickness values of the flash evaporated and spin-coated films were similar (207.1 nm and 225.0 nm, respectively), while the standard deviation for the spin-coated film was about 10 times larger (30.2 nm compared to 3.0 nm for the flash evaporated film). Given that the standard deviation value of 3.0 nm for the flash evaporated film is similar to the surface roughness value measured by AFM, the variation in the sampled thickness values can be assumed to be due to the morphology, not the variation in the actual thickness within the film. It can be seen that the film made by flash evaporation has a much uniform thickness and a smooth surface.

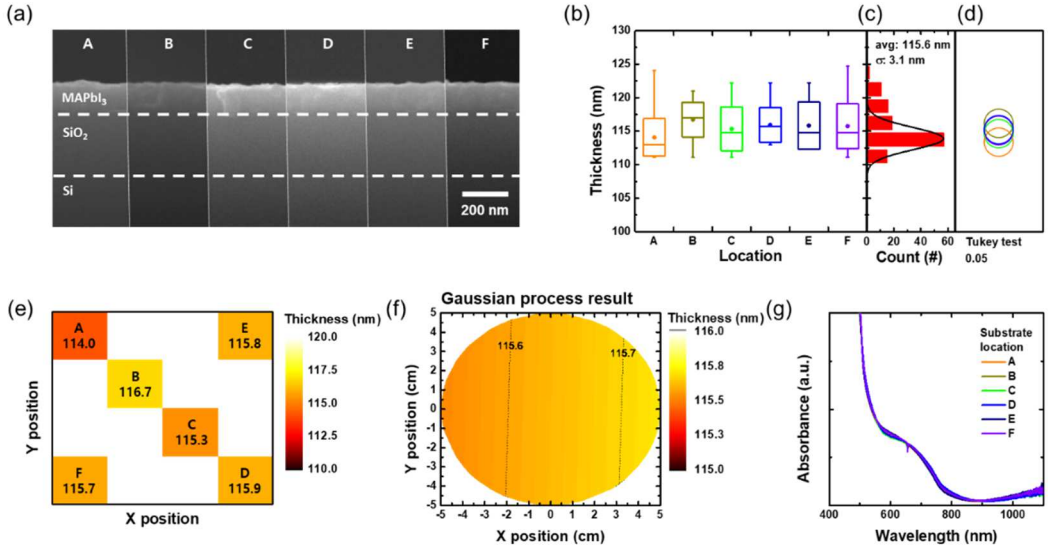

Figure 4.4 Uniformity test of flash evaporated $MAPbI_3$ films. (a) Cross-sectional SEM images for the thickness comparison of the $MAPbI_3$ film by the substrate location given in Figure 1(c). (b) The measured thickness values presented in box and whisker diagram at each location. (c) A histogram of all the thickness data. (d) Comparison circles from the Tukey test. (e) Color map image of the average thickness values at each substrate location on the 4-inch wafer. (f) The estimated thickness of the perovskite film by Gaussian process. (g) UV-visible absorbance spectra of the $MAPbI_3$ films at the different substrate locations.

In order to investigate whether there was a change in the thickness depending on

the location over the 4-inch wafer, cross-sectional FE-SEM images were taken for the evaporated films at each substrate location labeled according to Figure 4.1(c) (Figure 4.4(a)). The thickness values were measured at 20 points of the film for each substrate in order to carry out statistical analysis. Figure 4.4(b) is a graph summarizing the thickness values extracted from each substrate location drawn as a box and whisker diagram. The dots within the boxes represent the average values and boxes show the first and third quartile range of each distribution. The lines inside the box represent median values and the whiskers show the minimum and maximum values. The box and whisker diagrams show the similarity in the distribution of the thickness values at different locations. Figure 4.4(c) shows the distribution for all the measured 120 thickness values from the different locations shown in Figure 4.4(b) plotted together in one histogram. The thickness values did not significantly deviate from the average value of 115.6 nm (the standard deviation was 3.1 nm) at all substrate locations. More importantly, there were no multiple peaks in the normal distribution fit, which suggests that all the thickness values belong to a single distribution. Tukey-Kramer honest significant difference test (Tukey test)[50] was performed to quantitatively determine whether the distributions of the thickness values at the six different substrate locations (shown in Figure 4.4(b)) can be judged as the same distribution. Tukey test is a statistical test that compares multiple distributions simultaneously and shows how different they are from each other, which can be used to categorize similar distributions into separate groups. Figure 4.4(d) is a graphical visualization of the Tukey test results. The comparison circles are shown in Figure 4.4(d) have their centers each aligned with the average thickness values and the radii proportional to the standard deviation values of each distribution. The more the comparison circles overlap, the more similar the distributions are. Here, the comparison circles are all

overlapped and therefore all the distributions can be judged as the same distribution sampled from the same population. Analysis of variance (ANOVA) test[51] was also run to support whether the average values of two or more distributions are statistically identical. Thus, all the average thickness values at each substrate location can be considered statistically identical. To visualize the uniformity in the film thickness over the whole 4-inch wafer, I used a color map to plot the average values of the film thickness at each substrate location from A to F (Figure 4.4(e)). The average thickness values at each substrate location differed by less than 2 nm which is smaller than the standard deviation value of 3.1 nm (Figure 4.4(c)). Figure 4.4(f) shows simulation results obtained by the Gaussian process regression with the whole 120 thickness data. The variation of the predicted thickness across the wafer was as small as approximately 2 Å. In addition to the thickness measurement, UV-visible absorbance and PL spectra were measured for the films deposited at each substrate location to confirm that they all have the same absorbance and PL responses regardless of location (see Figure 4.4(g)). All these results consistently support the wafer-scale uniformity of the flash evaporated perovskite film over the 4-inch wafer.

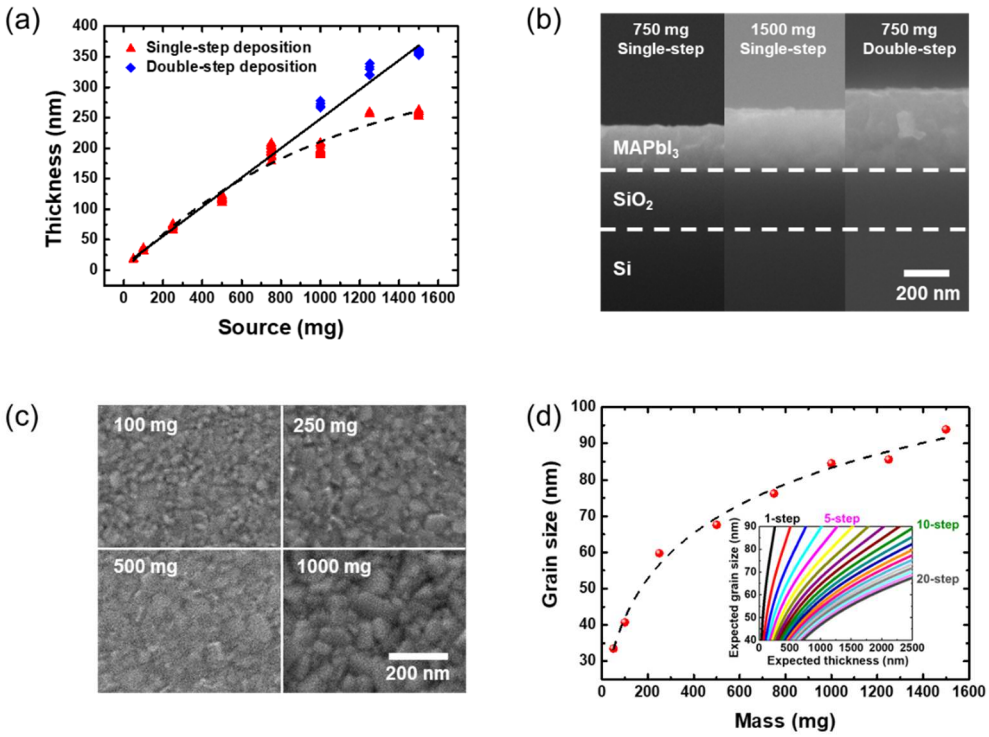

Figure 4.5 (a) A graph of thickness of the flash evaporated perovskite film as a function of the amount of the $MAPbI_3$ single crystal power source. (b) Cross-sectional SEM images for a single- and multi-step deposited perovskite films by flash evaporation for comparison. (c) Top-view SEM images for showing grain size variation for deposition with different source mass. (d) Grain size correlation graph of the deposited perovskite films according to the source mass. The inset shows a predicted controllable range of the grain size and thickness of the $MAPbI_3$ films by the empirical fit shown as the dashed line.

The controllability of the flash evaporation method was demonstrated by depositing various thicknesses of perovskite films by varying the weight of the source materials. The thicknesses of the films were measured by using a cross-sectional FE-SEM as in the uniformity measurement. The thickness increased linearly with increasing the weight of the source from 50 mg to 750 mg (see the red triangle points in Figure 4.5(a)). However, as the weight of the source exceeded 750 mg, the increase in the thickness

became sub-linear. In order to mitigate the non-linear relationship above the threshold weight of the source of 750 mg, I introduced a multi-step deposition (i.e. the perovskite films were successively deposited multiple times). For example, to deposit a target thickness of 250 nm, 500 mg of the source perovskite powders were deposited twice (a total of 1000 mg), which could then be described by a linear relationship again (see the blue diamond points in Figure 4.5(a)). Figure 4.5(b) shows the representative cross-sectional SEM images of $MAPbI_3$ films deposited with different weights of the source. Flash evaporation with 1500 mg of the source powders does not yield twice the thickness of the $MAPbI_3$ film with 750 mg of the source powders. However, successively evaporating 750 mg of the source twice gives a $MAPbI_3$ film twice the thickness (See Figure4. 5(b)).

I discovered that the grain size could also be controlled by varying the weight of the source powders. The grain size tended to increase as the source mass increased (Figures 4.5(c) and 4.5(d)). I also discovered that the grain size did not vary significantly depending on the number of deposition steps while the thickness increased linearly for a double-step (390 nm) and triple-step (620 nm) evaporated films for the source mass of 750 mg, which potentially provides a way for controlling the grain size independently with the thickness (see the inset of Figure 4.4(d) for the predicted range of grain size for each thickness). The grain size of crystals in perovskite films, along with its thickness, is an important parameter that determines the device performance of optoelectronic devices. In the case of solar cells, the carriers should be able to move freely from the active layer (the point of generation within) to the electrodes (where they are extracted), so the larger the grain, the better the collection efficiency[40]. In the case of LEDs, a higher rate of recombination is desired, and therefore a smaller grain size would be required to fabricate LEDs with higher emission efficiencies[52]. Therefore, our findings can be highly relevant for investigating the

relationship between the grain size and device performance of optoelectronic devices based on flash evaporated perovskite films.

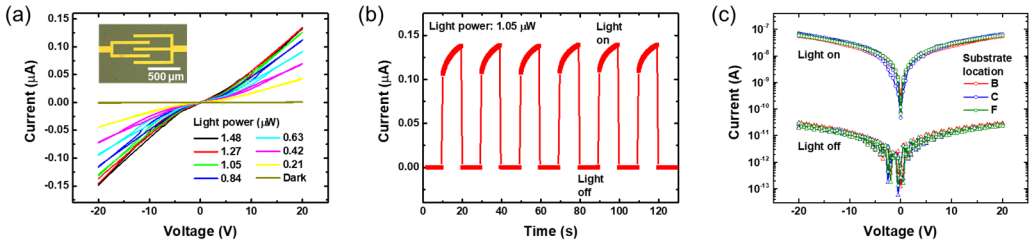

Figure 4.6. Device characteristics of photodetectors prepared by flash evaporation. (a) I-V characteristics under 520 nm laser with different intensities. The inset shows the optical microscope image of the fabricated $MAPbI_3$ photodetector. (b) Time-dependent photoresponse of the photodetector under few cycles of turn-on and off. (c) The I-V characteristics under light and dark conditions for the photodetectors prepared by the flash evaporated films at the different substrate locations.

In order to demonstrate how the wafer-scale film uniformity discussed so far can be transferred to the uniformity in the optoelectronic device performance, I fabricated photodetectors which are one of the most suitable devices due to their simple structures that require only the deposition of two top contact electrodes on evaporated perovskite films (see the inset of Figure 4.6(a) for the device structure). For performance comparison, a photodetector using spin-coated $MAPbI_3$ film was also fabricated. The detailed fabrication process is explained in the Methods section. Figure 4.6(a) shows typical current-voltage curves of the photodetector with the evaporated film under light illumination with 532 nm wavelength and various laser intensities. The photocurrent gradually increased with increasing the laser intensity due to increased photogenerated carrier concentrations. The responsivity (R) which is the ratio of the excess current generated by light illumination to

the incident light power was studied. The responsivity decreased as the light power increased. This can be attributed to the increase of carrier-carrier scattering or filling the deep trap states with a longer lifetime, which tends to provide a higher photocurrent at a lower light power[53-55]. The estimated responsivity is 0.20 A/W for the photodetector with the flash evaporated film and 0.55 A/W for the photodetector with the spin-coated film at a bias of 20 V and light power of 0.21 uW. Detectivity (D*) which is another parameter to characterize the sensitivity of photodetection was calculated according to $D^* = R\left(\frac{2eI_{dark}}{A}\right)^{-\frac{1}{2}}$, where I_{dark} is the dark current, A is the area of the photosensitive region and e is the electric charge. The highest value of detectivity was found to be 3.82×10^{11} Jones within the measured range for the photodetector with the flash evaporated film. This is a comparable value to the detectivity of 6.14×10^{11} Jones for the device with the spin-coated film. These device performance parameters are comparable to the previously reported $MAPbI_3$-based photodetectors[31, 56-58] and commercial Si photodetectors (< 0.2 A/W)[47, 59]. Figure 4.6(b) displays repeated on/off operation of the photodetector with the flash evaporated $MAPbI_3$ film. The device showed relatively fast photo-responses (< 1 s), stable and reproducible operation during the measurement cycles. Finally, in order to demonstrate how the wafer-scale film uniformity discussed above can be transferred to the uniformity in the photodetector device performance, I fabricated photodetectors with flash evaporated films at different locations (see Figure 4.6(c)). The measured device characteristics were nearly identical regardless of the sample substrate locations (B, C, and F), which shows that I can achieve the wafer-scale uniformity in the device performance by our flash evaporation method.

4.3. Experiments

Synthesis of $MAPbI_3$. 2.66 g of PbO and 1.90 g of CH_3NH_3I (MAI) were dispersed in a mixed acid solution of HI (18 ml, 57 wt% in water) and H_3PO_2 (2 ml, 50 wt% in water). The solution was heated at 130 °C until all the precursors were dissolved. The solution was then cooled to room temperature to precipitate $MAPbI_3$ single crystals. The crystals were isolated by filtration and dried in vacuum conditions.

Film preparation.

Substrate cleaning. The thermally grown 270 nm thick SiO_2 on Si substrate and glass were sequentially cleaned with acetone, 2-propanol, and deionized water in a sonicator for 10 min at each step. SiO_2 and glass substrates were exposed to 50 W, 30 sccm condition of O_2 plasma for 120 seconds.

Deposition of $MAPbI_3$ film by flash evaporation. Prepared $MAPbI_3$ powder was placed into a tungsten boat. After the pressure in a chamber pumped down to below $1 \cdot 10^{-6}$ Torr, the substrate holder was rotated in 24 rpm for film uniformity, and the current of tungsten boat was rapidly increased to 100 A in 3 seconds. Then, the temperature of the tungsten boat was raised rapidly and $MAPbI_3$ powder sublimated. The nominal deposition rate read by the sensor was approximately 50−80 Å/sec. When the deposition rate decreased to 0.1 Å/sec, the process was terminated and the total deposition time was within 60 seconds.

Deposition of $MAPbI_3$ film by spin-coating. Spin-coating was conducted according to the known hot-casting method[2]. 0.5 M of perovskite precursor solution was prepared by dissolving the prepared $MAPbI_3$ powder in DMF. The cleaned substrate was heated at 120 °C on the hot plate. Then, the heated substrate was quickly moved to the spin-coater and the precursor solution was spin-coated on the substrate for 40 seconds at 5000 rpm.

Fabrication of photodetector. The Au top electrode lines with 50 μm width and 50 nm

thickness were deposited using a patterned shadow mask on prepared perovskite film. The electron-beam evaporator pressure was $1 \cdot 10^{-6}$ Torr and the value of the Au deposition rate on the sensor was approximately 1 Å/sec.

Film Characterization.

SEM measurements. The thickness and surface morphology of the perovskite film were analyzed by FE-SEM (JSM-7800F Prime) using an electron beam accelerated at 5 kV for surface morphology study and 10 kV for thickness study.

XRD measurements. Crystallographic structures of perovskite films were analyzed by high resolution X-ray diffraction (HRXRD) technique (Rigaku Smartlab).

Steady-state PL measurements. Steady-state PL spectra of the thin film samples (glass/$MAPbI_3$ film) were measured using a spectrofluorometer (JASCO FP-8500). The excitation wavelength was 520 nm and used Xenon arc lamp (150 W).

Absorbance measurements. The absorbance of the thin film samples (glass/$MAPbI_3$ film) was measured using a UV/Vis spectrophotometer (PerkinElmer LAMBDA 45).

4.4. Conclusions

I designed a single-source flash evaporation setup with a long source-to-substrate distance to deposit $MAPbI_3$ films directly over 4-inch wafer. The thicknesses of the films were measured at various locations of the 4-inch wafer and statistically analyzed to demonstrate that the thicknesses of the films were constant throughout the whole 4-inch wafer. The optical properties of the flash evaporated films were also identical throughout the wafer. The correlation between the amount of the single crystal perovskite powders loaded to the source and the thickness of the deposited film was studied to demonstrate the controllability of the evaporation. I observed that the deposited $MAPbI_3$ film thickness was proportional

to the source mass until a critical point, above which the film thickness started to saturate. The proportionality was recovered by introducing the multiple numbers of deposition steps which additionally provided a way for controlling the grain size by varying the source mass and number of deposition steps. The wafer-scale uniformity was preserved for photodetector devices fabricated with flash evaporated $MAPbI_3$ films. The fabricated devices showed the responsivity of 0.2 A/W and detectivity of 3.82×10^{11} Jones which are comparable to the previously reported $MAPbI_3$-based photodetectors. Our results demonstrate that single-source flash evaporation can be a promising route towards controllably and reliably depositing large-area perovskite films, and therefore producing perovskite-based optoelectronic devices in large-scale.

References

[1] Zhou H, Chen Q, Li G, Luo S, Song T-b, Duan H-S, Hong Z, You J, Liu Y and Yang Y 2014 *Science* **345** 542-6

[2] Nie W, Tsai H, Asadpour R, Blancon J-C, Neukirch A J, Gupta G, Crochet J J, Chhowalla M, Tretiak S, Alam M A, Wang H-L and Mohite A D 2015 *Science* **347** 522-5

[3] Yang W S, Noh J H, Jeon N J, Kim Y C, Ryu S, Seo J and Seok S I 2015 *Science* **348** 1234-7

[4] Choi H, Mai C-K, Kim H-B, Jeong J, Song S, Bazan G C, Kim J Y and Heeger A J 2015 *Nat. Commun.* **6** 7348

[5] Tsai H, Nie W, Blancon J-C, Stoumpos C C, Asadpour R, Harutyunyan B, Neukirch A J, Verduzco R, Crochet J J, Tretiak S, Pedesseau L, Even J, Alam M A, Gupta G, Lou J, Ajayan P M, Bedzyk M J, Kanatzidis M G and Mohite A D 2016 *Nature* **536** 312-6

[6] Park N-G 2018 *MRS Bull.* **43** 527-33

[7] 2020 NREL. Efficiency chart.

[8] Tan Z-K, Moghaddam R S, Lai M L, Docampo P, Higler R, Deschler F, Price M, Sadhanala A, Pazos L M, Credgington D, Hanusch F, Bein T, Snaith H J and Friend R H 2014 *Nat. Nanotechnol.* **9** 687-92

[9] Zhao X and Tan Z-K 2020 *Nat. Photonics* **14** 215-8

[10] Lee H-D, Kim H, Cho H, Cha W, Hong Y, Kim Y-H, Sadhanala A, Venugopalan V, Kim J S, Choi J W, Lee C-L, Kim D, Yang H, Friend R H and Lee T-W 2019 *Adv. Funct. Mater.* **29** 1901225

[11] Cho H, Jeong S-H, Park M-H, Kim Y-H, Wolf C, Lee C-L, Heo J H, Sadhanala A, Myoung N, Yoo S, Im S H, Friend R H and Lee T-W 2015 *Science* **350** 1222-5

[12] Cao Y, Wang N, Tian H, Guo J, Wei Y, Chen H, Miao Y, Zou W, Pan K, He Y, Cao H, Ke Y, Xu M, Wang Y, Yang M, Du K, Fu Z, Kong D, Dai D, Jin Y, Li G, Li H, Peng Q, Wang J and Huang W 2018 *Nature* **562** 249-53

[13] Fang Y, Dong Q, Shao Y, Yuan Y and Huang J 2015 *Nat. Photonics* **9** 679

[14] Blancon J C, Tsai H, Nie W, Stoumpos C C, Pedesseau L, Katan C, Kepenekian M, Soe C M M, Appavoo K, Sfeir M Y, Tretiak S, Ajayan P M, Kanatzidis M G, Even J, Crochet J J and Mohite A D 2017 *Science* **355** 1288-92

[15] Xing G, Mathews N, Lim S S, Yantara N, Liu X, Sabba D, Grätzel M, Mhaisalkar S and Sum T C 2014 *Nat. Mater.* **13** 476-80

[16] Qian L, Sun Y, Wu M, Xie D, Ding L and Shi G 2017 *Adv. Mater.* **29** 1606175

[17] Park N-G 2015 *Mater. Today* **18** 65-72

[18] Yu W, Li F, Yu L, Niazi M R, Zou Y, Corzo D, Basu A, Ma C, Dey S, Tietze M L, Buttner U, Wang X, Wang Z, Hedhili M N, Guo C, Wu T and Amassian A 2018 *Nat. Commun.* **9** 5354

[19] Momblona C, Gil-Escrig L, Bandiello E, Hutter E M, Sessolo M, Lederer K, Blochwitz-Nimoth J and Bolink H J 2016 *Energy Environ. Sci.* **9** 3456-63

[20] Mitzi D B, Prikas M T and Chondroudis K 1999 *Chem. Mater.* **11** 542-4

[21] Niu L, Liu X, Cong C, Wu C, Wu D, Chang T R, Wang H, Zeng Q, Zhou J, Wang X, Fu W, Yu P, Fu Q, Najmaei S, Zhang Z, Yakobson B I, Tay B K, Zhou W, Jeng H T, Lin H, Sum T C, Jin C, He H, Yu T and Liu Z 2015 *Adv. Mater.* **27** 7800-8

[22] Lan C, Dong R, Zhou Z, Shu L, Li D, Yip S and Ho J C 2017 *Adv. Mater.* **29** 1702759

[23] Chen Y, Zhang L, Zhang Y, Gao H and Yan H 2018 *RSC Adv.* **8** 10489-508

[24] Jeon N J, Noh J H, Kim Y C, Yang W S, Ryu S and Seok S I 2014 *Nat. Mater.* **13** 897-903

[25] Wu T, Wu J, Tu Y, He X, Lan Z, Huang M and Lin J 2017 *J. Power Sources* **365** 1-6

[26] Burschka J, Pellet N, Moon S-J, Humphry-Baker R, Gao P, Nazeeruddin M K and Grätzel M 2013 *Nature* **499** 316-9

[27] Im J-H, Jang I-H, Pellet N, Grätzel M and Park N-G 2014 *Nat. Nanotechnol.* **9** 927-32

[28] Ávila J, Momblona C, Boix P P, Sessolo M and Bolink H J 2017 *Joule* **1** 431-42

[29] Li G, Ho J Y L, Wong M and Kwok H-S 2016 *physica status solidi (RRL) – Rapid Research Letters* **10** 153-7

[30] Crane M J, Kroupa D M, Roh J Y, Anderson R T, Smith M D and Gamelin D R 2019 *ACS Applied Energy Materials* **2** 4560-5

[31] Wei H, Ma H, Tai M, Wei Y, Li D, Zhao X, Lin H, Fan S and Jiang K 2017 *RSC Adv.* **7** 34795-800

[32] Liu M, Johnston M B and Snaith H J 2013 *Nature* **501** 395-8

[33] Yang D, Yang Z, Qin W, Zhang Y, Liu S and Li C 2015 *J. Mater. Chem. A* **3** 9401-5

[34] Chen C-W, Kang H-W, Hsiao S-Y, Yang P-F, Chiang K-M and Lin H-W 2014 *Adv. Mater.* **26** 6647-52

[35] Bohee H and Jang-Sik L 2017 *Adv. Mater.* **29** 1701048

[36] Ono L K, Wang S, Kato Y, Raga S R and Qi Y 2014 *Energy Environ. Sci.* **7** 3989-93

[37] Hwang B and Lee J-S 2018 *Adv. Opt. Mater.* **7** 1801356

[38] Tai M, Zhao X, Wei H, Wang G, Hao F, Li X, Yin X, Zhou Y, Han J, Wei Y, Jiang K and Lin H 2018 *ACS Appl. Mater. Interfaces* **10** 26206-12

[39] Wei H, Zhao X, Wei Y, Ma H, Li D, Chen G, Lin H, Fan S and Jiang K 2017 *NPG Asia Mater.* **9** e395-e

[40] Xu H, Wu Y, Xu F, Zhu J, Ni C, Wang W, Hong F, Xu R, Xu F, Huang J and Wang L 2016 *RSC Adv.* **6** 48851-7

[41] Longo G, Gil-Escrig L, Degen M J, Sessolo M and Bolink H J 2015 *Chem. Commun.* **51** 7376-8

[42] Kim H-S, Lee C-R, Im J-H, Lee K-B, Moehl T, Marchioro A, Moon S-J, Humphry-Baker R, Yum J-H, Moser J E, Grätzel M and Park N-G 2012 *Sci. Rep.* **2** 591

[43] Momblona C, Malinkiewicz O, Roldán-Carmona C, Soriano A, Gil-Escrig L, Bandiello E, Scheepers M, Edri E and Bolink H J 2014 *APL Mater.* **2** 081504

[44] Zhao L, Lee K M, Roh K, Khan S U Z and Rand B P 2019 *Adv. Mater.* **31** 1805836

[45] Huang C-Y, Wu C-C, Wu C-L and Lin C-W 2019 *ACS Omega* **4** 8081-6

[46] Climent-Pascual E, Hames B C, Moreno-Ramírez J S, Álvarez A L, Juarez-Perez E J, Mas-Marza E, Mora-Seró I, de Andrés A and Coya C 2016 *J. Mater. Chem. A* **4** 18153-63

[47] Wang K, Wu C, Yang D, Jiang Y and Priya S 2018 *ACS Nano* **12** 4919-29

[48] Saidaminov M I, Abdelhady A L, Murali B, Alarousu E, Burlakov V M, Peng W, Dursun I, Wang L, He Y, Maculan G, Goriely A, Wu T, Mohammed O F and Bakr O M 2015 *Nat. Commun.* **6** 7586

[49] Kong W, Ye Z, Qi Z, Zhang B, Wang M, Rahimi-Iman A and Wu H 2015 *Phys. Chem. Chem. Phys.* **17** 16405-11

[50] Tukey J W 1977 *Exploratory data analysis* vol 2: Reading, Mass.)

[51] Scheffe H 1999 *The analysis of variance* vol 72: John Wiley & Sons)

[52] Yuan M, Quan L N, Comin R, Walters G, Sabatini R, Voznyy O, Hoogland S, Zhao Y, Beauregard E M, Kanjanaboos P, Lu Z, Kim D H and Sargent E H 2016 *Nat. Nanotechnol.* **11** 872-7

[53] Zhang W, Huang J-K, Chen C-H, Chang Y-H, Cheng Y-J and Li L-J 2013 *Adv. Mater.* **25** 3456-61

[54] Konstantatos G, Howard I, Fischer A, Hoogland S, Clifford J, Klem E, Levina L and Sargent E H 2006 *Nature* **442** 180-3

[55] Konstantatos G, Clifford J, Levina L and Sargent E H 2007 *Nat. Photonics* **1** 531-4

[56] Bao C, Zhu W, Yang J, Li F, Gu S, Wang Y, Yu T, Zhu J, Zhou Y and Zou Z 2016 *ACS Appl. Mater. Interfaces* **8** 23868-75

[57] Gegevičius R, Treideris M, Pakštas V, Franckevičius M and Gulbinas V 2018 *Adv. Electron. Mater.* **4** 1800114

[58] Bai F, Qi J, Li F, Fang Y, Han W, Wu H and Zhang Y 2018 *Adv. Mater. Interfaces* **5** 1701275

[59] Guo F, Yang B, Yuan Y, Xiao Z, Dong Q, Bi Y and Huang J 2012 *Nat. Nanotechnol.* **7** 798-802

Chapter 5. Tailored Design-of-Experiments Approach for Optimization of Flash-Evaporated Organic Inorganic Halide Perovskite-based

In this thesis, I described optimization method to deposit perovskite films which can be used for flexible resistive memory devices. Single-source flash evaporation method has recently gained attention for its potential as a rapid and solvent-free deposition method for producing organic-inorganic halide perovskite (OHP) films in large-scale. However, due to a complex nature of the different experimental parameters involved in the deposition process, it is not straightforward to obtain the optimal condition for producing high-quality OHP films. In this study, I tackle this problem by employing the design-of-experiment (DoE) process, which is an efficient statistical analysis for finding an optimized condition with a minimized number of experiments. The DoE process was used for optimizing the responsivity of the OHP photodetector devices against the input variables used in the deposition that yielded an enhanced responsivity of 112.2 mA/W, which is up to an order of magnitude higher than that of the unoptimized devices. Our experimental results using the DoE method provide not only the conditions required for enhancing the device performance but also the guidelines for improving the overall film quality through exploring the variable space of the flash evaporation technique.

5.1. Introduction

Organic-inorganic halide perovskites (OHPs) have recently received enormous attention due to their excellent properties for optoelectronic[1-17] and electronic[18-21] devices. Out of various deposition methods studied in the field, solution-processing[7, 22, 23], chemical vapor deposition (CVD)[24, 25] and thermal evaporation[26, 27] have gained the most attention for OHPs. Spin-coating techniques of OHPs are mainly used in lab-scale device fabrication because it is a low-cost and easily accessible process. Although

some works have reported remarkable device performances in large-area perovskite optoelectronic devices made with spin-coated perovskite films,[12, 28] the spin-coating techniques face a challenge in producing reliable and uniform films over a large area. On the other hand, evaporation methods have shown a potential for producing uniform films over a large area.[29, 30] The evaporation methods do not require the use of solvents and thus have the advantage that the films can be deposited without solvent-induced-damages which are critical for organo-metal-halide perovskite films.[31, 32] Organo-halide precursor (e.g. methylammonium iodide, MAI) and lead-source precursor (e.g. lead iodide, PbI_2) can be thermally evaporated by various methods, i.e., co-evaporation method,[26, 33, 34] vapor-assisted deposition[1, 35] or sequential deposition[36-38] to fabricate OHP (e.g. methylammonium lead iodide, $MAPbI_3$) films. Although these deposition methods are well-established, it is crucial to produce OHP films with the desired stoichiometric ratio among the three different ionic components by evaporation because each precursor has different sublimation temperatures.[30]

The single-source flash evaporation method[27, 32, 39-41] has gained attention as a candidate for thermally evaporating from either a mixed-precursor source or pre-synthesized stoichiometric OHP source by expeditiously raising the temperature in a short time. In principle, the rapid vaporization of the single crystal precursors results in a uniform and homogeneous evaporation of the precursors while maintaining the same ratio between the different components in OHP.[32] Furthermore, the single-source flash evaporation method can be expanded to fabricate OHP films with mixed cation and halide species, which is challenging in other methods.[30] Although these aspects of the single-source flash evaporation present potential of exploring a diverse compositional range of OHPs, there has been relatively few reports which have systematically studied the film quality

optimization by considering the relationship between relevant input and response variables of the flash evaporation method.

The one-factor-at-a-time (OFAT) method, which is commonly used as a systematic experimental method, has clear disadvantages that it is relatively time-consuming and does not consider interaction effects because only one input variable is considered at a time. Moreover, most of the experimental designs typically require a long time to gather a sufficiently large training data set. Even after the model is completed, precise data predictions are limited to the variables within the range of the training data set. In this way, the effects of single input variables, e.g., substrate temperature,[42] excess amount of MAI, and chamber pressure[41] on the resulting film quality of the evaporated OHP films have been previously studied by following the OFAT method. However, multi-variable interactions and correlations between the input and response variables for achieving desired film properties have not yet been investigated, to the best of our knowledge.

On the contrary, the design-of-experiment (DOE) approach[43, 44] is a multivariate statistical method that is optimized for minimal experimentation. In addition, the DOE method allows us to consider the correlation between the variables in the analysis step and discover optimal experimental conditions via regression analysis. Because the DOE approach considers various variables simultaneously, it is an efficient tool for achieving experimental targets in a relatively short period of time, given that a clear objective is set. Although the DOE approach remains as a powerful tool for performing multivariate statistical analysis, it has been rarely used for investigating the film deposition conditions of organo-metal-halide perovskites.[45]

In our study, the DOE approach was used to analyze the relationship between the variables that affect the film deposition in the flash evaporation method, which in turn,

provided guidelines for optimizing the deposition conditions that produce high-quality perovskite films with the desired optoelectronic properties. Our developed flash evaporation method was recently shown to be highly reproducible and only had few control variables, both of which are suitable for employing the DOE approach for optimizing the film quality. In the analysis process, I first investigated the input variables that affect the physical and optoelectronic properties of the deposited perovskite films and extracted the relationships between these properties. By extending the film characterizations to photodetector devices, the DOE method was able to predict the responsivity values, which allowed us to design devices with a high responsivity value that was up to an order of magnitude higher than that of the devices fabricated from off-optimum conditions.

5.2. Result and Discussion

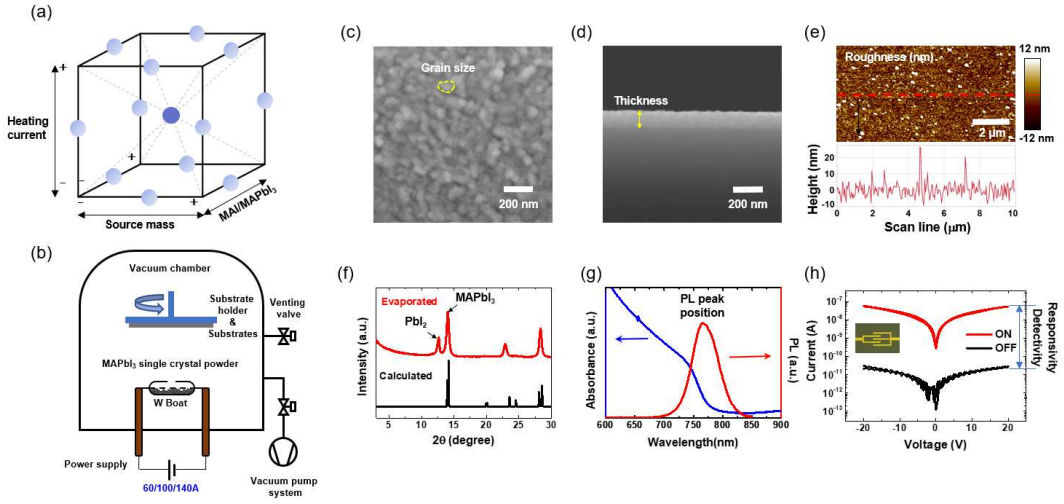

Figure 5.1. (a) A graphical representation of the Box-Behnken design for three factors (heating current, source mass, and excess MAI ratio). (b) A schematic illustration of single-source flash evaporation to deposit a $MAPbI_3$ film. (c) surface and (d) cross-sectional SEM images, and (e) an AFM image of the flash-evaporated $MAPbI_3$ film. (f) X-ray diffraction pattern of the flash-evaporated

$MAPbI_3$ film (red) and calculated data (black) from the unit cell of $MAPbI_3$. (g) UV-visible absorbance spectra (blue) and PL spectra (red) of the $MAPbI_3$ film (h) I-V characteristics of flash-evaporated perovskite photodetectors under white light illumination (red) and dark (black) conditions, which were used to extract responsivity (R) and specific detectivity (D^*).

The overall stages of DOE method can be best described as sequential procedures that consist of 1) planning the experiments, 2) executing the experiments, 3) analyzing the results, and 4) optimizing via data analysis. In the stage of planning the experiments, input variables, response variables and experimental design are chosen according to the set objective. In this study, I employed response surface method (RSM) out of various experimental which is suited for optimizing deposition conditions for producing high-quality flash-evaporated $MAPbI_3$ films.[46, 47] Among the RSM designs, the Box-Behnken design was chosen because it is an efficient design that needs relatively few numbers of experiments for optimization. It acquires data that correspond to experiments at the center of each side of the cubic variable space[48] (see Figure 5.1(a)). The length of each side of the cube represents a range of input variables and each point at the center (represented as circles in Figure 5.1(a)) corresponds to a set of input variables (i.e. an experimental condition) used for each experiment. In the Box-Behnken design, when three input variables are selected, 13 different experimental conditions are determined, and the center point experiment condition (dark blue circle in Figure 5.1(a)) is repeatedly evaluated three times to verify reproducibility and robustness of the model. By using such an experimental model, the experiments are arranged regularly such that potential bias towards specific experimental conditions is avoided. Therefore, it is a convenient model to analyze

the effect of individual input variables on each response variable, as well as the interactions between them.

The objective of the DOE process was to find the optimal deposition condition for single-source flash evaporation of $MAPbI_3$ film (from the set-up schematically drawn in Figure 5.1(b)) that results in high-performance photodetectors. In total, three input variables were selected based on the previous studies on flash evaporation of OHP films. An excess amount of MAI added to the source (i.e. an excess molar ratio of MAI to $MAPbI_3$ powder) was selected as the first variable because it has been reported to play a role in reducing PbI_2 impurity in the evaporated film which is related to the relative purity of the evaporated film.[41] The other input variables were the mass of $MAPbI_3$ single crystal source (source mass, the second variable) and the heating current (related to the heating temperature, the third variable) which control the total amount of evaporated materials and sublimation rate, both of which affect the thickness and grain size of the deposited $MAPbI_3$ films. By combining these three input variables that control the relative purity, grain size, and thickness of the $MAPbI_3$ films, I attempted to find out the relationships between physical properties, optoelectronic properties, and the resulting device performance of photodetectors made with the flash-evaporated $MAPbI_3$ films.

In the DOE process, the selection of the evaluation scope, which is expressed as the size of the variable cube shown in Figure 5.1(a), is important because I can extract the effect of multi-input-variables on each response variable, and thus find out optimum experimental condition within the evaluated range of the variables. The range of the input variables should be selected such that it is neither too wide to prevent an accurate linear regression analysis nor too narrow to risk the loss of generality of the extracted model. As a 1:1 molar ratio between MAI and $MAPbI_3$ was found to be ideal for reducing PbI_2

impurity in a previous study,[41] the evaluation range was selected from 0.5 to 1.5 mol ratio. In order to control the range of thickness from 500 to 2000 Å, the source mass (the second variable) was evaluated in the range from 250 to 750 mg. For the heating current (the third variable), 60 A represented a slow sublimation of the source, nearly approaching the rate of conventional thermal evaporation. Therefore, the heating current was evaluated in the range between 60 A and 140 A. In order to find out the effect of the aforementioned input variables, various physical and optoelectronic properties were measured. The measured properties were chosen as the response variables used to perform the multivariate analysis. The selected response variables are various film properties: grain size, thickness, roughness, relative purity, and photoluminescence (PL) peak position and photodetector device properties: responsivity and specific detectivity (Figures 5.1(c)-(h)).

Here, I show how I characterized each response variable by outlining the results for the evaporated film under the central condition, defined by the variable coordinate of 500 mg (source mass), 100 A (heating current), and 1.0 mol ratio (excess MAI ratio). Firstly, the structural properties were probed by microscopy and X-ray diffraction (XRD) measurements. The resulting evaporated $MAPbI_3$ film had a grain size of approximately 37 nm and a thickness of 1333 Å (133.3 nm) as determined from the top-surface image and cross-sectional image measured with field-emission scanning electron microscope (FE-SEM) (Figures 5.1(c) and (d)). The surface morphology of the film was probed by measuring the root-mean-squared value of surface roughness (Rq), which was measured to be 1.8 nm by atomic force microscope (AFM) (Figure 5.1(e)). The crystallinity of the film was analyzed by XRD data which showed peaks at 14.0 and 28.0 degrees (2) that coincide with the predicted results (Figure 5.1(f)). In addition, to determine the relative purity of the film, Rietveld refinement[49-51] was used to quantitatively estimate the amount of PbI_2

present in the $MAPbI_3$ film from the XRD data. Since the ratio of PbI_2 in the $MAPbI_3$ film is proportional to the XRD peak intensity, I defined the relative purity of the films with the following formula,

$$Relative\ purity = \ln\left(\frac{I_{MAPbI_3}\,(14.0°)}{I_{PbI_2}\,(12.6°)}\right),$$

where $I_{\mathrm{MAPbI_3}}\,(14.0°)$ and $I_{\mathrm{PbI_2}}\,(12.6°)$ represent the XRD peak intensity at 14.0° and 12.6° that correspond to $MAPbI_3$ and PbI_2, respectively. Secondly, the photophysical properties of the $MAPbI_3$ film were measured by PL and UV-Vis absorbance spectra to determine the wavelengths of the emission peak and absorption edge, respectively. The PL peak position appeared at near 765 nm which is identical to the expected results from previous studies[39, 52, 53] and UV-vis absorbance edge appeared at 758 nm (Figure 5.1(g)).

Two of the most important response variables of interest can be the device performance parameters of the photodetectors fabricated with the flash-evaporated $MAPbI_3$ film. They are the responsivity (R) which represents a quantitative measure of how much excess electrical current output comes out when illuminated with light input and specific detectivity (D^*) corresponding to the magnitude of the signal to noise ratio of a photodetector per unit bandwidth and unit area. In detail, the responsivity and specific detectivity are determined by $R = (I_{light} - I_{dark})/(PA)$ and $D^* = R\left(\frac{A}{2eI_{dark}}\right)^{\frac{1}{2}}$, respectively, where I_{light} is the current under illumination, I_{dark} is the dark current, P is the light intensity, A is the area of photosensitive region of the OHPs film, and e is the electric charge.[17, 54, 55] The calculated responsivity of the device made with the film deposited under the central condition was found to be 57.8 mA/W (at the applied voltage of 20 V and

incident light power of 667 μW) and the specific detectivity was found to be 1.8×10^9 Jones.

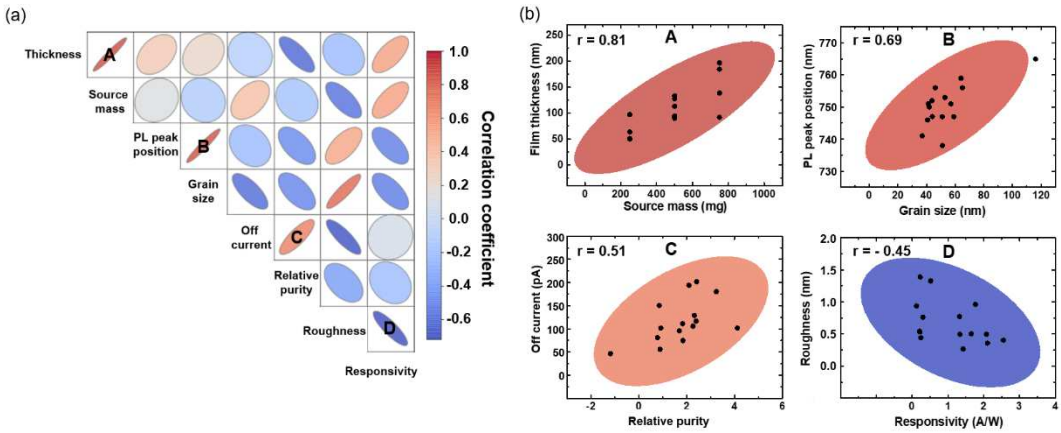

Figure 5.2 (a) Multi-variable correlation matrix plot. (b) Representative correlation graphs for source mass and film thickness, grain size and PL peak position, relative purity and off current, and responsivity and surface roughness. The ellipses in the graphs show the regions with the confidence level of 90 %.

I now explain how the response variables mentioned above were analyzed via the DOE approach to study the correlation between each structural and photophysical property of the evaporated films, which later can be related to the device performances. A total of 15 experiments were conducted with 13 different types of perovskite films made for each condition specified in Figure 5.1(a). Before the regression analysis was conducted, the correlation matrix plot was used to understand the correlation between the variables, which were quantitatively estimated through the value of correlations (Figure 5.2(a)). The correlation matrix plot which is a set of scattering plots between variables provides a simple and holistic approach to check the relationships between the variables before performing detailed regression analysis. The correlations were analyzed by extracting the density ellipse for pairs of each input and response variable. The density ellipse displays

the area that contains 90% of the total data in Figure 5.2(b). When 13 numerical variables were analyzed by the correlation matrix plot, the correlation matrix plot in Figure 5.2(a), which consists of 8 variables, could be expressed to focus on a set of variables with a significant degree of correlation. The following four correlation results were aligned with our expectations: the thickness of the deposited film increased as the source mass increased, as expected (plot A in Figure 5.2(b)). The wavelength of the PL peak position increased as the grain size increased (plot B in Figure 5.2(b)). This red-shift in the PL emission as larger grain size is related to photon-reabsorption of emitted light in larger crystal grains, as reported previously.[56] The higher the relative purity, the larger the dark (off) current (plot C in Figure 5.2(b)), which is related to PbI_2 acting as a charge-intercept barrier[57] (i.e. the dark current increased as the relative proportion of PbI_2 decreased). The responsivity decreased when the film surface became rougher (plot D in Figure 5.2(b)). A smooth morphology is likely to improve the charge transport which can lead to improved photoconductive gain, and therefore a larger photocurrent.[58] Although there is no absolute standard for the correlation coefficient (r) categorization, the r value falling within the range between 0.68 and 1.0 (plot A and B in our case) can be generally considered to indicate a strong correlation, and the range between 0.36 and 0.67 (plot C and D in our case) a moderate correlation.[59]

There were nontrivial correlation results that could be identified with the correlation analysis such as relatively strong correlations between heating current versus off current (+, positive correlation), PL intensity versus thickness (+), grain size versus roughness (+), and PL intensity versus responsivity (+) and the weak correlations between excess MAI ratio versus thickness, MAI ratio versus grain size, relative purity versus responsivity, and relative purity versus specific detectivity. Although some of these weak correlation results

were unexpected (e.g. excess MAI ratio versus thickness/grain size and relative purity versus responsivity/specific detectivity), I could build upon these simple correlation analyses to examine the most relevant factors for optimizing the photodetector device performance parameters by performing detailed regression analyses.

Before going into the regression analysis step, it is necessary to verify the reproducibility of the results to confirm the robustness of the experimental environment. I checked the reproducibility by comparing the three experiments performed for the central condition and re-evaluated additional conditions in the DOE cube. The data clearly show the reproducibility of the thickness, grain size, relative purity, and responsivity under the central condition and an additional DOE Condition. The DOE approach, which analyzes data from multiple angles, can reduce misinterpretation by considering the interactions that can be overlooked in the optimizing process by OFAT method. Through regression analysis, each response variable can be quantitatively associated as a function of input variables to derive meaningful relationships between various film properties and device performance.[60] The regression analysis was performed on 7 response variables-grain size, thickness, roughness, relative purity, PL peak position, responsivity, and specific detectivity- which revealed that grain size, thickness, relative purity, and responsivity values could be modeled well with input variables. On the other hand, the accuracy of modeling roughness, PL peak position, and specific detectivity was relatively low, and therefore these variables were excluded from the subsequent analysis.

For each response variable, I can represent the regression model as a three-dimensional (3D) scattering plot with the axes and range corresponding to the input variable cube shown in Figure 5.1(a). In the case of the thickness (Figure 5.3(a)), if I examine a cross-section from the 3D scattering plot perpendicularly to the excess MAI ratio

axis at MAI/$MAPbI_3$ ratio of 1 (shown as the brown dashed line in Figure 5.3(a)), a two-dimensional (2D) contour plot can be extracted with the source mass and heating current (Figure 5.3(b)). If I look closely at the lines along with the heating current values of 60 A (green line in Figure 5.3(b)), 100 A (orange), and 140 A (black), the thickness increases linearly with the source mass for all the current values (Figure 5.3(c)). However, the slope of the increase in the thickness varies according to the heating current: the lower the heating current, the larger the slope. This is an example of an interaction effect, where the effect of one input variable (i.e. source mass) on a response variable (i.e. thickness) depends on another variable (i.e. heating current).

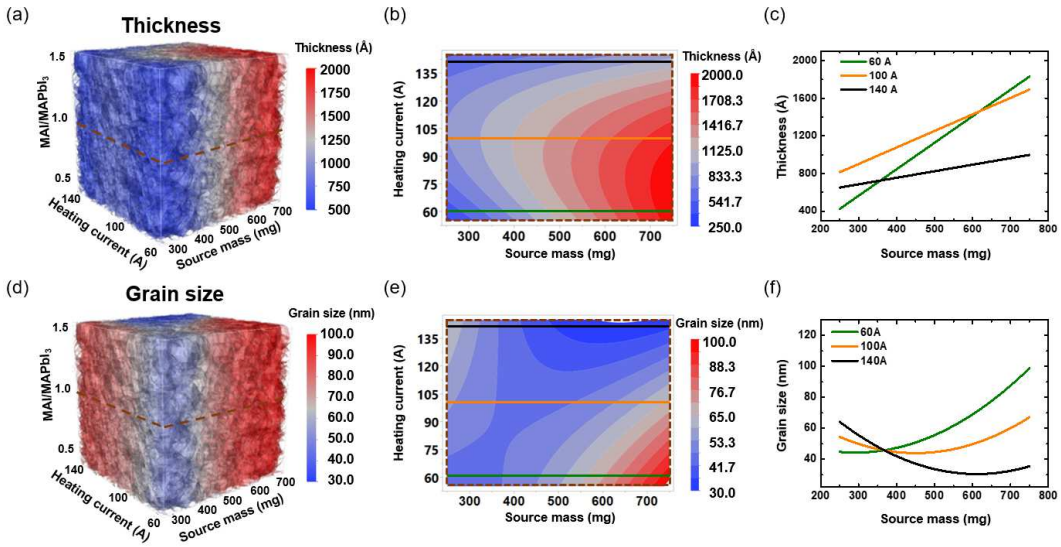

Figure 5.3 (a) A 3D scattering plot of the film thickness according to the heating current, source mass, and excess MAI ratio (MAI/$MAPbI_3$) from the regression analysis. (b) A contour plot of the film thickness according to the heating current and the source mass. (c) Graphs of the film thickness as a function of the source mass at the different heating currents of 60 A (green line), 100 A (orange line), and 140 A (black line). (d), (e), and (f) are the same graphs as (a), (b) and (c) but represent the grain size instead of the film thickness.

The regression analysis for grain size (Figure 5.3(d)) reveals the feature of interaction effect more clearly. I can no longer observe simple linear relationships between the source mass and the grain size in the 2D contour plot at an excess MAI ratio of 1 (Figures 5.3(e) and (f)). Depending on the heating current, the grain size either increases (heating current of 60 A) or decreases (140 A) with source mass. This is a good example of an interaction effect, where a response variable (i.e. grain size) is affected strongly by interaction terms of multiple variables (i.e. heating current × source mass). In other words, the grain size cannot be represented by a simple linear model. This is the origin of an apparently weak correlation between the grain size and the source mass from the correlation matrix plot in Figure 5.2, since the interaction with other variables (i.e. heating current) was neglected. Similarly, each interaction between input variables for each response variable can be effectively expressed by the interaction plot. Overall, I have demonstrated that the multivariate regression analysis allows us to predict various film properties by modeling their complex relationships with multiple input variables which collectively define the film deposition conditions.

The goal of our study is to employ DOE for optimizing film deposition conditions for obtaining high-performance flash-evaporated perovskite photodetector devices. The DOE process allowed us to predict the responsivity values of photodetector devices via regression analysis as can be shown from a high R^2 value. In order to optimize the responsivity, the deposition condition can be simply found where the predicted responsivity value reaches maximum in the regression analysis result. In this way, it is possible to fabricate photodetectors with film deposition conditions predicted to achieve the maximum responsivity value without individually controlling the factors that affect responsivity such as grain size, relative purity, and trap density. Nevertheless, it is informative to carry out a

detailed correlation analysis in order to find out the main factors accountable for the optimized device performance. Therefore, I focused on extracting relationships between responsivity and other response variables for which reliable regression models with high R^2 values were obtained: thickness, relative purity, and grain size.

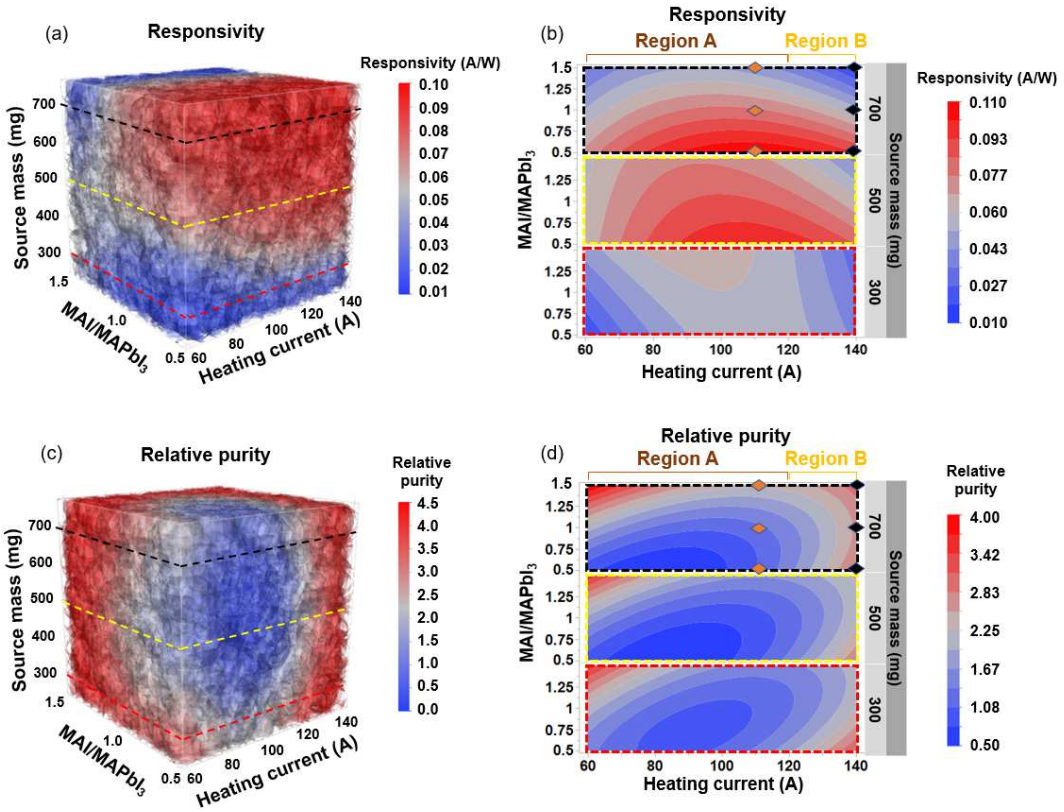

Figure 5.4. 3D scattering plots of (a) the responsivity and (c) the relative purity according to the heating current, source mass, and MAI/MAPbI$_3$ from the regression analysis. Contour plots of (b) responsivity and (d) the relative purity is extracted from 3D scattering data (Figure 5.4(a) and (c)) at the source mass of 300, 500, 700 mg.

As shown in the 3D scattering plot (Figure 5.4(a)), the responsivity is predicted to increase as the source mass increases. This is expected due to the strong influence of the source mass on the deposited thickness of the perovskite film (Figure 5.3(c)). Since the

tested thickness range is significantly smaller than the expected light penetration depth in $MAPbI_3$,[61] the generated photocurrent at the same input light power will attune to a similar scale with the thickness of the film. I have experimentally confirmed the thickness scaling in the responsivity by comparing photodetector devices made with multi-stacked perovskite films.

I tried to discover hidden details within the expected thickness scaling of the responsivity by looking at 2D contour plots (Figure 5.4(b)) generated from planar cross-sections of the 3D plot for the source mass of 300 mg (red dashed line cut in Figure 5.4(a)), 500 (yellow), and 700 mg (black). Figures 5.4(c) and (d) are the 3D scattering plots and corresponding 2D contour plots generated from the regression analysis for the relative purity of the evaporated film. When comparing Figures 5.4(b) and (d) as a whole, the responsivity and relative purity do not seem to have a clear correlation, which implies complexities in relating the responsivity and relative purity from the input variables. However, when it comes to a smaller deposition condition range, a noticeable correlation can be found. More specifically, if I divide the regions according to the heating current value as “Region A” from 60 A to 120 A and “Region B” from 120 A to 140 A (see Figures 5.4(b) and (d)), a negative correlation between responsivity and relative purity can be seen in Region A in the contour plot for the source mass of 700 mg (top panels of Figures 5.4(b) and (d)). This result is consistent with previous reports that the responsivity increases with incorporation of PbI_2 impurities in the perovskite film.[57, 62-64] The origin of the different trends between the responsivity and relative purity in Region B is not entirely clear, but a finite formation of extra perovskite phases such as low dimensional perovskites[52] by evaporating films at the high heating current values near 140 A may contribute to the discrepancy. The grain size and responsivity showed a relatively small

correlation, which may be due to a limited range of the grain size tested in our study compared to previous works.[65]

In order to experimentally confirm our regression models with actual data, I fabricated photodetectors with perovskite films evaporated under six deposition conditions at the edge of Region A and Region B (the orange and black points in Figures 5.4(b) and (d)). Firstly, for the three conditions denoted as the orange points in Region A, I could confirm the negative correlation between the relative purity and the responsivity, as predicted by the regression analysis, i.e., the relative purity increased and responsivity decreased as increasing the excess MAI ratio.

In addition, I further investigated the origin of the negative correlation between the relative purity of the evaporated film and the responsivity from the films deposited at these three conditions: a low relative purity film seems to contain some PbI_2 on the surface of the perovskite film suppressing non-radiative recombination near the contacts[57, 62-64]. Secondly, for the other three deposition conditions denoted as black points in Region B, the relative purity of the film remained relatively constant but the responsivity decreased with the excess MAI ratio (Figure 5.4(b)), which also confirms the predictions from the regression model. The sound agreements between the experimental results for the responsivity and relative purity with the prediction of the regression models guarantee the reliability of the formulated regression models.

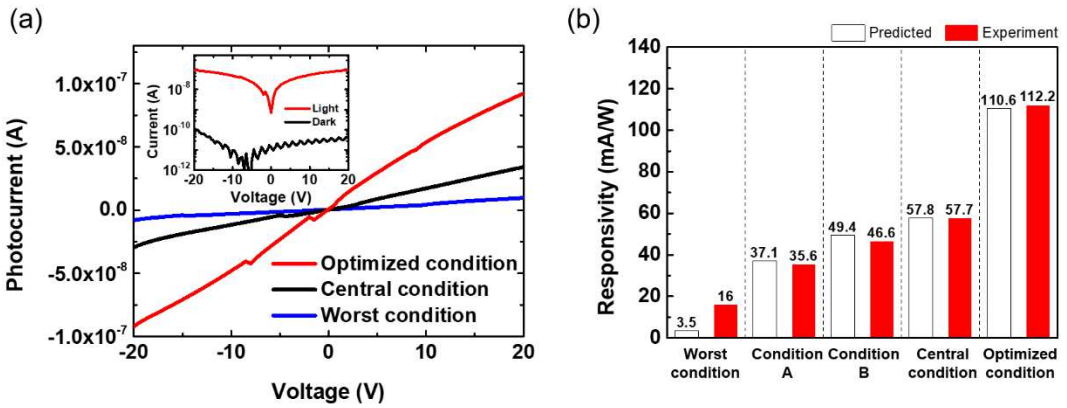

Figure 5.5 (a) I-V characteristics of white light illuminated photodetectors with three different $MAPbI_3$ films which are flash-evaporated under the optimized (red), central (black), and worst (blue) deposition condition. The inset shows log-scale I-V curves of the optimized photodetector under white light illumination (red) and dark (black) conditions. (b) The predicted responsivity values from the regression model (white) and experimental values (red) under various deposition conditions.

As the final step of the DOE process, I fabricated a photodetector device with the optimized film deposition condition and evaluated its device performance. The optimized deposition condition for maximizing the responsivity was predicted to the source mass of 650 mg, the excess MAI mol ratio of 0.5, and the heating current of 110 A. For comparison, other photodetectors were also fabricated with perovskite films deposited under the conditions expected to perform worse: including the predicted worst deposition condition (the source mass of 750 mg, the excess MAI mol ratio of 1.5, and the heating current of 140 A). Figure 5.5(a) shows the photoelectric characteristics of photodetectors made of the perovskite films deposited under several different deposition conditions including the optimized and the worst condition. As expected, the photocurrent was largest in the optimized photodetector and smallest in the worst condition photodetector. The responsivity of the optimized device was found to be 112.2 mA/W, as confirmed from

multiple evaluations. This is a 98% improvement over the responsivity of the central condition photodetector, and 600% improvement over that of the worst condition photodetector. Moreover, to confirm the aforementioned influence of PbI_2 on the photodetector performance, approximately 0.3% of PbI_2 was detected in the deposited film via Rietveld refinement of the X-ray diffraction pattern.

Although the specific detectivity values of photodetector devices were not discussed previously due to low reliability of the regression model, the specific detectivity could be also significantly improved with the value for the optimized device showing an order of magnitude higher compared to that of the device fabricated under the worst deposition condition. It is remarkable that the device performance parameters could be improved significantly by only proceeding parametric optimization of deposition conditions and without the introduction of a new deposition method or architectural improvement of the device. Although the optimum deposition conditions acquired with our analysis may not be directly transferred to other deposition systems due to variations in experimental conditions, the methodologies demonstrated here, along with our analysis results, can be applied to any deposition systems. Furthermore, our work demonstrates the advantage of DOE process for its accuracy in the predictability of the photodetector responsivity values under various deposition conditions and the efficiency of the device optimization process which requires only a small number of experiments.

5.3. Experiments

Synthesis of a $MAPbI_3$ Single Crystal Powder: 2.66 g of PbO (99.9% trace metal basis) and 1.90 g of CH_3NH_3I (MAI, 99.5%) were mixed and dissolved into a mixture of 18 ml hydriodic acid (HI, 57 wt% in water) solution and 2 ml hypophosphorous acid

(H_3PO_2, 50 wt% in water) solution. The solution was heated at 130 °C on a hotplate until the precipitates completely disappeared. Then, the solution was cooled at room temperature to precipitate a $MAPbI_3$ single crystal powder. The single crystal powder was filtrated and dried in a vacuum condition.

Perovskite Film Evaporation: The thermally grown 270 nm thick SiO_2 on Si and glass were used as substrates. The substrates were sequentially sonicated in acetone, 2-propanol, and deionized water for 10 min each. Then, the SiO_2 and glass substrates were cleaned using O_2 plasma treatment for 120 seconds. For flash evaporation, the synthesized $MAPbI_3$ powder was loaded onto a tungsten boat in a vacuum chamber. The cleaned substrates were placed into the chamber at a height of 30 cm from the source material. Then, the chamber was evacuated to a pressure of Torr. The tungsten boat was rapidly heated by applying a current of 100 A. The source powder was fully evaporated within 30 s.

Characterization and Measurement: Scanning electron microscopy (SEM): The images of the perovskite film were captured using JSM-7800F Prime at 5-10 kV.

X-ray diffraction (XRD): Crystallographic structures of perovskite films were analyzed by high-resolution X-ray diffractometer (HRXRD) technique (Rigaku Smartlab).

Rietveld refinement: XRD patterns were subject to Rietveld refinement using the GSAS-II [34] software for phase quantification. Strong preferred orientations of the deposited films required use of the March-Dollase function; peak broadening was treated with the domain size model due to the relatively small grain sizes (approx. 50 nm via SEM).

Photoluminescence (PL) spectroscopy: Steady-state PL spectra were measured using a spectrofluorometer (JASCO FP-8500) with a 520 nm excitation source.

UV-visible absorbance spectroscopy: Absorbance spectra were measured using a UV/Vis spectrophotometer (PerkinElmer LAMBDA 45).

Atomic force microscopy (AFM): The perovskite layer surface was characterized by an atomic force microscope system (NX 10 AFM, Park Systems).

Device fabrication: In order to fabricate photodetector, Au electrodes with a thickness of 50 nm were deposited on the prepared perovskite film by electron-beam evaporator through a shadow mask. The channel length and width of the fabricated photodetector were 50 μm and 1 mm.

Device measurement: The perovskite photodetector characteristics were measured using a semiconductor parameter analyzer (Keithley 4200 SCS). All the measurements were performed in a vacuum environment.

Data Analysis: All data were analyzed by a statistical analysis program (SAS JMP Pro 15).

5.4. Conclusion

I have employed DoE approach for systematically investigating the deposition conditions and film properties of single-source flash-evaporated $MAPbI_3$ films with the aim of optimizing photodetector device performance. In total, OHP films were deposited under 15 different experimental conditions specified by three input variables -source mass, excess MAI, and heating current- selected by the Box-Behnken design to map various response variables that represent the structural and photophysical properties of the deposited films and photodetector device parameters. The correlations between the different film and device properties were investigated by using both a correlation matrix plot and regression analysis that enabled a detailed multivariate analysis. Our analysis reveals a significant interaction between the variables, which indicates a complex nature of the relationships between each film property and the input variables. Therefore, a

simultaneous consideration of the variables via a multivariate approach is essential for optimizing the film deposition conditions, which cannot be achieved with a commonly practiced one-variable-at-a-time method. I have fabricated photodetector devices with the optimized deposition conditions predicted from the regression model (showing a responsivity value of 112.2 mA/W), which can be accurately predicted from the regression analysis. Overall, our work promotes DoE approach as an efficient statistical tool for optimizing perovskite film deposition conditions and a reliable route for extracting information on multi-dimensional relationships between material and device properties, which can be expanded to other complex optimization problems remaining in the general materials and device communities.

References

[1] Hwang B and Lee J-S 2019 *Adv. Opt. Mater.* **7** 1801356

[2] Tan Z-K, Moghaddam R S, Lai M L, Docampo P, Higler R, Deschler F, Price M, Sadhanala A, Pazos L M, Credgington D, Hanusch F, Bein T, Snaith H J and Friend R H 2014 *Nat. Nanotechnol.* **9** 687-92

[3] Choi H, Mai C-K, Kim H-B, Jeong J, Song S, Bazan G C, Kim J Y and Heeger A J 2015 *Nat. Commun.* **6** 7348

[4] Lee H-D, Kim H, Cho H, Cha W, Hong Y, Kim Y-H, Sadhanala A, Venugopalan V, Kim J S, Choi J W, Lee C-L, Kim D, Yang H, Friend R H and Lee T-W 2019 *Adv. Funct. Mater.* **29** 1901225

[5] Blancon J C, Tsai H, Nie W, Stoumpos C C, Pedesseau L, Katan C, Kepenekian M, Soe C M M, Appavoo K, Sfeir M Y, Tretiak S, Ajayan P M, Kanatzidis M G, Even J, Crochet J J and Mohite A D 2017 *Science* **355** 1288

[6] Park N-G 2018 *MRS Bull.* **43** 527-33

[7] Nie W, Tsai H, Asadpour R, Blancon J-C, Neukirch A J, Gupta G, Crochet J J, Chhowalla M, Tretiak S, Alam M A, Wang H-L and Mohite A D 2015 *Science* **347** 522

[8] Tsai H, Nie W, Blancon J-C, Stoumpos C C, Asadpour R, Harutyunyan B, Neukirch A J, Verduzco R, Crochet J J, Tretiak S, Pedesseau L, Even J, Alam M A, Gupta G, Lou J, Ajayan P M, Bedzyk M J, Kanatzidis M G and Mohite A D 2016 *Nature* **536** 312-6

[9] Yang W S, Noh J H, Jeon N J, Kim Y C, Ryu S, Seo J and Seok S I 2015 *Science* **348** 1234

[10] Fang Y, Dong Q, Shao Y, Yuan Y and Huang J 2015 *Nat. Photonics* **9** 679-86

[11] Zhou H, Chen Q, Li G, Luo S, Song T-b, Duan H-S, Hong Z, You J, Liu Y and Yang Y 2014 *Science* **345** 542

[12] Zhao X and Tan Z-K 2020 *Nat. Photonics* **14** 215-8

[13] Xing G, Mathews N, Lim S S, Yantara N, Liu X, Sabba D, Grätzel M, Mhaisalkar S and Sum T C 2014 *Nat. Mater.* **13** 476-80

[14] Cho H, Jeong S-H, Park M-H, Kim Y-H, Wolf C, Lee C-L, Heo J H, Sadhanala A, Myoung N, Yoo S, Im S H, Friend R H and Lee T-W 2015 *Science* **350** 1222

[15] Cao Y, Wang N, Tian H, Guo J, Wei Y, Chen H, Miao Y, Zou W, Pan K, He Y, Cao H, Ke Y, Xu M, Wang Y, Yang M, Du K, Fu Z, Kong D, Dai D, Jin Y, Li G, Li H, Peng Q, Wang J and Huang W 2018 *Nature* **562** 249-53

[16] Qian L, Sun Y, Wu M, Xie D, Ding L and Shi G 2017 *Adv. Mater.* **29** 1606175

[17] Dou L, Yang Y, You J, Hong Z, Chang W-H, Li G and Yang Y 2014 *Nat. Commun.* **5** 5404

[18] Kang K, Ahn H, Song Y, Lee W, Kim J, Kim Y, Yoo D and Lee T 2019 *Adv. Mater.* **31** 1804841

[19] Hwang B and Lee J-S 2017 *Sci. Rep.* **7** 673

[20] Wang J, Senanayak S P, Liu J, Hu Y, Shi Y, Li Z, Zhang C, Yang B, Jiang L, Di D, Ievlev A V, Ovchinnikova O S, Ding T, Deng H, Tang L, Guo Y, Wang J, Xiao K, Venkateshvaran D, Jiang L, Zhu D and Sirringhaus H 2019 *Adv. Mater.* **31** 1902618

[21] Senanayak S P, Yang B, Thomas T H, Giesbrecht N, Huang W, Gann E, Nair B, Goedel K, Guha S, Moya X, McNeill C R, Docampo P, Sadhanala A, Friend R H and Sirringhaus H 2017 *Sci. Adv.* **3** e1601935

[22] Yu W, Li F, Yu L, Niazi M R, Zou Y, Corzo D, Basu A, Ma C, Dey S, Tietze M L, Buttner U, Wang X, Wang Z, Hedhili M N, Guo C, Wu T and Amassian A 2018 *Nat. Commun.* **9** 5354

[23] Park N-G 2015 *Mater. Today* **18** 65-72

[24] Niu L, Liu X, Cong C, Wu C, Wu D, Chang T R, Wang H, Zeng Q, Zhou J, Wang X, Fu W, Yu P, Fu Q, Najmaei S, Zhang Z, Yakobson B I, Tay B K, Zhou W, Jeng H T, Lin H, Sum T C, Jin C, He H, Yu T and Liu Z 2015 *Adv. Mater.* **27** 7800-8

[25] Lan C, Dong R, Zhou Z, Shu L, Li D, Yip S and Ho J C 2017 *Adv. Mater.* **29** 1702759

[26] Momblona C, Gil-Escrig L, Bandiello E, Hutter E M, Sessolo M, Lederer K, Blochwitz-Nimoth J and Bolink H J 2016 *Energy Environ. Sci.* **9** 3456-63

[27] Mitzi D B, Prikas M T and Chondroudis K 1999 *Chem. Mater.* **11** 542-4

[28] Chen Y, Zhang L, Zhang Y, Gao H and Yan H 2018 *RSC Adv.* **8** 10489-508

[29] Li G, Ho J Y L, Wong M and Kwok H-S 2016 *physica status solidi (RRL) – Rapid Research Letters* **10** 153-7

[30] Ávila J, Momblona C, Boix P P, Sessolo M and Bolink H J 2017 *Joule* **1** 431-42

[31] Sessolo M, Momblona C, Gil-Escrig L and Bolink H J 2015 *MRS Bull.* **40** 660-6

[32] Crane M J, Kroupa D M, Roh J Y, Anderson R T, Smith M D and Gamelin D R 2019 *ACS Applied Energy Materials* **2** 4560-5

[33] Du P, Li J, Wang L, Liu J, Li S, Liu N, Li Y, Zhang M, Gao L, Ma Y and Tang J 2019 *ACS Appl. Mater. Interfaces* **11** 47083-90

[34] Liu M, Johnston M B and Snaith H J 2013 *Nature* **501** 395-8

[35] Ono L K, Wang S, Kato Y, Raga S R and Qi Y 2014 *Energy Environ. Sci.* **7** 3989-93

[36] Yang D, Yang Z, Qin W, Zhang Y, Liu S and Li C 2015 *J. Mater. Chem. A* **3** 9401-5

[37] Chen C-W, Kang H-W, Hsiao S-Y, Yang P-F, Chiang K-M and Lin H-W 2014 *Adv. Mater.* **26** 6647-52

[38] Hwang B and Lee J-S 2017 *Adv. Mater.* **29** 1701048

[39] Fan P, Gu D, Liang G-X, Luo J-T, Chen J-L, Zheng Z-H and Zhang D-P 2016 *Sci. Rep.* **6** 29910

[40] Longo G, Gil-Escrig L, Degen M J, Sessolo M and Bolink H J 2015 *Chem. Commun.* **51** 7376-8

[41] Xu H, Wu Y, Xu F, Zhu J, Ni C, Wang W, Hong F, Xu R, Xu F, Huang J and Wang L 2016 *RSC Adv.* **6** 48851-7

[42] Lohmann K B, Patel J B, Rothmann M U, Xia C Q, Oliver R D J, Herz L M, Snaith H J and Johnston M B 2020 *ACS Energy Lett.* **5** 710-7

[43] Kuehl R O and Kuehl R 2000

[44] Antony J 2014 *Design of experiments for engineers and scientists*: Elsevier)

[45] Tyagi P, David T W, Stoichkov V D and Kettle J 2019 *Sol. Energy* **193** 12-9

[46] Gunst R F 1996 *Technometrics* **38** 284-6

[47] *Response Surfaces, Mixtures, and Ridge Analyses*, pp 509-33

[48] Ferreira S L C, Bruns R E, Ferreira H S, Matos G D, David J M, Brandão G C, da Silva E G P, Portugal L A, dos Reis P S, Souza A S and dos Santos W N L 2007 *Anal. Chim. Acta* **597** 179-86

[49] Ando Y, Ohishi Y, Suzuki K, Suzuki A and Oku T 2018 *AIP Conference Proceedings* **1929** 020003

[50] McCusker L, Von Dreele R, Cox D, Louër D and Scardi P 1999 *J. Appl. Crystallogr.* **32** 36-50

[51] Von Dreele R 1997 *J. Appl. Crystallogr.* **30** 517-25

[52] Song Z, Watthage S C, Phillips A B, Tompkins B L, Ellingson R J and Heben M J 2015 *Chem. Mater.* **27** 4612-9

[53] Daniel M K, Matthew J C and Daniel R G 2019 Single-source flash sublimation of metal-halide semiconductors(vol 11084)

[54] Fang Y, Armin A, Meredith P and Huang J 2019 *Nat. Photonics* **13** 1-4

[55] García de Arquer F P, Armin A, Meredith P and Sargent E H 2017 *Nat. Rev. Mater.* **2** 16100

[56] Kanemitsu Y 2017 *J. Mater. Chem. C* **5** 3427-37

[57] Cao D H, Stoumpos C C, Malliakas C D, Katz M J, Farha O K, Hupp J T and Kanatzidis M G 2014 *APL Mater.* **2** 091101

[58] Hinds S, Levina L, Klem E J D, Konstantatos G, Sukhovatkin V and Sargent E H 2008 *Adv. Mater.* **20** 4398-402

[59] Taylor R 1990 *Journal of Diagnostic Medical Sonography* **6** 35-9

[60] Leng L, Zhang T, Kleinman L and Zhu W 2007 *J. Phys. Conf. Ser.* **78** 012084

[61] Shi Z, Zhang Y, Cui C, Li B, Zhou W, Ning Z and Mi Q 2017 *Adv. Mater.* **29** 1701656

[62] Jacobsson T J, Correa-Baena J-P, Halvani Anaraki E, Philippe B, Stranks S D, Bouduban M E F, Tress W, Schenk K, Teuscher J, Moser J-E, Rensmo H and Hagfeldt A 2016 *Journal of the American Chemical Society* **138** 10331-43

[63] Kim Y C, Jeon N J, Noh J H, Yang W S, Seo J, Yun J S, Ho-Baillie A, Huang S, Green M A, Seidel J, Ahn T K and Seok S I 2016 *Adv. Energy Mater.* **6** 1502104

[64] Wang L, McCleese C, Kovalsky A, Zhao Y and Burda C 2014 *Journal of the American Chemical Society* **136** 12205-8

[65] Geske T, Li J, Worden M, Shan X, Chen M, Bade S G R and Yu Z 2017 *Adv. Funct. Mater.* **27** 1702180

[66] Toby B H and Von Dreele R B 2013 *J. Appl. Crystallogr.* **46** 544-9

Chapter 6. Summary

In this thesis, I described the research results mainly focusing on unipolar non-volatile resistive memory devices for flexible electronics application. In particular, materials that can be used in flexible resistive memory devices and the fundamental physics of unipolar resistive memory devices were studied.

First, I demonstrated that even with inorganic materials, flexible memory devices can be fabricated by using a low temperature and dry process. I fabricated resistive memory devices with Al_2O_3 on a conventional tape substrate. The memory devices showed good electrical performance regardless of bending condition. The memory devices held their ON/OFF states for over 10^4 s and withstood 200 cycles of switching with a high ON/OFF ratio ($\sim 10^4$).

Secondly, I investigated the fundamental physics of unipolar resistive memory devices. The unclear operating principle of the unipolar resistive memory devices is a major cause of slowing the development speed of the resistive memory device. I indirectly explored the fundamental physics of the memory device by applying voltage stress to the memory device and exploring whether the current reacts with time. By statistically analyzing, I found that turn-on process can be explained by formation of conducting paths and the formation occurs probabilistically depending on the external voltage value. I discovered that active materials showing unipolar resistive switching shared the probabilistic nature of the conducting path formation.

Finally, we studied an organic-halide perovskite, a new material that can be used for resistance change memory. I demonstrate that single-source flash evaporation is a promising method to deposit large-area perovskite films controllably and reliably. Although

I did not fabricate the resistive memory device using this material, I provided a milestone for fabricating a large-scale perovskite resistive memory device by studying the $MAPbI_3$ evaporation method.

국문초록

유연 소자 적용을 위한 단극성 비휘발 메모리의 저항변화 스위칭 동작 연구

이우철
서울대학교 물리천문학부

오늘날 트랜지스터 및 메모리 소자와 같은 전자 소자를 유연, 또는 투명하거나 신축성이 있도록 제작하는 시도가 늘어나고 있다. 하지만, 전자 소자에 가장 많이 사용되는 기판인 실리콘은 이러한 특성이 거의 없다. 실리콘 기판의 한계를 극복하기 위해 휘어지는 기판과 휘어지는 반도체 물질을 탐색하는 연구가 진행되고 있다. 플라스틱 필름, 섬유 종이 또는 테이프와 같은 많은 종류의 기판이 휘어지는 전자 소자를 제작하기 위해 기판으로 사용되고 있다. 이 중 테이프는 유연성, 부착성 및 저렴한 가격 등 기판으로 활용되기에 좋은 특성을 가지고 있다. 한편, 유기물은 유연성이 우수하여 휘어지는 전자 소자의 활물질로 사용되고 있다. 유기 저항변화 메모리는 유기 재료의 다양성, 저렴한 소자 제조 비용, 인쇄 가능성 등과 같은 여러 장점을 갖는 유망한 데이터 저장 기술이다. 그러나 유기 저항변화 메모리 소자에서 저항 스위칭 현상의 메커니즘은 명확하게 이해되지 않았다는 문제점이 있다.

먼저, 휘어지는 메모리 소자를 만들기 위해 시판되는 테이프를 기판으로 사용하여 메모리를 제작하였다. 휘어지는 기판인 테이프 위에 8×8 어레이의 비휘발성 저항변화 메모리 소자를 제작했다. 메모리 소자 구조는 $Au/AlO_x/Au/AlO_x/Al/tape$ 이다. 제조 공정은 저온, 건식 공정을 활용하여 테이프 기판의 손상 없이 메모리 소자를 제작할 수 있었다. 제작된 메모리 소자는

전형적인 단극성 비휘발 저항변화 메모리 특성을 나타냈다. 메모리 소자는 ~3.5 V에서 ON 상태로 바뀌고 5 V 후에 음의 기울기 영역을 나타내며, ~10 V에서 OFF 상태로 바뀌었다. 메모리 소자는 높은 ON/OFF 비율, 우수한 재현성, 우수한 안정성, 그리고 높은 수율을 나타냈다. 특히 ON/OFF 비율은 ~10^4으로 높았으며 장치는 200 번 이상의 읽기/쓰기 동작을 견뎌냈다. 소자의 데이터 유지 시간은 ~10^4 초 이상이었다. 수율은 ~68 %로 나타났으며, 이 메모리 소자는 극도로 휘어진 상태에서도 안정적인 전기적 특성을 보여주었다.

휘어지는 저항변화 메모리 소자를 제작하였으나, 뚜렷한 단극 저항변화 메모리의 작동원리는 밝혀지지 않은 상황이었다. 이에 단극 저항변화 메모리의 작동원리를 조사하기 위해 메커니즘 탐구에 적합한 새로운 단극 저항변화 메모리를 제작하였다. 메모리 소자에 일정한 전압 스트레스를 메모리 소자에 인가하였고, 시간에 따른 전류 동작을 조사하였다. 이 측정에서 가해진 스트레스 전압은 ON 상태로 만들기 위한 알려진 문턱 전압보다 낮음에도 불구하고 전류는 급격하게 증가하였고 결국 메모리 소자는 ON 상태에 도달했다. 낮은 전압 스트레스 하에서 ON 상태에 도달하는 데 필요한 시간의 분포는 Weibull 분포로 설명할 수 있었다. 켜지는 데 걸리는 시간에 대한 통계 분석을 통해 전류의 급격한 증가가 일정한 확률 법칙을 따르는 것을 발견하였다. 시간이 지남에 따라 전류가 증가할 확률은 동일한 전압 스트레스 하에서 OFF 상태와 모든 중간 저항 상태에서 일정하게 나타났다. 스트레스 전압이 증가함에 따라 전류가 증가할 확률은 기하 급수적으로 상승했다. 이러한 통계적 분석을 통해 메모리가 켜지는 과정은 활물질 내부에 전류가 잘 통하는 percolation network 통로가 확률적으로 형성되며 저항값이 낮아진다고 추정하였다.

박사학위 과정 동안의 연구에서 단극 저항변화 메모리를 활용하여 휘어지는 메모리 소자를 제작하였고, 단극 저항변화 메모리 소자의 작동원리에 대하여 탐구하였다. 본 연구를 통하여 단극 저항변화 메모리 소자의 작동원리의 많은 부분을 이해할 수 있었으며, 메모리 소자의 효율적으로 활용하기 위한 작동 방식을 제시하였다. 또한, 이 연구는 앞으로 더 향상된 단극 저항변화 메모리를 제작할 수 있도록 돕는 발판을 제공하였다.

Keywords: 저항변화 메모리 소자, 유기 메모리 소자, 저항변화 메모리의 스위칭 동작, 유니폴라 메모리 소자

Student Number: 2014-22373